Quantitative Pore-Scale Analysis of CO_2 Foam for CCUS

Master Thesis in Reservoir Physics

by

Benyamine Benali

Department of Physics and Technology

University of Bergen

December 2019

Abstract

This experimental thesis is a part of ongoing projects lead by the Reservoir Physics group at the Department of Physics and Technology, University of Bergen. The main objectives of this thesis were to develop image analysis software to quantitatively describe CO_2 foam for CCUS at the pore scale, investigate the separate and combined use of surfactants and nanoparticles as foaming agents for CO_2 foam in the absence of oil at pore space, and to study calcite precipitation and dissolution in a micromodel to shed light on pore scale mechanisms during CO_2 storage in carbonate reservoirs.

The high pressure silicon wafer micromodels used enabled direct pore-scale visualization at relevant pore pressures of fluid dynamics, foam texture, foam stability, and foam performance. Micromodel porosity and permeability were found to be 0.607 ± 0.001 and 2.97 ± 0.07 D, respectively. Qualitative image analysis of fluid displacements occurring in the micromodel is useful to shed light on potential new displacement mechanisms, but provide limited information in a restricted field of view and it is time consuming. A major contribution in this thesis is the development of new image analysis tools that allow quantitative analysis on fluid displacement mechanisms and CO_2 foam behavior. Access to dynamic, quantitative data from image analysis enables calculation of bubble generation and coalescence rates during CO_2 injections, and direct comparison when parameters are varied in a controlled manner. The software development and experiments reported has been conducted in collaboration with PhD candidate Tore L. Føyen.

The CO_2 was injected in an unsteady-state approach, where the pores were initially fully saturated with fluid (brine and surfactants and/or nanoparticles) before the CO_2 was injected at constant rate (1 $\mu l/min$ or 4 $\mu l/min$). The microscope continuously captured images of the pore scale displacement during injection, and the images were analyzed by the developed software. The number of bubbles was obtained from each image and plotted as a function of the pore volumes CO_2 injected. In addition density plots were used to illustrate the location of the bubbles and visualize the channels and foam generation path.

Results from the CO_2 foam experiments show that surfactant and nanoparticles generated a strong foam compared to baseline: bubbles numbers recorded when using foaming agents (surfactants and nanoparticles) increased significantly relative to the baseline (no foaming agent present, only brine), indicating a high CO_2 mobility reduction. The number of bubbles increase with increasing surfactant concentration (0.05 wt% to 0.5 wt%), and the foam was found “shear thickening” for increasing rate. The comparison made between surfactant- and nanoparticle-stabilized foams at pore-scale indicates that surfactants have a higher ability to generate foams, whereas nanoparticles display a more significant potential to stabilize foams. The synergy between nanoparticles and surfactant demonstrated that foam generation and stability are independent of nanoparticles concentration in the absence of oil for the concentrations used in this thesis.

The reported laboratory pore scale observations of calcite precipitation and dissolution were conducted in collaboration with PhD candidates Malin Haugen and Tore L. Føyen. A procedure for using of *Sporosarcina pasteurii* bacteria was developed as part of this thesis, and the calcite successfully precipitated in the pore space and calcite dissolution was studied at room temperature using 2 wt% hydrochloric acid. The procedure must be further developed to achieve a uniform distribution of calcite in the pore space to allow for controlled experiments related to the dissolution of calcite during CO_2 storage in carbonate.

Acknowledgements

First I would like to express my gratitude to my main supervisor Prof. Martin Fernø and co-supervisor Dr. Bergit Brattekås at the Department of Physics and Technology at the University of Bergen, for giving me the opportunity to work on interesting research projects. Thank you Martin for the support, guidance, and valuable discussions.

I would also like to thank PhD candidate Tore L. Føyen. Thank you for your guidance, patience, motivation, and collaboration. Thank you for your positivity and for keeping your doors open whenever I needed your help.

I would also like to thank Prof. Arne Graue and Associate Prof. Geir Ersland for their contributions to the reservoir physics group.

I would also like to thank my fellow students both during the bachelor and master studies for many interesting discussions and social events. Thank you for always being in a good mood, solution oriented and for your never ending willingness to share your knowledge.

Finally, I would like to thank my family Zineb, Yazid and Kaouthar for their support and motivations during my period of studying at the University of Bergen.

Bergen, December 2019

Benyamine Benali

Table of Contents

Part I: Introduction and Theory

1. Energy Demand and Climate Change in Context of CCUS

Energy plays a vital role in our everyday lives, we use it for transportation, internet, heating, and we consume it 24 hours a day. Cheap, renewable, and sustainable energy stipulation is one of the most critical issues in our lifetime and in the future. The population quadrupled in the 20th century, and explains why energy demand has increased 16 times in the same period. In particular, we need 13 terawatts (TW) of energy to sustain 6.5 billion people worldwide with their current lifestyle. In 2050, an additional 10 TW of clean energy (Kamat, 2007) is needed to sustain the same lifestyle. During the British Industrial Revolution, when coal surpassed renewable energy after 1780, the era of fossil fuel began. In 1859, oil started to replace coal and by the 1940s, oil became the dominant source of energy. The global dependence on fossil fuels is now 85.5% of total energy consumption (Ediger, 2019). Chemically, fossil fuels contain energy and release energy by combustion, this chemical reaction's products are mostly water vapor, steam, and CO_2.

In its synthesis Report on Climate Change (2014), the Intergovernmental Panel on Climate Change (IPCC) stated that human influence on the climate system is evident and that recent greenhouse gas anthropogenic emissions are the highest in history (IPCC, 2014). The CO_2 level gradually increased from the global pre-industrial level of 280 parts per million (ppm) (Yokota et al., 2009) and in April 2019 it reached 412 ppm (Tans & Keeling, 2019) globally. In its Special Report on Global Warming of 1.5 ℃, the IPCC estimated that human activity caused about 1 ℃ global warming above pre-industrial levels, and is likely to reach 1.5 ℃ between 2030 and 2052 if it continues to rise at the current rate (IPCC, 2018). Therefore many measures need to be taken to achieve goals of the Paris Agreement, such as increasing the share of global energy consumption by renewable energy. Carbon capture, utilization, and storage (CCUS) is one of the essential measures to be taken to achieve these goals.

CCUS is the method of trapping CO_2 from major emission sources, such as cement plants or power plants, and using it in one of the technologies shown in Figure 2 or storing it by injecting into deep saline aquifers or depleted oil and gas fields.

Three leading technologies are available to capture CO_2 from large emission points.

- Pre-combustion: Upon combustion, this system captures CO_2. Syngas (composed mainly of carbon monoxide and hydrogen) is formed by the addition of steam or oxygen to the primary fuel. The water-gas shift reaction then transforms CO to CO_2 and H_2 by adding heat (Jansen et al., 2015).
- Oxy-fuel: During combustion, this system captures CO_2. Pure oxygen is used instead of air for combustion. Therefore a flue gas consisting of H_2O and CO_2 is formed, thus allowing for simple purification of CO_2. The flue gas produced is circulated to control the temperature of the boiler (Gerbelová et al., 2017).
- Post-combustion: After combustion, this technology captures CO_2 and is the most mature technology. Capture CO_2 from the soot by chemical absorption, such as NH_3 or Amine (Cuccia et al., 2018).

The CO_2 must be compressed into liquid form after capture and transported by pipeline or boats to storage site, and pumped into a geological reservoir in a safe manner. There are generally four main mechanisms for trapping (Figure 1):

- Structural and stratigraphic trapping: An impermeable rock in the top of the reservoir traps CO_2.
- Residual trapping: CO_2 is trapped in rock pores by capillary pressure (Zulqarnain et al., 2018).
- Dissolution trapping: CO_2 dissolves into the surrounding brine water and decreases the brine pH (Chen et al., 2018).
- Mineral trapping: This trapping mechanism is the safest and the most permanent. CO_2 is trapped by reacting with calcium and/or magnesium to form carbonate minerals (Liu & Maroto-Valer, 2014).

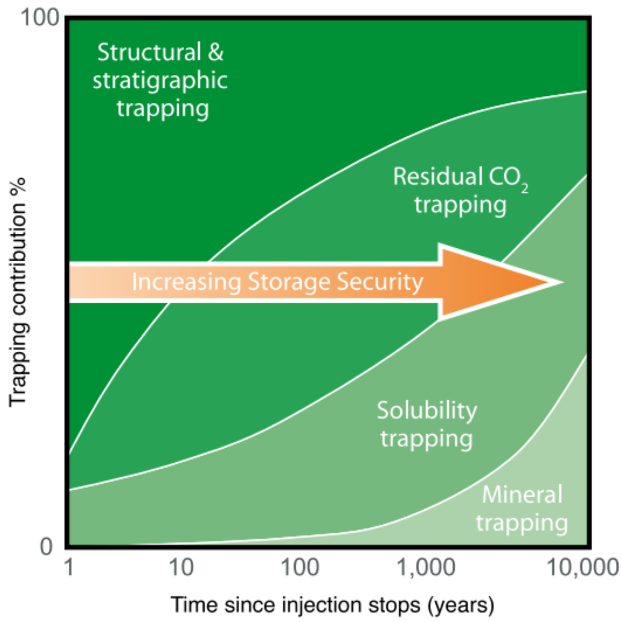

Figure 1: The security of storage for both the physical and the geochemical processes increases over time (IPCC, 2005).

The Sleipner injection project, with more than 16 million tons (Mt) of CO_2 injected since 1996, is the world's first offshore industrial CCS plant. The Sleipner Vest Field had 9 mole percent CO_2 content, which was higher than the 2.5 mole percent CO_2 export quality requirement. In order to avoid significant emissions, meet the criteria of selling gas, and as a response to the Norwegian CO_2 emission taxes, Statoil and partners have performed the CO_2 extraction using an amine plant. The CO_2 was then injected back into the saline aquifer of the Utsira formation, which was highly porous (Baklid et al., 1996; Furre et al., 2017; Hansen et al., 2005). A similar project also started in the Norwegian North Sea in April 2008, CO_2 has been injected into the sandstone saline Turbåen formation aquifer in the Snøhvit field (Shi et al., 2013).

In 2005, the Norwegian CLIMIT program for research, development, and demonstration of CCS was established. The program is conducted in collaboration between Norway's Research Council and Gassnova, providing financial support for CCS technology research, development, pilots, and demonstration (Bekken et al., 2013). In 2017 Equinor launched the Northern Lights project on behalf of Gassnova. The project will transport and store the CO_2 from the cement factory in Norcem and Fortum Oslo Varme Klemetsrud in the Johansen formation offshore Western Norway.

The Norwegian Petroleum Directorate (NPD) has prepared the CO_2 Storage Atlas of the Norwegian part of the North Sea to provide data on where secure long-term storage of CO_2 can be applied and how much CO_2 can be stored in saline aquifers, depleted hydrocarbon fields and producing fields using enhanced oil recovery (EOR) (NPD, 2011).

The high cost of carbon capture and storage is the main barrier to its widespread deployment at power plants and other industrial facilities (IPCC, 2014). Several CO_2 utilization technologies are being developed to facilitate the beneficial use of captured CO_2, as shown in Figure 2. A major option to solve this problem is CO_2 for enhanced oil recovery (EOR). Not only can oil fields provide revenues to offset the costs of capturing CO_2, but they can also provide secure and well characterized sites for storing CO_2 (Kuuskraa et al., 2013).

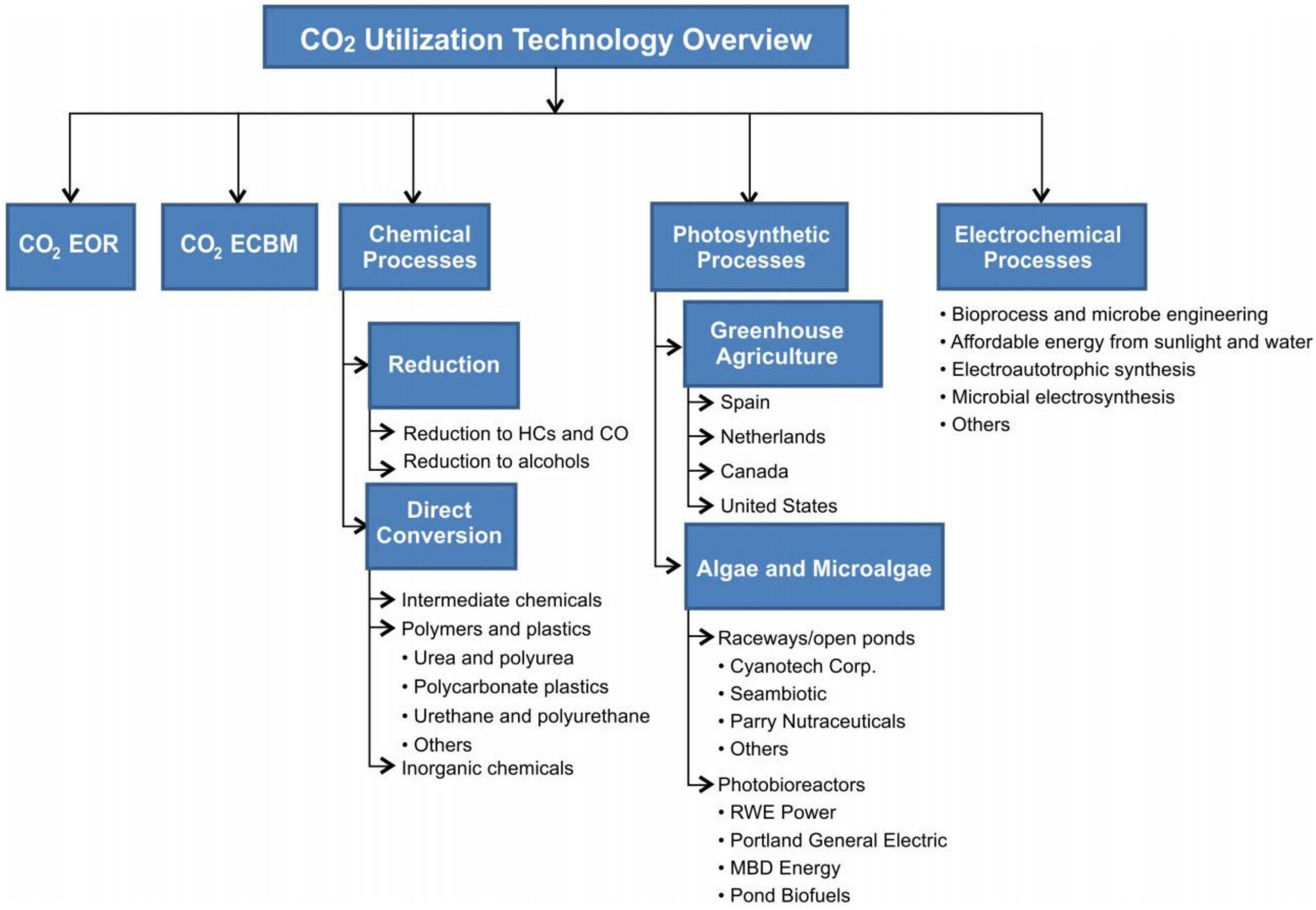

Figure 2: Overview of CO_2 utilization technologies. In addition to EOR, and enhanced coalbed methane (ECBM), other utilization technologies are under development. Mineralization to form carbonate or bicarbonate solid from CO_2 that may be used in construction materials. Produce useful fuels and chemical feedstocks as polycarbonate plastics or urea. Photosynthesis-based technologies that reduce the carbon in CO_2 to organic carbon for use as food, fuel, or a chemical feedstock (Laumb et al., 2013).

A comparison between CO_2 sequestered via CCS, EOR, and other utilization technologies are shown in Figure 3. The comparison shows the importance of CO_2-EOR and the potential it has to materially contribute to the sequestration of CO_2, whereas the contribution of carbon, capture, and utilization (CCU) is negligible. The scale is the key to climate change mitigation. Whilst CO_2 for EOR projects can be deployed at a sufficient scale, the same is not valid for the majority of CCU technologies (Mac Dowell et al., 2017). However, despite the importance of CO_2 for EOR to limit warming to the 2 ℃ target of the Paris agreement, the deployment is lagging far behind estimates of what is required. Analyses estimate that 200–1000 metric tons per year of anthropogenic CO_2 will be required to be captured and injected into geological formations for sequestration by 2030 to meet the Paris target. By 2050, 5000-10 000 metric tons per year will be required, while only ~ 30 metric tons per year of CO_2 is currently captured and stored in geological formation (Edwards & Celia, 2018).

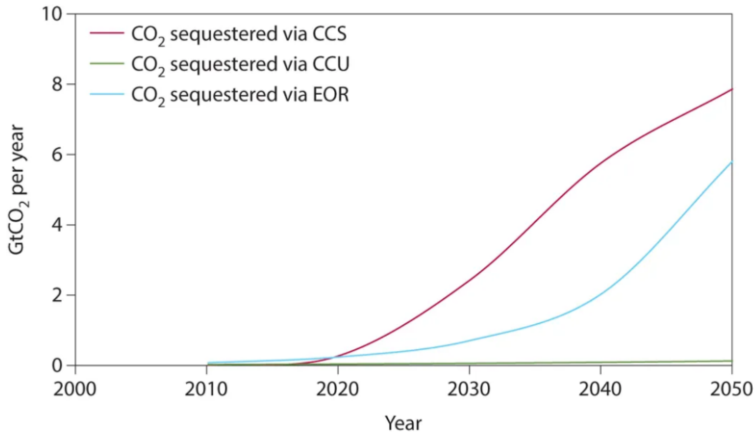

Figure 3: CCS versus CCU- a perspective for the period 2010 to 2050. Shows the importance of CO_2-EOR and the potential it has to materially contribute to the sequestration of CO_2 in the coming years, whereas the contribution of CCU is negligible (Mac Dowell et al., 2017).

CCUS has great potential in the oil and gas industry, and there are many ongoing projects aiming to advance the technology of CO_2 foam for CO_2 storage as a part of CCUS. The high mobility of CO_2 is the main problem in CO_2 injection into a reservoir, and it leads to poor mobility control and early breakthrough. In order to decrease the CO_2 mobility, foaming agents (i.e., surfactant or nanoparticles) can be used to generate CO_2 in brine foam. The aim of this thesis is to study the effect of these foaming agents quantitatively in the pore-scale in the absence of oil and to develop an experimental apparatus to study calcite precipitation and dissolution at the pore-scale during CO_2 storage in carbonate reservoirs.

This thesis consists of Five parts. Part 1 presents the motivation behind this thesis and gives a general understanding of the reservoir physics describing the relevant pore-scale mechanisms. Part 2 explains the experimental setups, procedures used, and the image analysis tools developed during this thesis. The results from the experiments are analyzed with the developed software, and are presented and discussed in Part 3. Part 4 provides the conclusions drawn based on the results obtained and propose further work. Part 5 presents the data obtained and the software script. The references are listed at the end.

2. Fundamental Reservoir Principles

Fundamental petrophysical principles and parameters must be reviewed in order to understand CO_2 flow patterns, foam generation and decay, calcite precipitation and dissociation.

2.1 Porosity

Porosity is a measure of the porous medium ability to store fluids. The sedimentary rocks consist of cemented matrixes and void space (pores). The pores are filled with fluids (liquids or gases), and absolute porosity is a dimensionless parameter defined as:

$$\phi_A = \frac{V_p}{V_t} \times 100\% \tag{1}$$

where:

ϕ_A = Absolute porosity

V_p = The pore volume

V_t = The matrix volume

Effective porosity is related to the pores that are connected and can contribute to fluid flow through the porous medium. This porosity is the porosity of interest when studying flow in porous media, and is defined as:

$$\phi = \phi_{tot} - \phi_{res} \tag{2}$$

where:

ϕ = Effective porosity

ϕ_{tot} = Total porosity

ϕ_{res} = Residual porosity (the portion of volume where the pores are not connected together)

The two-dimensional (2D) silicon wafer micromodel used in this thesis (described in detail in Chapter 6.3.1) enables direct visual of grains and pores; hence, the porosity can be calculated by analyzing micromodel images. Image analysis is required due to difficulties associated with performing accurate volume-based calculations because the micromodel pore volume is very small compared to volumes in fluid connection points. The micromodel porosity calculated from image analysis is influenced by a shadowing effects (Buchgraber et al., 2012); to ensure the same shadowing effect, identical light settings on the microscope were used each time. The porosity was calculated by adding the grain area (silicon and/or calcite) and dividing it by the image area, as shown in Equation (3):

$$\phi = 1 - \frac{\sum_{i=0}^{n} A_i}{x * y} \tag{3}$$

where:

A_i = Area of grain i [Pixels^2]

x = Width of the picture [Pixels]

Y = Height of the picture [pixels]

2.2 Fluid Saturation

If the pore volume is filled with a mixture of *n* fluids, the volume can be expressed as:

$$V_p = \sum_{i}^{n} V_i \tag{4}$$

The saturation of each fluid is defined as the volume fraction of that fluid to the pore volume

$$S_i = \frac{V_i}{V_p} \tag{5}$$

where:

S_i = Saturation of fluid i

V_i = Volume of fluid i

From Equation (5) the saturation to each fluid can only be between 0 and 1, and the sum of saturation to all fluids in the pore volume is 1.

2.3 Permeability

Permeability (K) is the ability of a porous medium to conduct fluid flow. The absolute permeability can be measured when the saturation of the medium is 100 % of one fluid. For horizontal, steady-state, viscous and laminar flow, the empirically derived formula (Darcy law) is defined as:

$$Q = \frac{K \times A \times \Delta P}{\mu \times l} \tag{6}$$

where:

Q = Volumetric flow $[m^3]$

K = Absolute permeability $[m^2]$

A = Cross-section (width × depth) $[m^2]$

ΔP = Differential pressure across the micromodel $[atm]$

μ = Viscosity $[Pa \times s]$

l = Length of the micromodel $[m]$

The permeability is a property of the medium, and it is independent of the fluid as long as the flow rate is proportional to the pressure gradient. It is common to use gases to measure permeability, and due to the compressibility of gases, the flow rate will depend on the pressure gradient. The permeability of gases is approximately a linear function of the reciprocal mean pressure, and the system permeability can be found by extrapolating the gas permeability to infinite pressure. This effect can be explained by the slippage phenomenon, which is closely related to the mean free paths of the gas molecules (Klinkenberg, 1941).

Darcy's law is insufficient to describe high-velocity gas flow in high permeable porous media. Forchheimer added a drop, which is proportional to the square of the velocity, to the pressure drop predicted by Darcy's law (Forchheimer, 1901; Zeng & Zhao, 2008). The Forchheimer equation is defined as:

$$-\frac{dp}{dx} = \frac{\mu}{k} v + \rho \beta v |v| \quad (7)$$

where:

$\frac{dp}{dl}$ = Pressure Drop across Sample

v = Velocity

β = Forchheimer factor

ρ = Density

When several immiscible fluids are present in a porous medium, they will influence each other, and the permeability for each fluid is defined as the effective permeability:

$$u_i = -\frac{K_i}{\mu_i} \times \nabla(p + \rho g z) \quad (8)$$

where:

K_i = The effective permeability of fluid i

p = Pressure

g = The gravity constant

z = Height

For practical purposes, the relative permeability for each fluid is defined as:

$$K_{ri} = \frac{K_i}{K} \quad (9)$$

where:

K_{ri} = Relative permeability of fluid i

The relative permeability depends on the wettability, that is a surface property of the rock. Common wettability preferences are hydrophobic and hydrophilic. Figure 4 shows that the endpoint relative permeability for water in a strongly hydrophilic system is relatively low for an imbibition process (is the process when the wetting phase displace the non-wetting phase) because of high friction between water and the rock grains (Anderson, 1987b) (Figure 5). For a hydrophobic system, the endpoint relative permeability to water is relatively high for a drainage process (is the process when the non-wetting phase displace the wetting phase) because of the absence of friction between water and the grains in such systems (Figure 5).

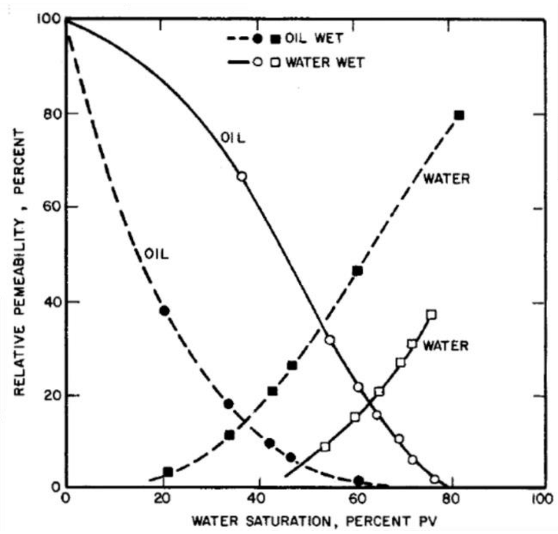

Figure 4: Steady-state oil/water relative permeability measured with heptane and brine in hydrophilic and hydrophobic synthetic Alundum core. The oil-wet core was treated with organo-chlorosilanes (Anderson, 1987a)

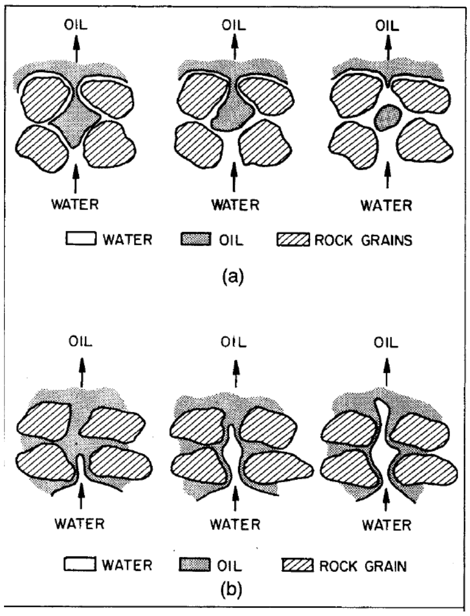

Figure 5: Water displacing oil from a pore during a waterflood: (a) strongly water-wet, (b) strongly oil-wet rock (Anderson, 1987b)

3. CO_2 for Foam Mobility Control

3.1 CO_2 Emissions

In recent years, massive amounts of CO_2 have been emitted, significantly more than the other greenhouse gases, as shown in Figure 6. CO_2 emissions have increased rapidly since the industrial revolution. Figure 7 shows the increase in the atmospheric concentration of CO_2 since 1959.

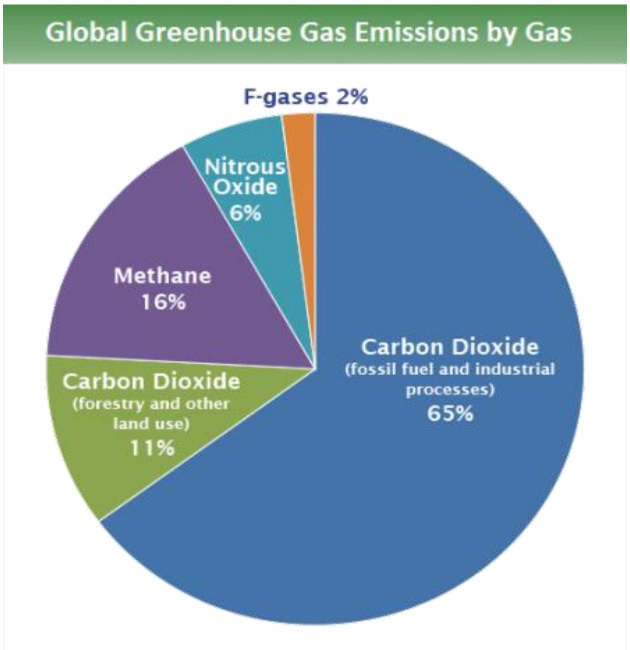

Figure 6: Global greenhouse gas emissions by gas from 2010. CO_2 emissions in total was 76 % of the total global greenhouse gasses emitted in 2010 (EPA, 2019).

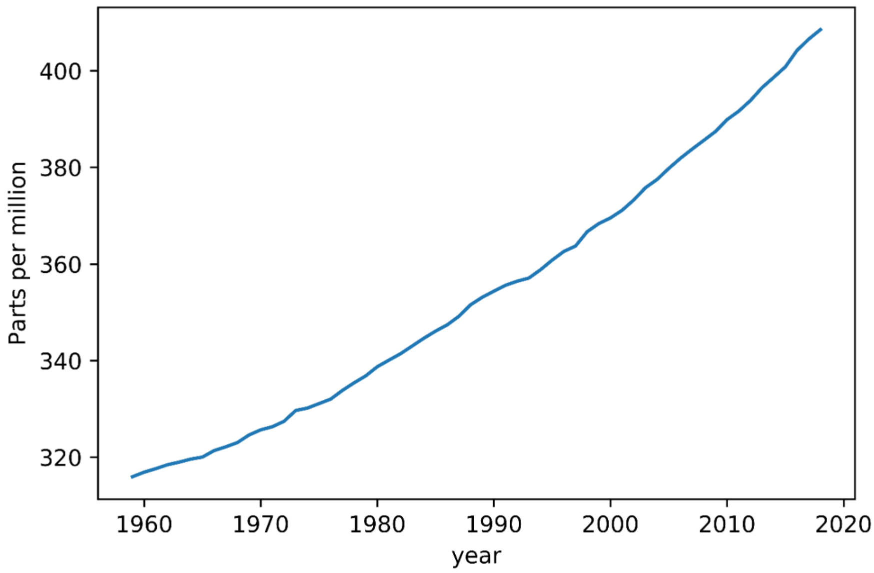

Figure 7: Atmospheric CO_2 annual mean concentration measured at Mauna Loa observatory, Hawaii. CO_2 Concentration was 316 ppm in 1959 and measured in 2018 to be 409 ppm. Modified from (Tans & Keeling, 2019).

3.2 Physical Properties of CO_2

In atmospheric conditions (1 atm and 20 °C), CO_2 is in gaseous form, and it consists of one carbon atom and two oxygen atoms. CO_2 is either in liquid or supercritical phase at subsurface storage conditions in the reservoir (see Figure 8). In this thesis, CO_2 will be used in the supercritical phase in the calcite dissolution experiments, and in the liquid phase in the CO_2 foam experiments. CO_2 has unique properties in the supercritical phase with a liquid-like density and a gas-like viscosity. These properties make it very efficient (with other favorable properties described below) for secondary and tertiary oil recovery applications.

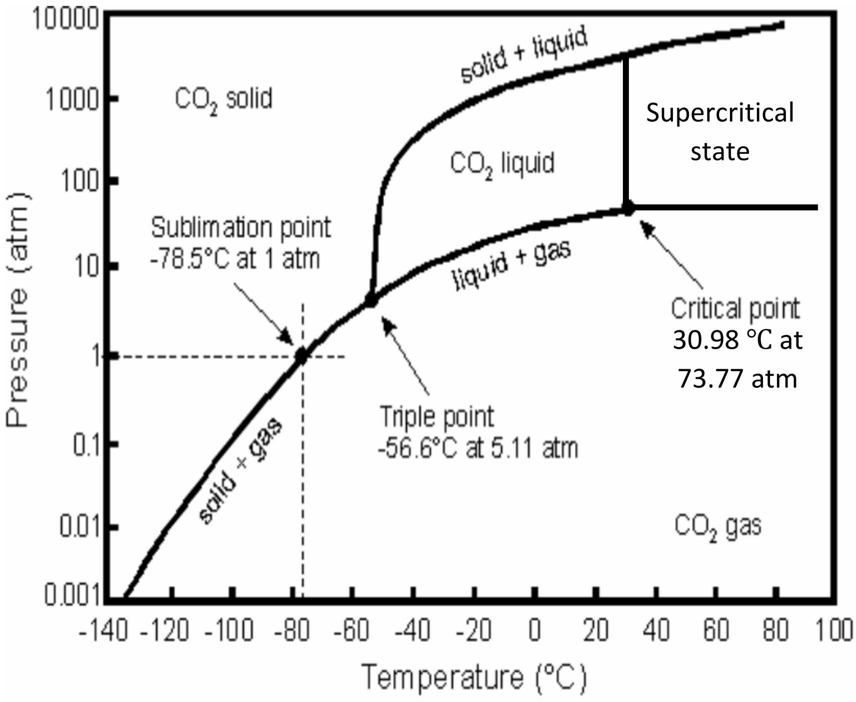

Figure 8: CO_2 phase diagram. shows the state of CO_2 for varying temperatures and pressures. At temperatures above the critical temperature, CO_2 vapor cannot be in the liquid state, but only in the supercritical state when the pressure exceeds supercritical pressure. Modified from (Picha, 2007)

3.3 CO_2 for EOR

CO_2 has many favorable properties relating to secondary and tertiary oil recovery applications. Such properties include swelling of the oil, miscibility, oil density rise, high water solubility, and interfacial tension (IFT) reduction (Bahadori, 2018; Enick et al., 2012; Firoozabadi & Myint, 2010).

The solubility of CO_2 in oil leads to a volume increase of the oleic phase, termed oil swelling, by as much as 50-60%, swelling leads to increased relative permeability and mobility, resulting in increased oil recovery (Firoozabadi & Myint, 2010). The swelling of the oil and reduction in viscosity result from the reduction of IFT between CO_2 and oil (Enick et al., 2012). Since the density of CO_2 at reservoir conditions is similar to a liquid, the CO_2 becomes less prone to gravity separation, and this leads to a more efficient vertical sweep efficiency. IFT between oil and CO_2 is significantly reduced due to the relatively low minimum miscibility pressure (MMP) of CO_2. MMP is the pressure where miscibility occurs (Bahadori, 2018). Miscible and near-miscible displacement may increase the recovery by up to 18% compared to an immiscible displacement (Kamali et al., 2015).

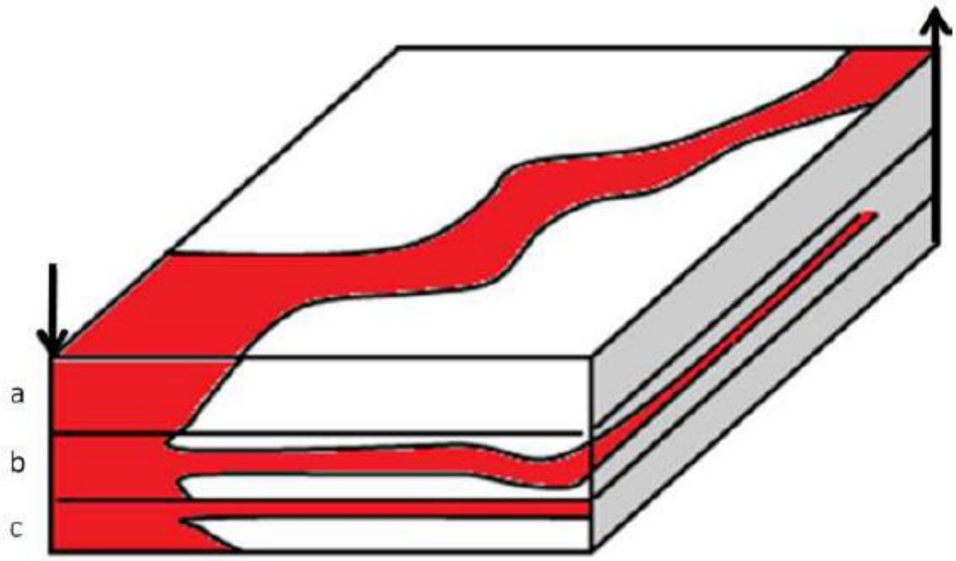

Figure 9: Red represents injected CO_2, and white is the reservoir matrix. Disadvantages of CO_2 EOR: (a) poor area sweep efficiency, (b) gas channeling, and (c) gravity override (Hanssen et al., 1994).

Despite achieving high microscopic sweep efficiency (mobilization of oil at pore scale) by miscible injection of CO_2, the volumetric sweep efficiency (the fraction of the floodable pore volume swept or contacted by the injected water (Cobb & Marek, 1997)), and gas utilization are limited (Figure 9). This limitation is due to the low viscosity and density of CO_2 that result in an unfavorable mobility ratio leading to gas channeling, early CO_2 breakthrough, high CO_2 production relative to oil, and gravity override. Several technical solutions have been developed to avoid these problems, mobility reduction by reducing its relative permeability through water-alternating-gas injection strategies, to increase its viscosity by adding polymers or to decrease its mobility by adding surfactants and/or nanoparticles to generate CO_2 in brine foams or CO_2 in oil foams (Enick et al., 2012).

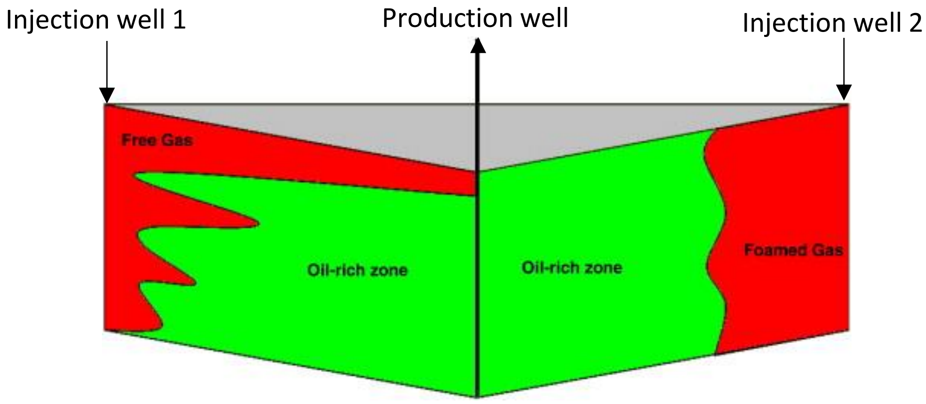

Figure 10: Gas flooding (injection well 1) vs. foam flooding(injection well 2): foaming of the gas modifies its profile by lowering gas mobility. Modified from (Farajzadeh et al., 2012).

Eventually, gas or water injection for EOR faces gravity segregation. Density variations will force the gas to mitigate upwards, sweeping the upper part of the reservoir, whereas the water will be forced to sweep the bottom part of the reservoir. Field and laboratory CO_2 foam studies have shown that foam can reduce the mobility of CO_2 and diminish the effects of gravity override, viscous fingering, and channeling in high permeable layers (Zuta et al., 2009). As shown in Figure 10, this leads to a more piston-shaped front leading to an increase in oil production and CO_2 storage.

3.4 Characteristics of Foam

Foam is defined as a dispersion of gas-liquid where the liquid is the continuous phase, and the gas is the phase of discontinuity (David & Marsden, 1969). The correct scientific term is CO_2 emulsion because in reservoir conditions the CO_2 will be in liquid form, but CO_2 foam is the name used in the literature and will be used throughout this thesis. Generally, the continuous phase is water in a hydrophilic surfaces. CO_2 is the discontinuous phase, separated by a thin, continuous film called lamella (see Figure 11 and Figure 12), whereas a three-lamellae link is referred to as a plateau border (Schramm, 1994).

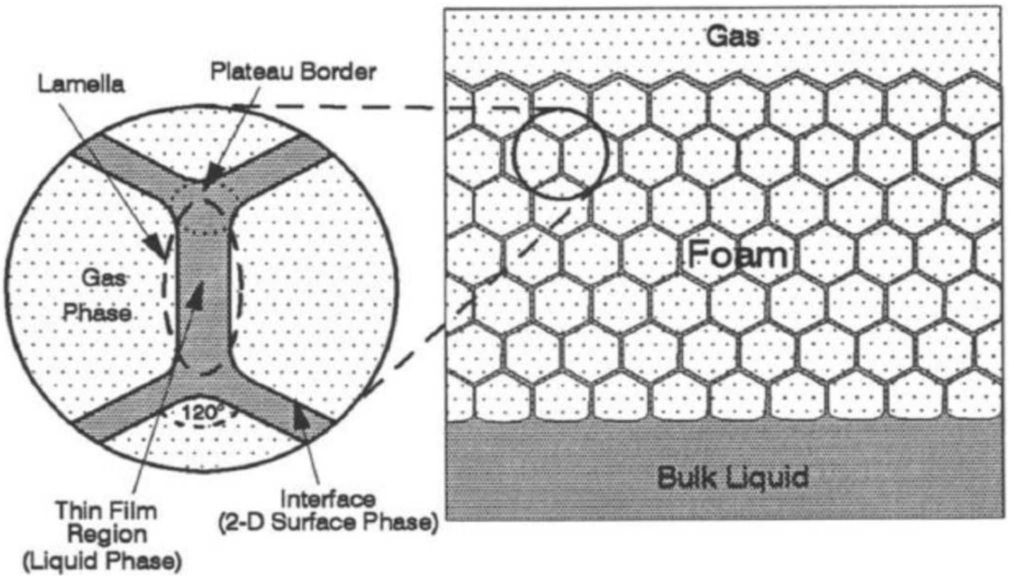

Figure 11: A 2D illustration of foam, where the zoomed section shows the definitions of foam structure (Schramm, 1994).

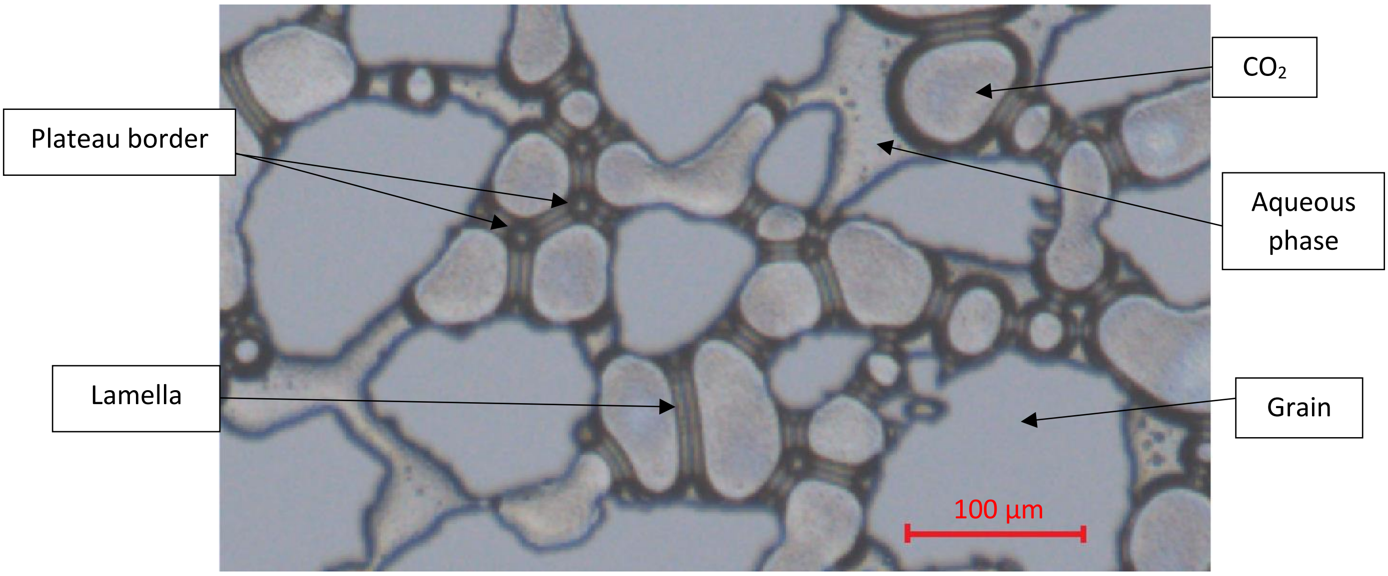

Figure 12: A 2D image of CO_2 foam in a micromodel, showing the lamella and the plateau border.

Foams are common substances created in the kitchen sinks by combining air, water, and soap. Foam is an unstable thermodynamic system (Zhang et al., 2020) due to liquid gravity segregation. Foam can be stable, when gas bubbles are released faster than the fluid between bubbles can drain away. Typically a foaming agent is used to achieve foam stability by reducing the IFT, improving the generation, stability, and lifetime of the foam (Schramm, 1994). The foaming agents used in this thesis are surfactants and/or nanoparticles, and they will be described in the following subchapters.

3.5 Foam Generation

Two methods can be used to generate foam in porous media, either by co-injection of gas and slug solution (brine + foaming agent) or by alternating injection method known as surfactant alternating gas (SAG). Three fundamental foam generation mechanisms at the pore level have been identified:

- Leave-behind: Generates bubbles as two gas fronts from different directions invade the same pore space filled with liquid. Then the two gas fronts squeeze the liquid into a lamella in the pore space (Ransohoff & Radke, 1988). Foams generated by this mechanism alone may be considered weak even though they would block many flow paths, they will also provide some continuous gas flow paths (Enick et al., 2012).

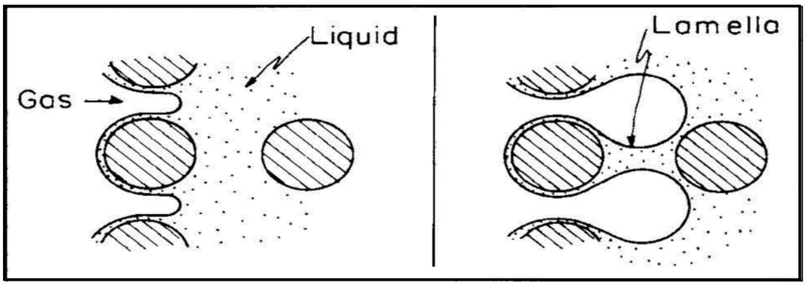

Figure 13: Illustration of foam formation by the leave-behind mechanism (Ransohoff & Radke, 1988).

- Snap-off: Takes place as the non-wetting phase moves through a narrow pore throat and displaces the wetting phase. The bubble will be snapped off when the differential pressure across the interface at the pore throat is higher than the leading interface pressure. This mechanism is considered the primary mechanism for the generation of foam, and in the presence of a foaming agent generates a strong foam (Ransohoff & Radke, 1988).

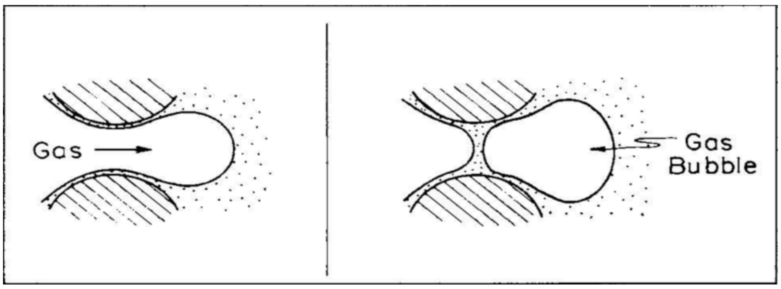

Figure 14: Illustration of foam formation by the snap-off mechanism (Ransohoff & Radke, 1988).

- Lamella-division: Also referred to as secondary foam generation as it occurs only when the foam is already present and flows through the porous media (Ransohoff & Radke, 1988). It must either break or span the throats when a single mobile lamella crosses a branch point. This mechanism also generates a strong foam as the snap-off mechanism, as these two mechanisms generate films perpendicular to the flow direction (Enick et al., 2012).

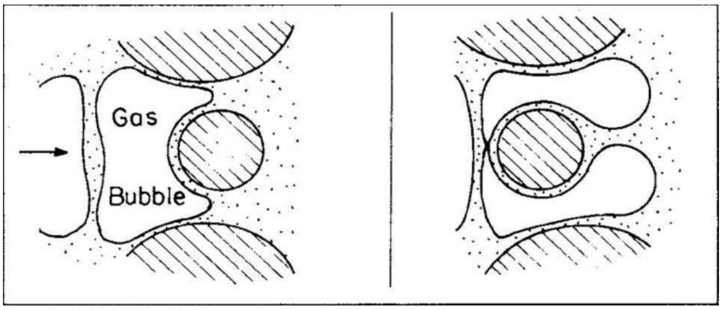

Figure 15: Illustration of foam formation by the lamella-division mechanism (Ransohoff & Radke, 1988).

3.6 Destabilization of Foams

As mentioned, foam is thermodynamically unstable and will eventually collapse. Figure 16 shows the various stages that foams can experience as they mature and eventually are destroyed

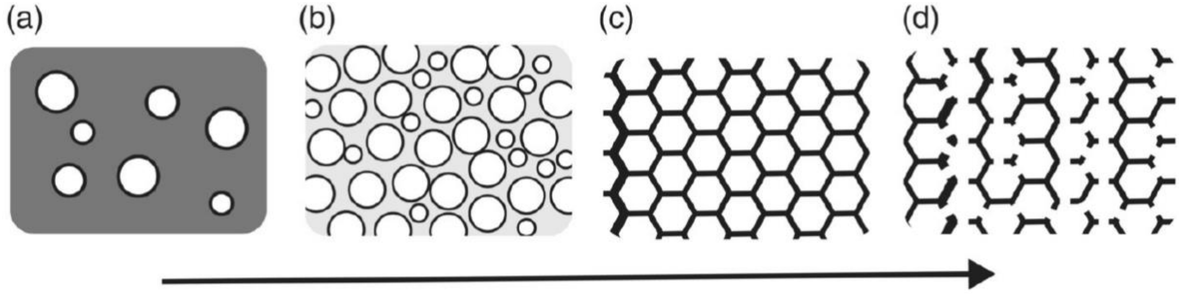

Figure 16: illustration of foam lifetime. (a) spherical foam (independent gas bubbles), (b) gravity drainage period, (c) lamella thinning period, and (d) film rupture (Kontogeorgis & Kiil, 2016).

There are three main mechanisms of foam destabilization:

- Gas diffusion: Due to surface tension, the pressure inside a bubble and between two bubbles in the film is higher than the pressure in the plateau border. This pressure difference in the plateau border sucks the liquid out from lamellae films, which can lead to rupture (Kontogeorgis & Kiil, 2016).

- Lamella rupture: It occurs because of surface waves (fluctuation). In pure water, rupture takes place when the film is 100-400 nm thick, but using a surfactant can reduce the rupture thickness to 5-15 nm (Kontogeorgis & Kiil, 2016).

- Gravity drainage: This mechanism is the fastest of the destabilization mechanisms, and if the foam has not stabilized, this mechanism will lead to total collapse before other mechanisms can become important (Kontogeorgis & Kiil, 2016). The liquid phase drain to the bottom, and the film thickness in the top part becomes thin, which can lead to rupture.

3.7 Foaming Agents

3.7.1 Surfactant-Stabilized CO_2 Foam Flooding

The surface-active agent known as surfactant is used mainly to reduce IFT between oil and water to remobilize the capillary-trapped oil. Because of their hydrophilic and hydrophobic part molecules, they adsorb to the gas-liquid interface and lower IFT, resulting in stable foam (Lake et al., 2014)

The rule of Bancroft states that the phase in which the surfactant is soluble will constitute the continuous phase (Ruckenstein, 1996), and therefore the surfactant should be soluble in brine in order to obtain CO_2 in brine foam. There are four types of surfactants that are distinguished by the electric charge; anionic, cationic, nonionic, and zwitterionic. Sandstone has a negatively charged surface, and therefore the cationic surfactant with a positively charged head group should be avoided because it will adhere to the rock instead of generating foam (until rock adsorption is satisfied). A nonionic, water-soluble surfactant (SURFONIC L24-22) is used in this (Huntsman, 2019). As temperature increases, most surfactants become less soluble in brines, so they should be tested at reservoir temperatures. Surfactants are often used in porous medium to improve foam generation and stabilization (Enick et al., 2012).

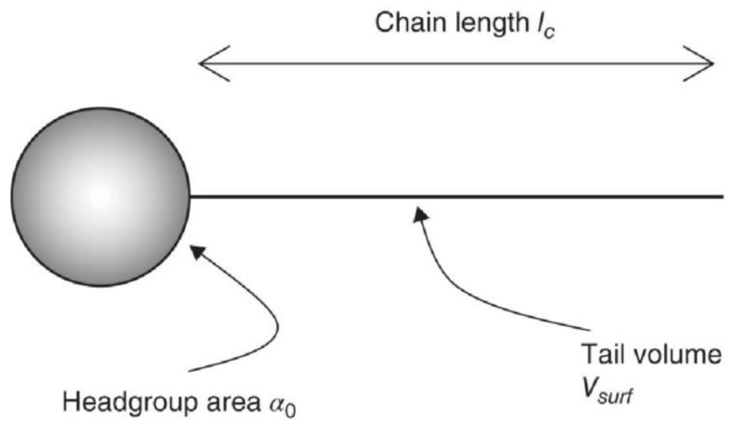

Figure 17: Illustration of surfactant. It consists of a hydrophobic part and a hydrophilic part (Kontogeorgis & Kiil, 2016).

3.7.2 Nanoparticle-Stabilized CO_2 Foam Flooding

Due to the instability associated with surfactants at harsh reservoir temperatures, interest in nanoparticular-stabilized CO_2 foam has arisen in recent years (Bennetzen & Mogensen, 2014). results Rognmo's results show that surfactant-stabilized foams are several times stronger than nanoparticle-stabilized foams during foam scans without oil, but in the presence of crude oil, surfactant-stabilized foams collapse while nanoparticles displayed stabilizing effects (Rognmo, 2019). The ability to stabilize foam in the presence of oil makes nanoparticles very interesting in a CCUS context. Silica nanoparticles are environmentally friendly as they constitute a natural part of the reservoir, making them particularly attractive as EOR foaming agents (Skauge et al., 2010).

Nanoparticles are defined as particles with a size ranging from 1-100 nm and properties different from those found in the bulk of the material due to their high surface-to-volume ratio (Auffan et al., 2009). It may not seem possible to inject an aqueous dispersion of particles into a porous medium. It is easy to imagine particles being too large to enter the pores or stuck in small pores. The nanoparticles used in this technology are too small to strain or block pores and flows smoothly through the porous media (Enick et al., 2012; Skauge et al., 2010). The nanoparticles used in this thesis is Levasil CC301, it is a neutral, 28 wt% aqueous dispersion of colloidal silica: *"Nanoparticle A (NPA) is a commercially available silane modified colloidal silica, Levasil CC301 (AkzoNobel). The modification produces a hydrophilic surface and a steric stabilization, resulting in an increased salt stability compared with unmodified silica particles. The discrete* SiO_2 *particles have a smooth, spherical shape with diameter 23.3 nm (±7.9) measured with dynamic light scattering (uncertenty is given as one standard deviation)"* (Rognmo et al., 2017).

4. Carbonate Reservoirs

Unlike siliciclastic rocks, carbonates are formed in situ instead of being composed by transported sediments. Chemical and organic processes form carbonates, with more variation in their shape than siliciclastic rocks. Approximately 60% of the world's oil reserves in carbonate reservoirs (Akbar et al., 2000). Throughout this thesis, different mechanisms will be studied at the pore-scale to study calcite precipitation and dissolution during CO_2 storage in carbonate reservoirs to give a better understanding of the patterns of reactivity and flow.

4.1 Formation and Deposition

4.1.1 Chemical Processes

The processes of chemical weathering expel chemical ions from the rocks of origin dissolving in lakes and oceans. Thus, water temperature and pressure contribute to the dissolution of source rocks. Increasing temperature or lowering pressure leads to CO_2 loss, resulting in increased water pH and carbonate mineral precipitation.

The equilibrium equation (10) shows the effect of CO_2 on the calcium carbonate ($CaCO_3$) accumulation. In the presence of a high concentration of CO_2, the $CaCO_3$ will dissolve, while in the case of loss of CO_2, the concentration of hydrogen ions decrease, and the pH increases.

$$H_2O + CO_2 + CaCO_3 \leftrightarrow Ca^{2+} + 2HCO_3^- \tag{10}$$

The reaction shifts toward the left, resulting in precipitation of $CaCO_3$ (Boggs, 2006)

4.1.2 Biogenic Processes

Organisms can support the chemical process. For example, extraction of $CaCO_3$ from seawater or freshwater, photosynthesis, and bacterial activity, are effects of organic activity on the precipitation of $CaCO_3$. Marine species such as foraminifers, corals, mollusks and algae absorb dissolved carbonate from the water to create skeletal structures. The carbonate layer is formed when the skeleton is buried, compacted, or lithified. In comparison to a sandstone rock, the various shapes and sizes of the skeleton can give a range of different types of pores.

As mentioned, the precipitation of carbonate can be facilities by removing CO_2 from the water. Photosynthesizing plants such as blue-green algae, Photosynthesizing bacteria, and coccoliths that remove CO_2 from the water are essential to the formation of carbonate (Boggs, 2006).

$$6H_2O + +6CO_2 \rightarrow C_6H_{12}O_6 + 6O_2 \tag{11}$$

The bacterial activity also promotes carbonate precipitation. In this thesis, Sporosarcina pasteurii bacteria were used to precipitate calcite minerals on the silica surface of pores in micromodel. The Sporosarcina pasteurii bacteria hydrolyze urea ($CO(NH_2)_2$) into ammonia (NH_3) and carbonic acid (H_2CO_3) (equation 12). This is followed by an increase in pH, due to production of (OH^-) (equation 13).The carbonic acid is converted to bicarbonate ions (HCO_3^-) as the pH increases (equation 14), thereafter forming carbonate ions (CO_3^{2-}) (equation 15). Eventually the precipitation of calcium carbonate ($CaCO_3$) starts in the present of calcium (equation 16) (De Muynck et al., 2010)

$$CO(NH_2)_2 + 2H_2O \rightarrow 2NH_3 + H_2CO_3 \tag{12}$$

$$2NH_3 + 2H_2O \leftrightarrow 2NH_4^+ + 2OH^- \tag{13}$$

$$H_2CO_3 + 2OH^- \leftrightarrow HCO_3^- + H_2O + OH^- \tag{14}$$

$$HCO_3^- + H_2O + OH^- \leftrightarrow CO_3^{2-} + 2H_2O \tag{15}$$

$$Ca^{2+} + CO_3^{2-} \rightarrow CaCO_3 \tag{16}$$

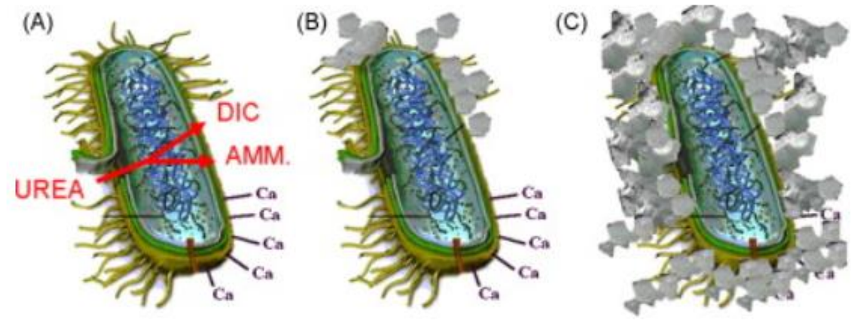

Figure 18: (A) shows positively charged calcium ions that are attached to the negatively charged bacterial cell wall. Bicarbonates ions and Ammonia are released in the microenvironment when urea is added. (B) Calcium carbonate precipitates on the bacterial wall, and after a while (C) the whole-cell becomes encapsulated, resulting in cell death (De Muynck et al., 2010).

4.2 Diagenesis

Diagenesis is the mechanism that describes physical and chemical changes in sediments induced by increasing temperature and pressure as they are buried. Most carbonates are deposited under marine environments. Sediments are subjected to a number of diagenetic processes after carbonate deposition, which can affect porosity, mineralogy, and chemistry. Porosity can either be decreased by cementation and compaction or increased by dissolution.

Subsequently, through boring, burrowing, and sediment-ingesting activities, the burial, organisms can rework sediment. These activities can alter the structure and leave organic traces behind. As the grains are cemented together and the porosity reduced, cementation is also an essential part of diagenetic processes. Cement from the seafloor is typically aragonite. Dissolution is also a critical part of diagenetic processes, particularly in carbonate reservoirs, as cementation. Carbonate mineral dissolution requires conditions other than cementation. Low pH pore waters, unstable minerals, and cold temperatures support dissolution. Equation (10) shows the process of dissolution of carbonate minerals. When fresh sediments are deposited, the stress is raised in the older sediments, resulting in compaction. The compaction leads to a reduction in porosity and bed thinning (Boggs, 2006).

5. Upscaling and Storage Security

5.1 Upscaling from Micro- to Field-Scale

It is vital to upscale from pore-scale to core-scale for better field-scale estimation methods for CO_2 storage security. Different mechanisms will be tested at pore-scale to give a better understanding of the patterns of reactivity and flow. In estimating long-term geological storage of CO_2 in carbonate reservoirs, the patterns of reactivity between CO_2 and carbonate, and flow are essential. 2D silicon micromodels allow direct visual observations of the reaction between the CO_2 saturated acidic fluid and calcium carbonate by conducting the investigations at the smallest scale relevant for the application of carbonate precipitation and dissolution. The micromodels have a controlled environment based on thin sections of realistic reservoir materials that will be explained further in the next chapter.

Using high-quality imaging of fluid flow paths using positron emission tomography (PET), quantitative analysis of core-scale dissolution structures (also referred to as Darcy-scale) will allow the evolving dissolution structure to be connected to the reaction fluid flow field. These data and data from pressure measurement can be used as input in simulation models. This will not be a part of my thesis, but will be conducted by Dr. Bergit Brattekås and MSc Torunn Veien.

Fluid flow is based on the determination of the field pilot's injection technique and the estimation of CO_2 diffusion in the reservoir. These models will also determine the structural integrity of storage formation and the sequestered CO_2 migration patterns in carbonate reservoirs for long-term secure geological CO_2 storage.

5.2 CO_2 Storage Security and Monitoring

For a minimum of 10 000 years, the CO_2 captured and stored must be securely isolated from the atmosphere and the ocean, so that CCS can contribute successfully to climate mitigation efforts. Migration of CO_2 to the surface would adversely affect the public perception of CCS as a technology for climate mitigation (Miocic et al., 2016). Fear of CO_2 leakage to the surface is actually the main driver of negative public opinion towards CCS and has led to delays in the development of storage projects (Mabon et al., 2014).

Considering storage security, the evaluation of CO_2 storage sites is critical. As a supercritical fluid, CO2 will be injected and stored (NPD, 2011). As stated above, the temperature and pressure required for obtaining a supercritical CO_2 are 30.98 ℃ and 73.77 atm, respectively. The reservoir depth must be chosen in order to meet these criteria. Another critical selection criteria are the presence of fractures or faults since CO_2 can migrate to the surface through it. Cap rocks should not have faults, and the capillary entry pressure of caprocks should be higher than the pressure increase induced by CO_2 injection (Miocic et al., 2016).

The monitoring of CO_2 injected at the storage site is necessary for two main reasons: firstly, to ensure that CO_2 is stored in the reservoir in compliance with plans and forecasts and, secondly, to provide information that can be used to update the reservoir models and to support potential mitigation steps when there are anomalies (NPD, 2011). Storage site monitoring should make a positive contribution to the public perception of CCS as a tool for climate mitigation. 4D seismic monitoring is an important CO_2 storage monitoring technology. Figure 19 illustrates how this technology was used in the previously described Sleipner project. Certain technologies include monitoring of temperature and pressure, CO_2 sensors on the surface, and monitoring of the seabed (NPD, 2011).

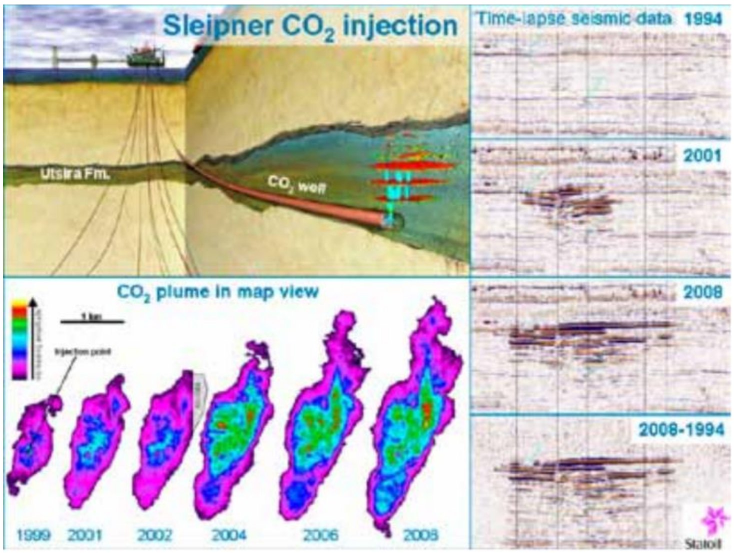

Figure 19: A sketch of the injection well and storage reservoir is shown in the upper left. To the right is a seismic section for a time-lapse difference. The first one is before the start of CO_2 injection, and the others are after. The lack of reflectivity on the seismic sections above the storage formation shows no sign of leakage. Sketch on the lower left shows the growth of the CO_2 plume through time(NPD, 2011).

Part II: Experimental Procedures

6. Experimental Setup and Equipment

6.1 Experimental Setup and Procedures

6.1.1 CO_2 Foam Setup and Procedures

Figure 20 shows the experimental setup for the CO_2 foam experiments, with the main elements described in detail in sub-chapters below. Initially, by using filtered, distilled water from the Quizix QX pump, the micromodel was pressurized to 100 bar, and injected liquids were produced through a back pressure regulator (BPR). The aqueous phase (brine and/or surfactant solution and/or nanoparticle solution) was then injected into the micromodel, and by closing inlet and outlet valves, the micromodel was isolated. Subsequently, CO_2 was injected via bypass to displace the aqueous phase in the lines, and a rate of 5 ml/ min was used to extract the aqueous phase from the filter so that during experiments foam does not generate in the filter. CO_2 was then pumped via bypass to the accumulator at a rate of 4 μl/min until the pressure in the pump was stable, then outlet and inlet valves were opened respectively and bypass closed.

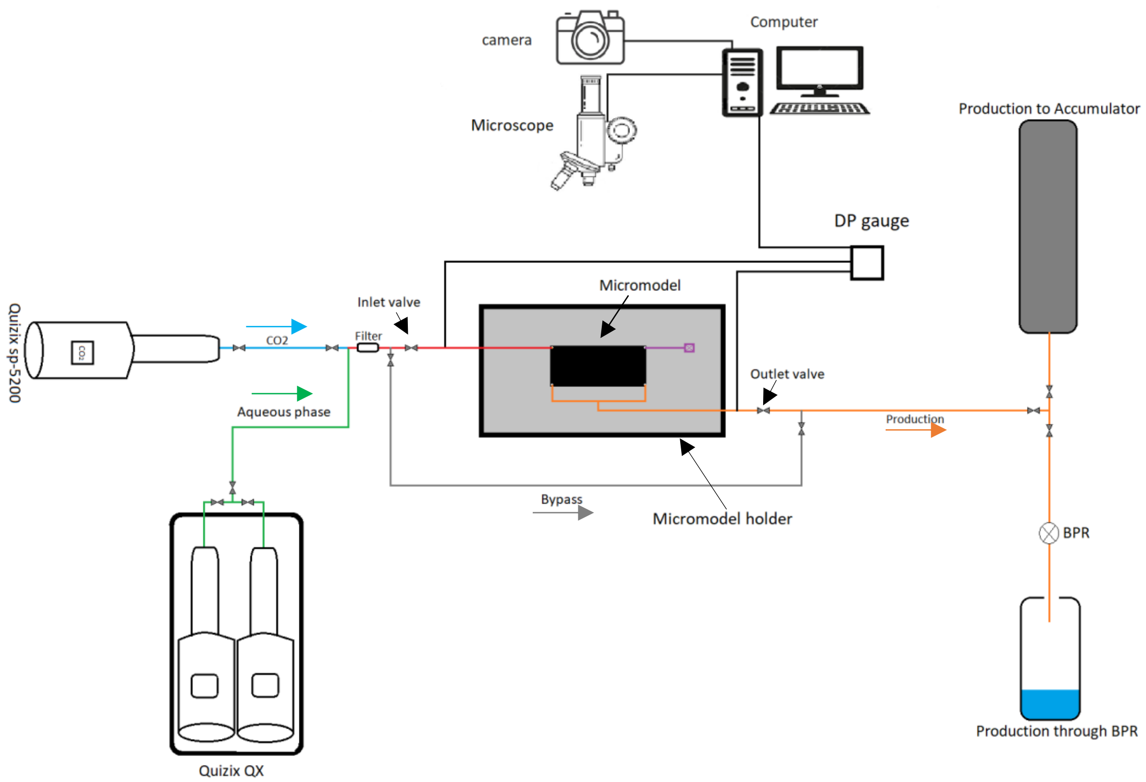

Figure 20: Sketch of the CO_2 foam experimental setup used in this thesis. A Quizix QX pump was used to inject aqueous phase (brine and/or surfactant solution and/or nanoparticle solution) and filtered, distilled water (the green line ahead of the filter), Quizix SP-5200 was used to inject CO_2 into the micromodel (the blue line ahead of the filter). Fluids were produced at 100 bar back pressure in the accumulator (orange line), and after each experiment, the accumulator was depressurized to 100 bar. After experiments, the fluids were produced through BPR (orange line). Bypass line (gray line) has been used in cleaning procedures of micromodel after each experiment. The port in the right upper corner is unused and plugged (purple line).

6.1.2 Calcite Precipitation and Dissolution Experimental Setup and Procedures

Figure 21 shows the experimental setup for calcite precipitation and dissolution, with the main elements described in detail in sub-chapters below. Initially, the micromodel was saturated with filtered, distilled water. The water was pumped from the Quizix QX pump through the green, and yellow tubing (Figure 21) to the micromodel, and the production was produced in the ambient production bottle. The viscosity of the water and the bacteria is approximately equal, hence a fully water-saturated micromodel is a good start point for even bacteria distribution. The bacteria and reactant solution were injected in the micromodel using a syringe pump through the purple tubing (Figure 21), and the production was produced in the ambient production bottle. For calcite dissolution, the Quizix SP-5200 pump was used to saturate the hydrochloric acid in the accumulator with CO_2 for 24h. The CO_2 saturated hydrochloric acid was then injected through the dark teal tubing, then the yellow tubing (Figure 21) to the micromodel, and the production were produced in the high-pressure production bottle.

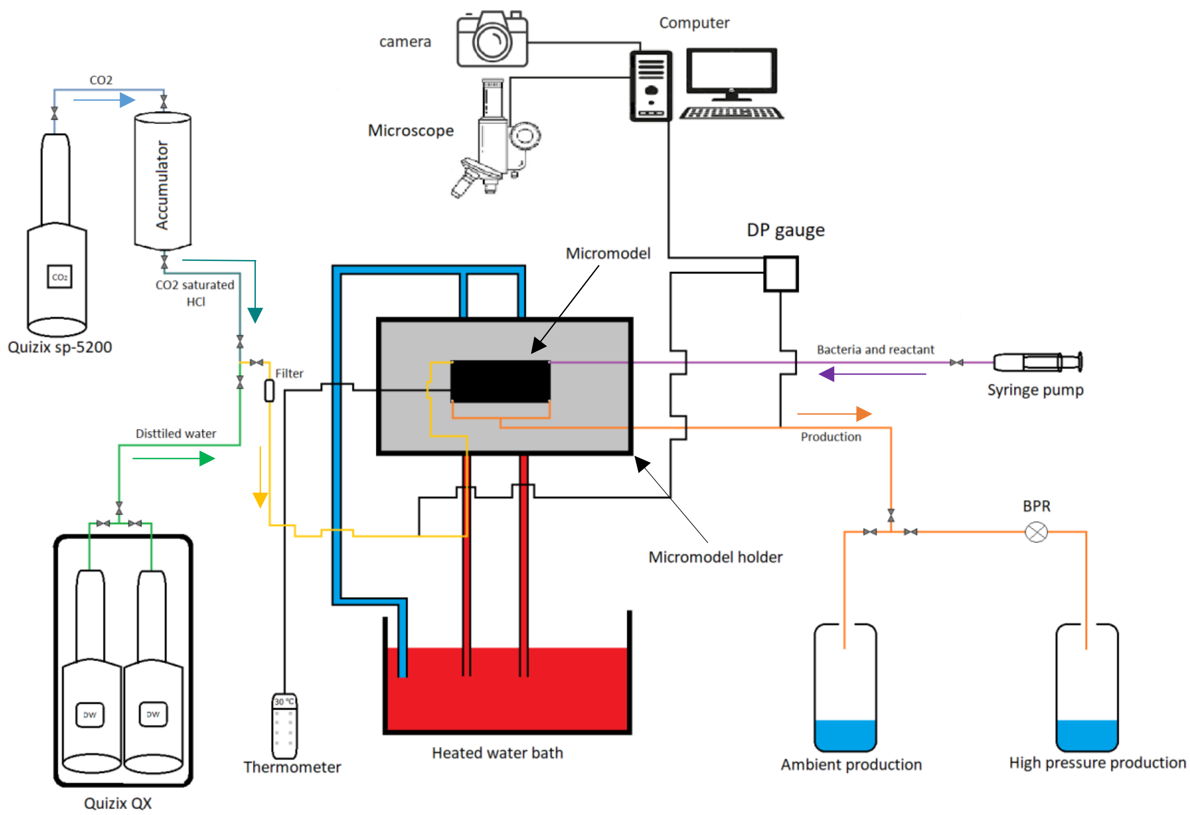

Figure 21: Sketch of the calcite precipitation and dissolution experimental setup used in this thesis. A Quizix QX pump was used to inject filtered, distilled water (the green line ahead of the filter), Quizix SP-5200 was used to inject CO_2 to the accumulator (blue line) then to the micromodel. The syringe pump was used to inject bacteria and reactant solutions (purple line). Bacteria, reactant, and filtered, distilled water were produced in ambient production bottle so that the system has atmospheric pressure, whereas CO_2 saturated hydrochloric acid was produced in high-pressure production bottle through BPR (was set to 100 bar).

6.2 Equipment

6.2.1 Micromodel

Precipitation and dissolution of carbonate were analyzed using a 2D micromodel with a synthetic porous medium. The bottom part of the micromodel is a silicon wafer that is anodically bonded to a smooth, optically transparent borosilicate glass. The fabrication steps are shown in Figure 22.

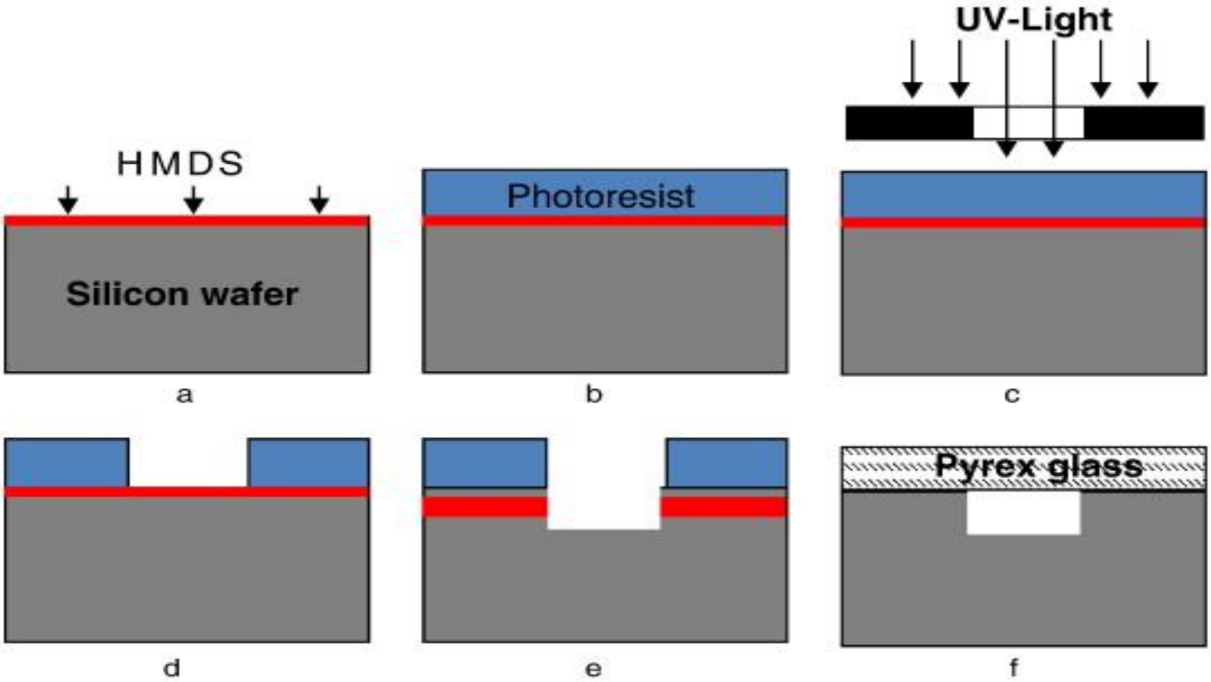

Figure 22: Micromodel fabrication process: (a) vapor prime hexamethyldisilane (HMDS) coating, (b) photoresist coating, (c) a mask is placed and the excess photoresist is removed, (d) the wafers are ready to be etched, (e) Hydrofluoric acid gasses etch the regions exposed to UV light to the desired depth (30 μm), and (f) anodic bonding of pyrex glass (Buchgraber et al., 2012).

The pore network and grain structures are based on thin sections of a real pore network (Buchgraber et al., 2012; Hornbrook et al., 1991). The micromodel height, width, and etching depth are 2.8 cm, 2.2 cm, and 30 μm, respectively. The pores and two channels (one at the top and the other at the bottom) allow transportation of fluid through the porous network, as shown in Figure 23. The micromodel has four ports on the backside of the silicon wafer, providing entry points for liquids to the micromodel (Figure 24).

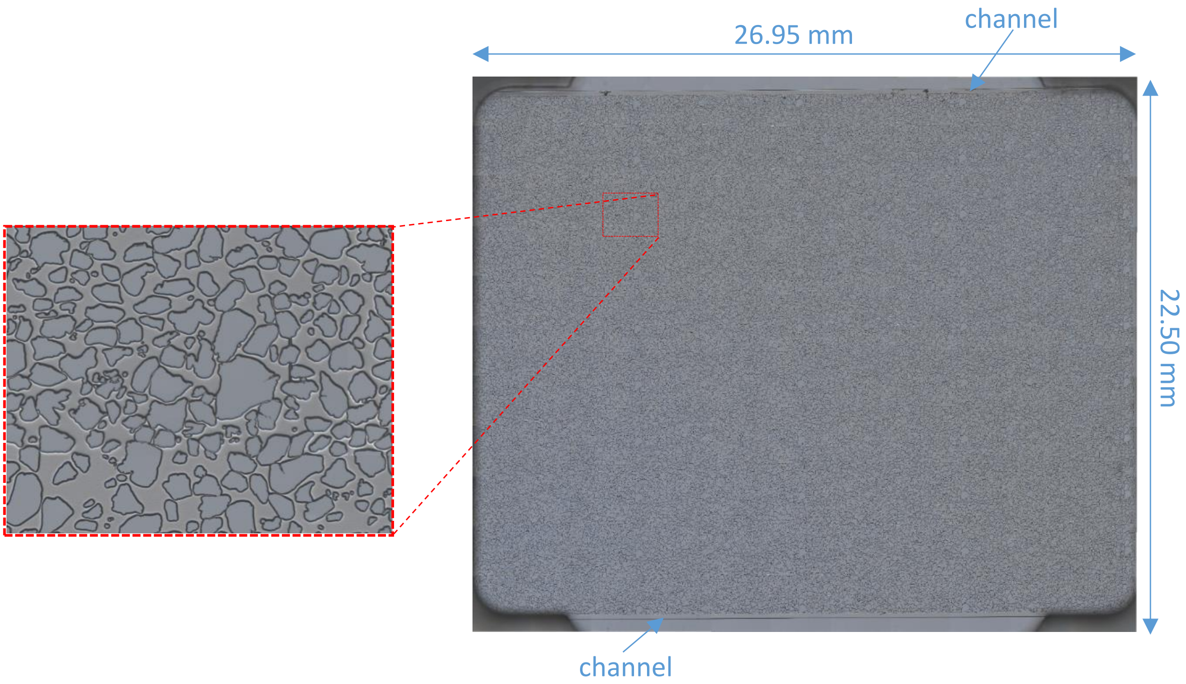

Figure 23: A bird-eye view picture of micromodel placed in the micromodel holder showing the structure of the grains and pores and the location of the channels. The ports are located in the four corners, and the pattern is repeated 36 times in the network.

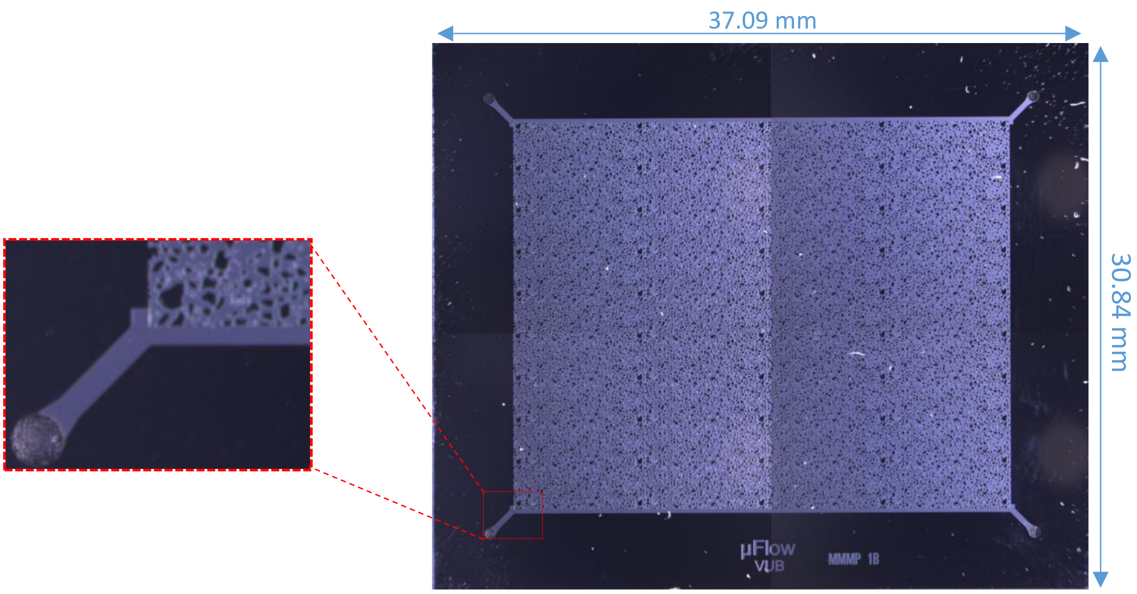

Figure 24: Picture of micromodel showing the four ports and the dimensions of the micromodel

6.2.2 Micromodel Holder

The micromodel holder have two main purposes: Connect ports to tubes for injection and production; transfer heat from the adjacent copper pipes to the pore space for temperature control to maintain constant temperature for bacterial growth or supercritical CO_2 conditions.

O-rings are placed in depressions in the micromodel holder that align with ports in the micromodel (Figure 25), and the micromodel is held in place by an aluminum plate with eight screws (Figure 26). Two 1/8 inch copper pipes pass through the micromodel holder through the pre-drilled tracks (Figure 25), and a thermal paste ensures heat exchange between the warm water circulating in the copper pipes and the pore space in the micromodel.

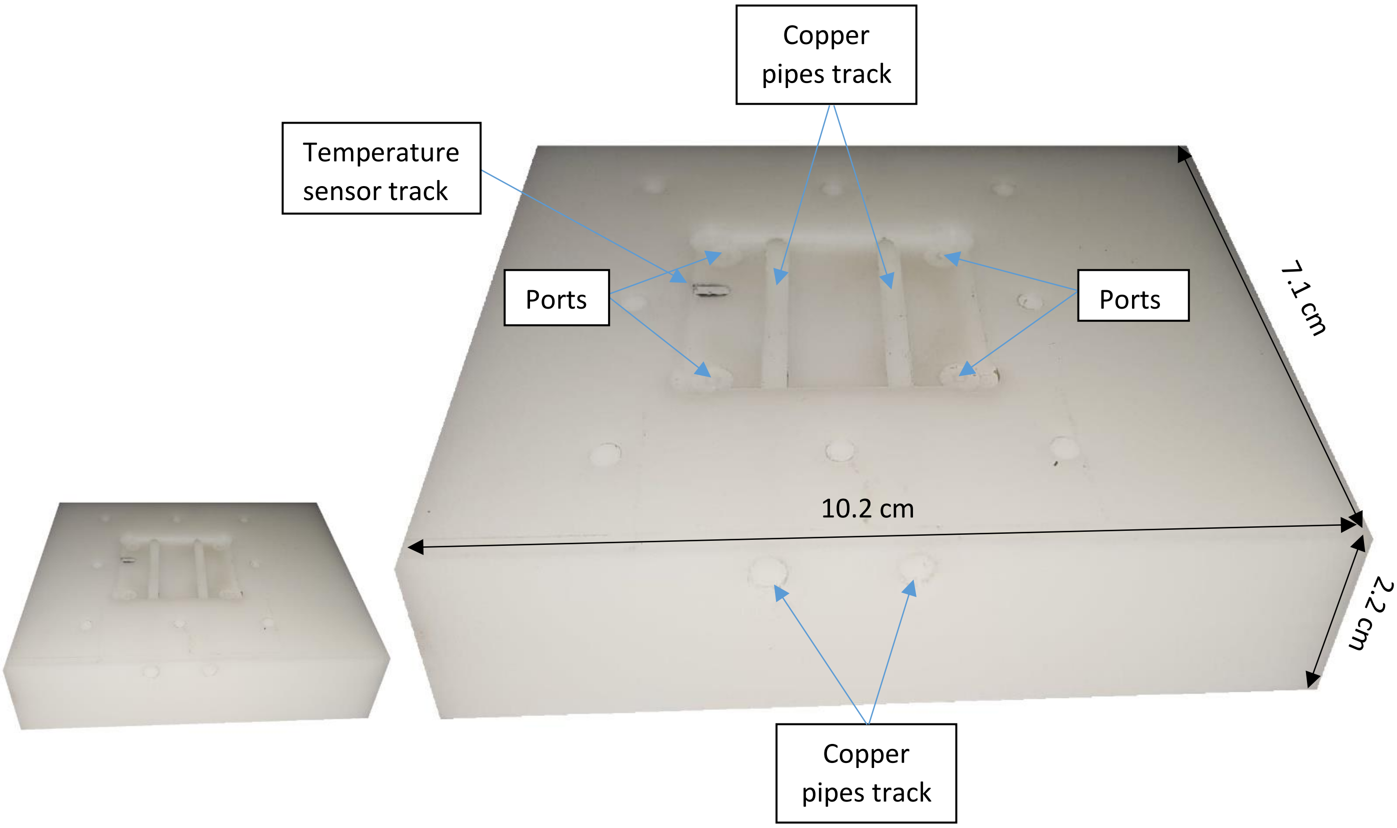

Figure 25: Top part of the polyoxymethylene (POM) micromodel holder. Showing the drilled tracks used for temperature monitoring and heat exchange, and the depressions adjacent to ports where O-rings are placed.

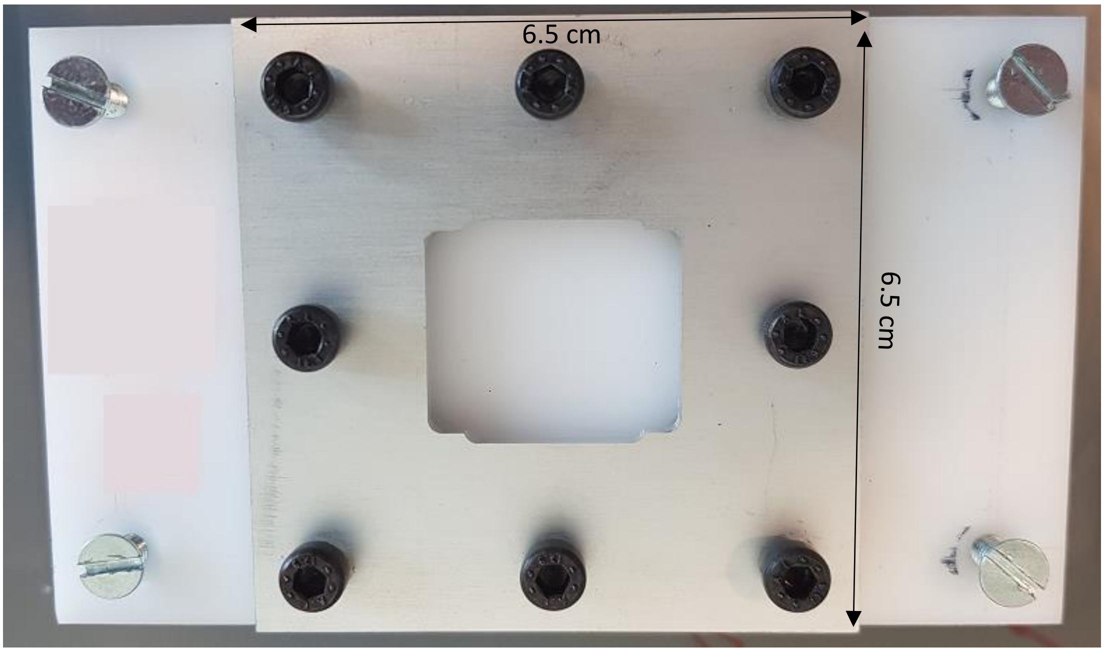

Figure 26: Aluminum plate attached to the POM micromodel holder.

6.2.3 Developing of the Micromodel Holder

The micromodel holder was originally made of POM and did not have the tracks shown in Figure 25. To get a flat surface, the tracks were drilled 3700 μm below the micromodel so that the micromodel does not break. The 1/16 inch tubes were mounted in the rails, and the top part of the tracks was flattened with thermal paste.

Small particles were observed inside the micromodel when the water injection started (Figure 27), and it was suspected to arise from the stainless steel (ss316) injection tubes connected to the micromodel. The reduced pH of the aqueous phase when saturated with CO_2 resulted in rapid rust developing in the tube that was transported into the porous medium. Polyether ether ketone (PEEK) has been found to resist all the chemicals and fluids used in this thesis, and all ss316 injection and production lines were replaced with PEEK material. The POM was also found to react with calcium chloride in the reactant solution. The material used in the holder of the micromodel was therefore changed from POM to PEEK.

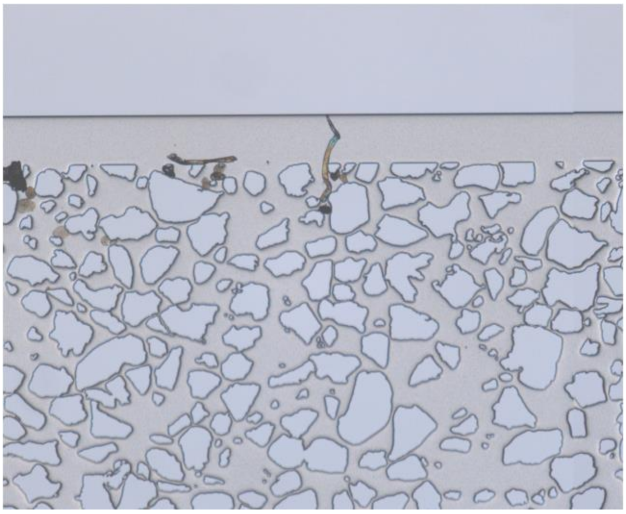

Figure 27: A bird-eye view picture of micromodel showing the particles that were observed in the micromodel.

The system was again tested after machining the micromodel holder in PEEK rather than POM, and the small particles were still found to be injected into the micromodel. It was assumed that the small particles came from the Quizix QX pump. To check this assumption, the water was injected directly from the pump to the micromodel, and the small particles were found still to be injected into the micromodel. As mentioned in the Experimental part, the pump was cleaned with toluene after initial testing, after which the number of particles observed in the pores decreased significantly. A further improvement was that the aluminum plate at the top of the micromodel was painted black to reduce reflected light (Figure 28): this enhanced the edges of images.

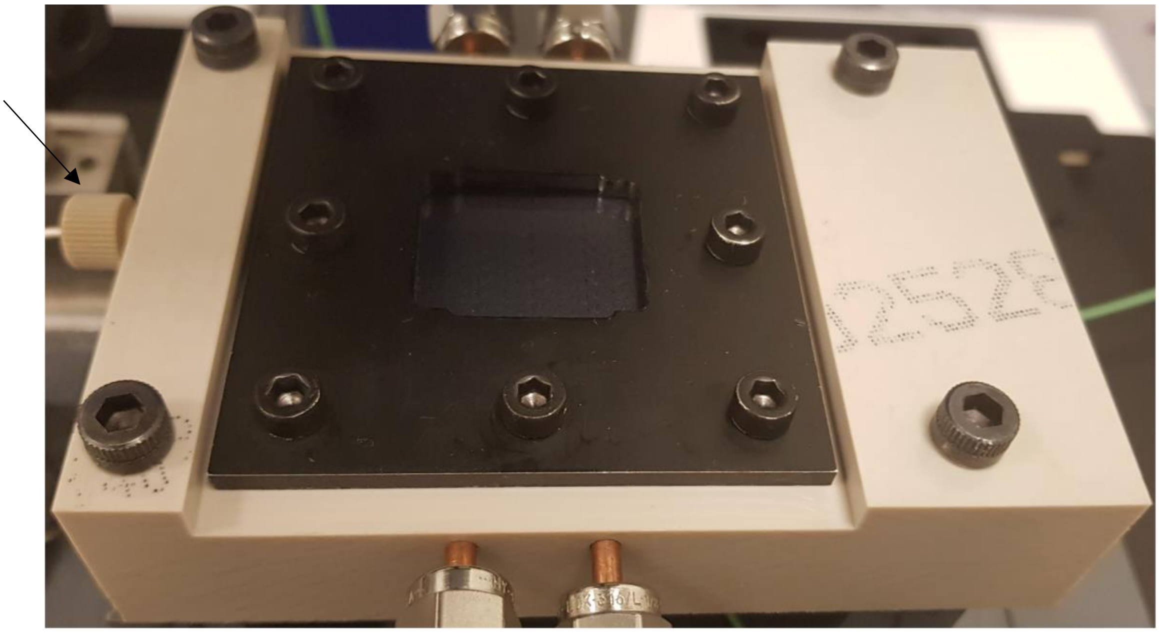

Figure 28: The PEEK micromodel holder used in this thesis. The middle of the micromodel holder has been milled to fix the temperature sensor to it, and the aluminum plate has been painted with black to remove reflection from it.

6.2.4 Heating System

A heated water bath was used to circulate warm water through the micromodel holder. The inlet peek tubing passed through the warm water hose before reaching the micromodel to heat the injected CO_2 saturated hydrochloric acid before entering the pore space. The system was isolated with insulating tape to maintain a constant temperature. The micromodel temperature was monitored using a type T thermocouple under the micromodel and an IR thermometer on the surface.

6.2.5 Differential Pressure Transmitter

The APLISENS PRE-28 SMART differential pressure has a measuring range of 0-2.5 bar differential pressure, with a static pressure limit up to 250 bar. The instrument accuracy is below 0.1 % of calibrated range.

6.2.6 Pumps

The three pumps used in this thesis are shown in Figure 29. Quizix QX pump was used to supply the micromodel with filtered, distilled water, and the Quizix SP-5200 pump was used to inject CO_2 to the micromodel through an accumulator (to saturate the hydrochloric acid). KDS Legato 100 was used to pump the bacteria and reactant directly to the micromodel to avoid bacterial contamination of the lines or sealing the lines and valves with calcite precipitation.

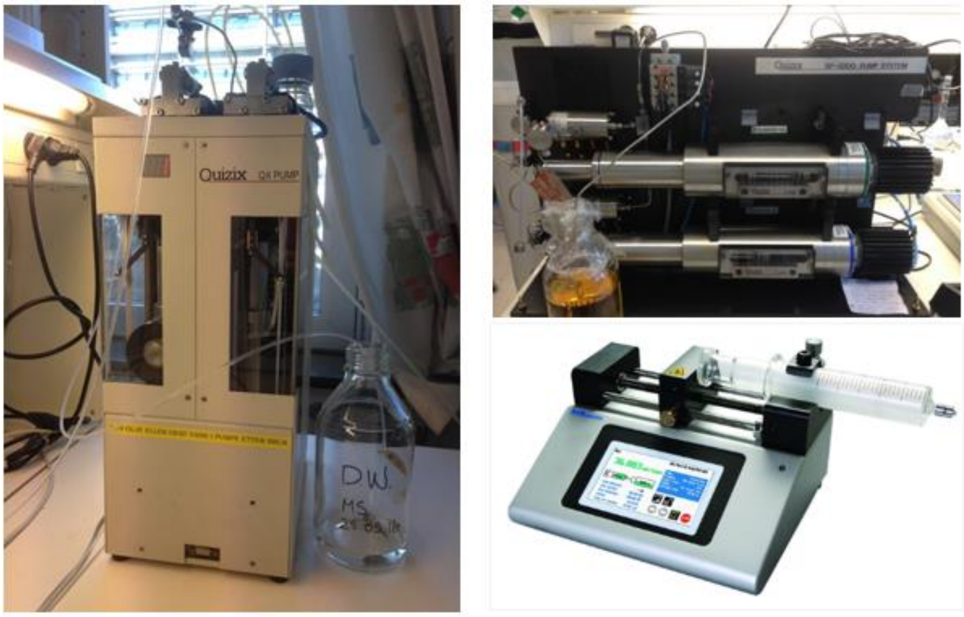

Figure 29: Pumps used in this thesis. Quizix QX pump is shown on the left side. On the upper right, Quizix sp-5200 is shown, and KDS Legato 100 syringe pump is shown under it.

Cleaning procedures of Quizix QX pump

The pump was cleaned with toluene and isopropanol. Laboratory protocols for health, safety, and environment (HSE) have been used to treat these chemicals safely. Toluene and isopropanol bottles have been opened in a fume hood to acquire the minimum needed quantity. Viton gloves and an integrated filter 3 M 4251 half mask were used. The following steps are used to clean the cylinders:

- Fill the pump with air
- Circulate 300 ml toluene using 500 ml/h rate (set the piston return rate multiplier to 1.2, to avoid pump damage)
- Circulate air for 45 min using 800 ml/h rate in the same bottle used for toluene by pulling the injection tube to the top of the bottle
- Circulate 150 ml toluene using 500 ml/h rate
- Circulate air for 25 min using 800 ml/h rate in the same bottle used for toluene by pulling the injection tube to the top of the bottle
- Inject 450 ml isopropanol using 500 ml/h rate and produce in another bottle (to remove residual toluene from the pump)
- Circulate air for 20 min using 800 ml/h rate.
- Fill 1800 ml filtered, distilled water using 500 ml/h rate and produce in another bottle.

6.2.7 Microscope

Figure 30 shows an image of the microscope used in this thesis. The main components and their properties are listed below:

- Cold-light source CL9000 LED: This light source delivers up to 900-lumen light flux at 9 mm fiber cable. The light intensity can be adjusted either from the light source or the software.
- Zeiss axiocam 305 color: is a 5 Megapixel camera for high-resolution imaging at fast speeds, it can take 36 full-frame (max 2464 × 2056 pixels) images per second.
- Stage: Zeiss stage is used so that a large area can be covered while using a high zoom to get high-resolution images.
- Zoom: The microscope body (0.7x…11.2x) and 10x eyepiece is used to get a zoom from 7x to 112x.
- Focus : To get an appropriate focus a 12 supporting points are distributed over the micromodel using the Zeiss software and the focus is set manually for each point.

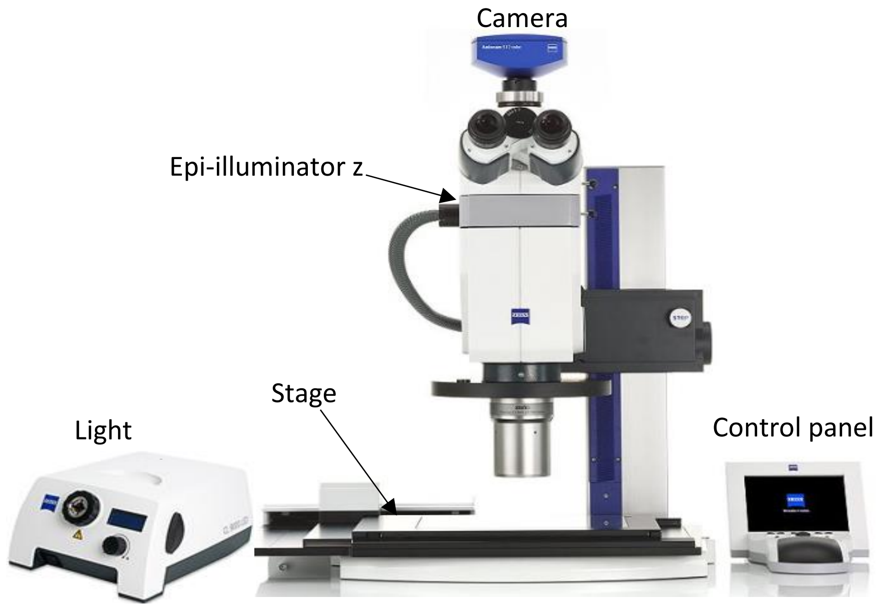

Figure 30: Image of Zeiss Axio Zoom. V16 Microscope (Zeiss)

6.3 Bacteria Handling

6.3.1 Preparation of Growth Medium and Reactant

Growth medium preparation (Song et al., 2018):

- Mix 47g of brain heart infusion into 900 ml of distilled water
- Sterilize the well-mixed solution for 15 min at 121 °C in an autoclave.
- Mix 20 g of urea into 100 ml of distilled water.
- Add the urea solution to the broth solution by using a 0.2 μm syringe filter
- The solution can be stored at 4 °C for 4 weeks.
- Filter the solution by using a 0.2 μm syringe filter before adding bacteria.

Reactant preparation (Song et al., 2018):

- Mix 1 M urea and 1 M calcium chloride dehydrate in distilled water
- Filter the solution by using a 0.2 μm filter to avoid injecting small particles to the micromodel

6.3.2 Cultivation of Bacteria

The bacteria were received in a vacuumed and sealed glass as a dried pellet. The pellet was added to 0.5 ml of the growth medium and allowed to rehydrate for 30 minutes, then 200 μl was moved to a 5 ml growth medium centrifuge tube. The centrifuge tube was placed in a heating cabinet at 30 °C for 24 hours, then after 24 hours the growth was detected by turbidity. This procedure was repeated one more time by adding the same amount of bacteria (0.2 ml) to a 10 ml growth medium and preserved in heating cabinet at 30 °C for 24 hours, and the growth was observed after 24 hours by turbidity. Then 200 μl of the bacteria solution and 200 μl of 30 % glycerol were added to 6 pendlorf microtubes for long-term storage at -80°C. The inventory of glycerol was prepared in case bacteria die or get concurred by other bacteria. The bacteria were moved every 7 days to a new 10 ml growth medium to prevent the death of bacteria as Figure 31 shows.

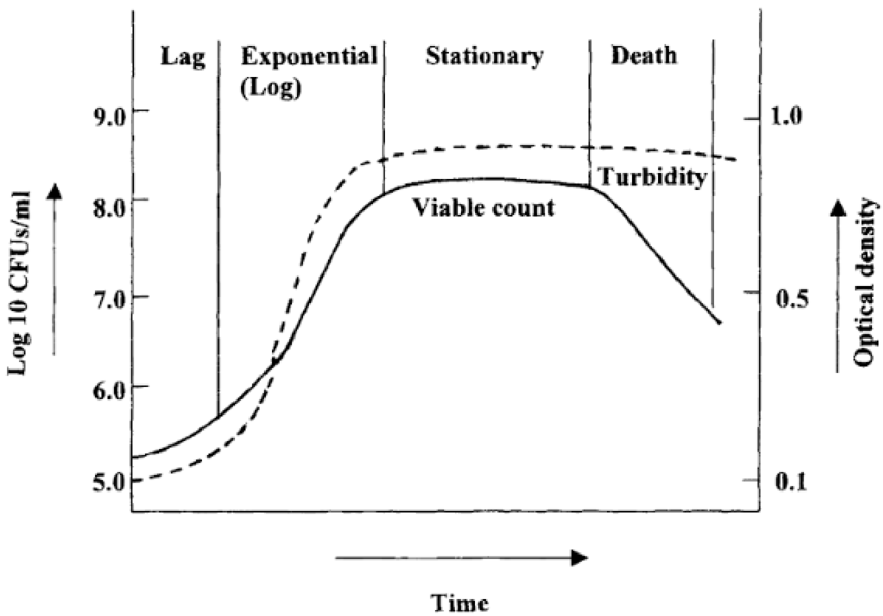

Figure 31: Curve of the bacterial growth. After the lag phase, the bacteria starts to grow exponentially by dividing the cells, and in the end, nutrients become less available, and the cells start to die and decay exponentially (Srivastava, 2003).

6.3.3 Activation of the Bacteria in the Micromodel

Initially, the micromodel was saturated with filtered, distilled water at ambient conditions. Then 5 μl bacteria were injected with 5.7 $\mu l/min$ rate with the syringe pump. The bacteria are dense and will be unevenly distributed if the injection takes too long, therefore the rate has to be high enough to avoid bacteria settling towards the bottom of growth medium. Then 471 μl growth medium was injected (466 μl upstream of injection point dead volume of tubing and the valve and 5 μl more to ensure that the bacteria will be at the center of the micromodel). The bacteria were then kept at static conditions in the micromodel for 5 hours so that it can grow and adhere to the grains to encourage calcite growth at the grains, not in the pores, and growth medium was continually injected with 10 $\mu l/min$ rate through the top channel to remove the bacteria from the channel.

The reactant solution was injected with 5.7 $\mu l/min$ at ambient condition after bacteria growth. In-situ precipitation of calcite crystals was monitored with the microscope. The micromodel was fully saturated with the reactant because calcite will only grow where bacteria meet the reactant.

7. Image Analysis

This chapter describes the essential image analysis tools created during this master thesis. The scripts can be found in the Appendix.

7.1 Test Grounds

An image of the entire micromodel using 50X zoom has approximately 24 000 x 19 000 pixels (900 megabytes (Mb)), and script evaluation on images of this size was very time-consuming. Hence, smaller subsections were defined (Figure 32) to evaluate and test image analysis tools efficiency before scripts were applied to images of the entire model.

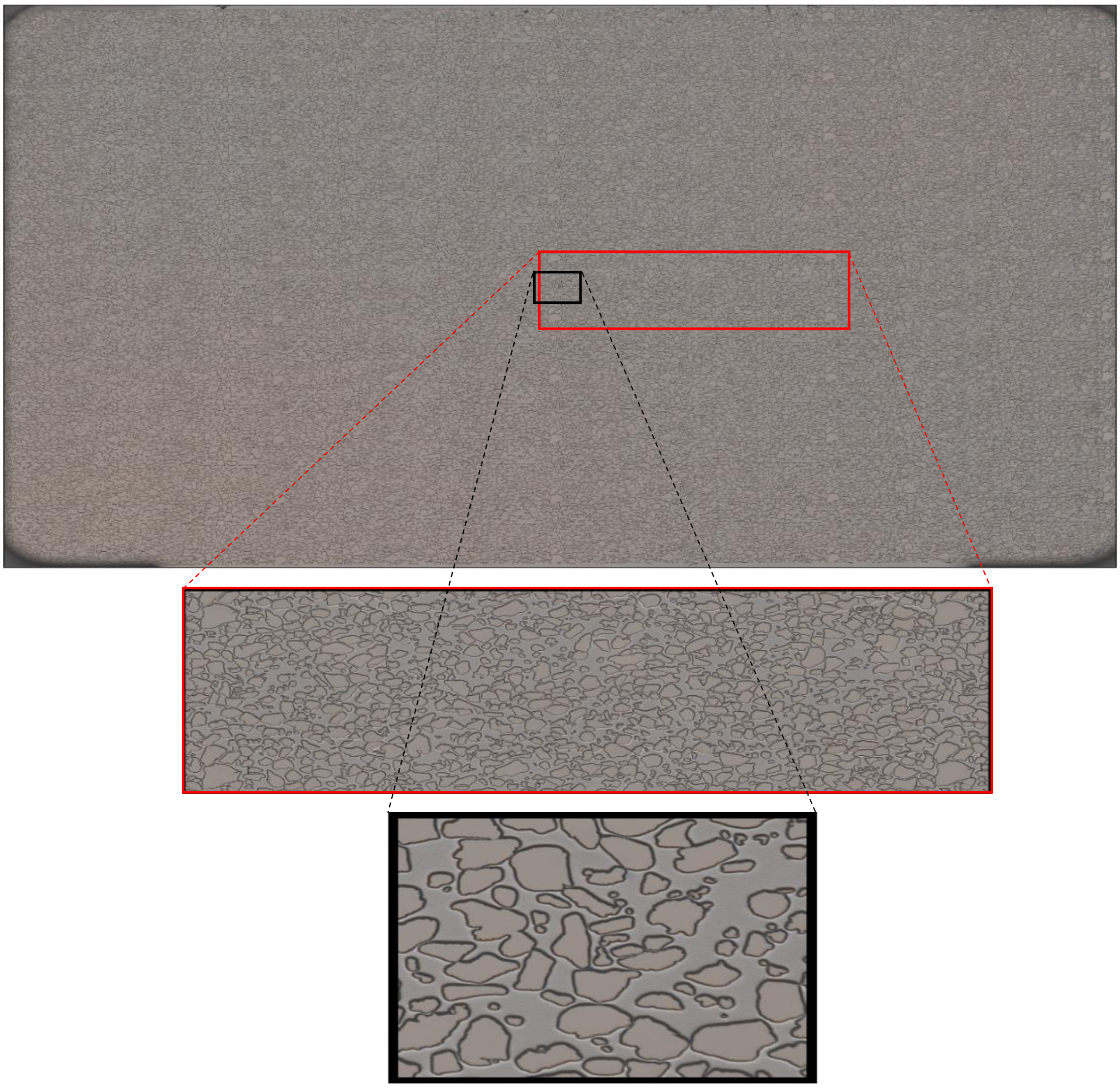

Figure 32: A bird-eye view picture of micromodel inside the micromodel holder showing the different scales that have been used to test the scripts. The picture in the top shows the whole micromodel, it has been used to check the effectiveness of the scripts after the scripts worked successfully on the two other scales. Test ground 1 is shown in the bottom, and it represents 0.23% of the whole model, the scripts usually takes just seconds to get results from this scale. Test ground 1 has been selected randomly, it doesn't represent all the structure in the whole micromodel. Test ground 2 is shown in the middle, it has been selected so that it can be representative of the whole micromodel. The micromodel is repetitive 36 times, and test ground 2 is one of these 36 repetitions.

Subsection *Test ground 1* (1050 x 1050 pixels, 1.6 Mb) enabled quicker image import in the computer for script evaluation compared to full-model images. With access to all the grains it was easier to identify individual grains in *Test ground 1* to develop scripts because code debugging was quick. The main reason for checking the scripts on *Test ground 1* rather than the full-model images was the script running time: seconds (*Test ground 1*) compared with days (full-model image). Subsection *Test ground 2* (6650 x 2650 pixels, 27.7 Mb) was more representative of the full-model images compared with *Test ground 1,* with all grain sizes and shapes included. Each full-model image consists of 36 repetitions of *Test ground 2*; hence, scripts running successfully on *Test ground 2* will also perform well on full-model images. After the scripts performed well on *Test ground 1*, it was checked on *Test ground 2* to verify that the parameters selected worked for all the grains in the micromodel. Finally, scripts were applied to full-model images to check efficient performance with more than 30 000 grains (with cross-checking) with an exponential increase in run time. Each script contains different image analysis tools that each perform a specific operation (detailed below), and the run time of each tool was quantified to identify the need to improve the code to make the total script run time as low as possible.

Figure 33 and Figure 34 show a comparison of the three image sizes to justify the use of them. *Test ground 1* was found to be representative for grain sizes less than $25\times 10^3\ \mathrm{\mu m}^2$, but not for larger sizes, whereas *Test ground 2* was found to be representative for the full-model images because it has all the grain sizes to be found in the full-model images. In addition pore throats lengths were also used to evaluate the three images sizes. Pore throats in *Test ground 2* was found to be representative for all the pore throats in full-model, whereas *Test ground 1* was found to be missing pore throats longer than 312.5 μm. Based on the evaluation of the grain sizes and pore throats for the three image sizes the scripts could be evaluated in *Test ground 1* and *Test ground 2*, and enormous time was saved.

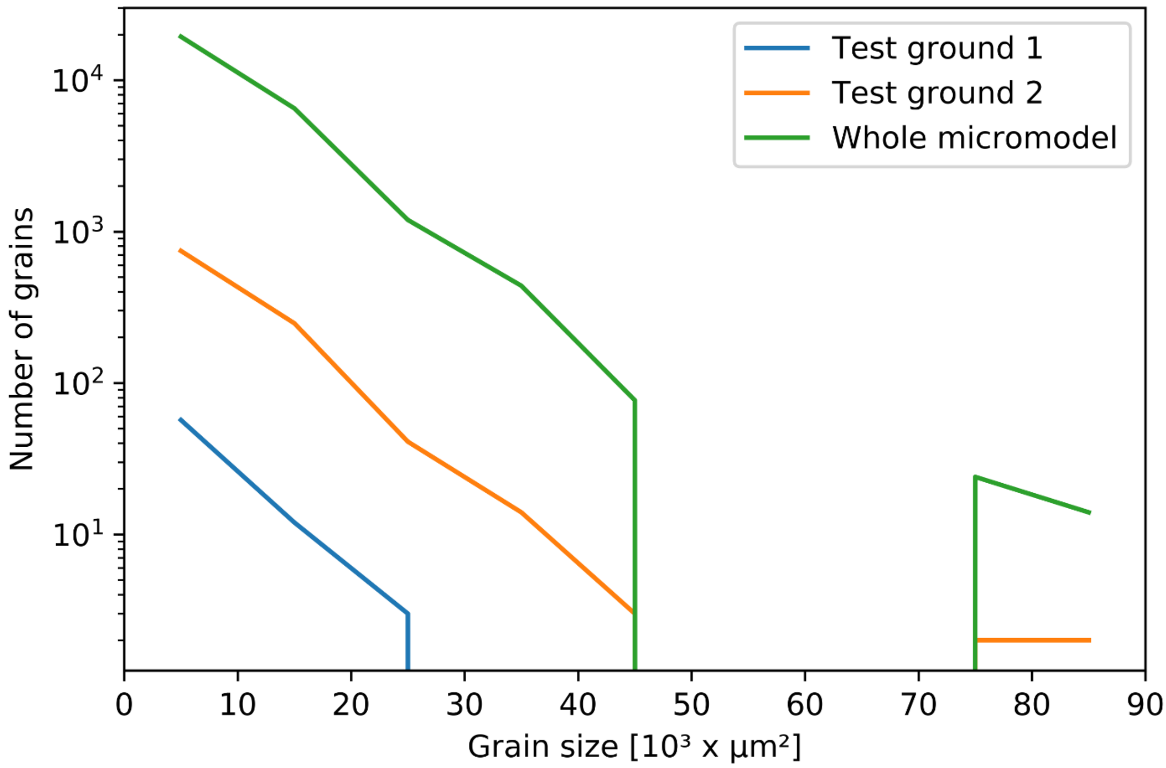

Figure 33: Number of grains versus grain size for the three image sizes (Test ground 1, Test ground 2 and Whole micromodel) used to develop scripts. Test ground 1 is representative for grain sizes less than $25\times 10^3\ \mu m^2$, but it is not representative for larger grain sizes. Test ground 2 is representative of the whole micromodel as it has the same grain size as the whole micromodel.

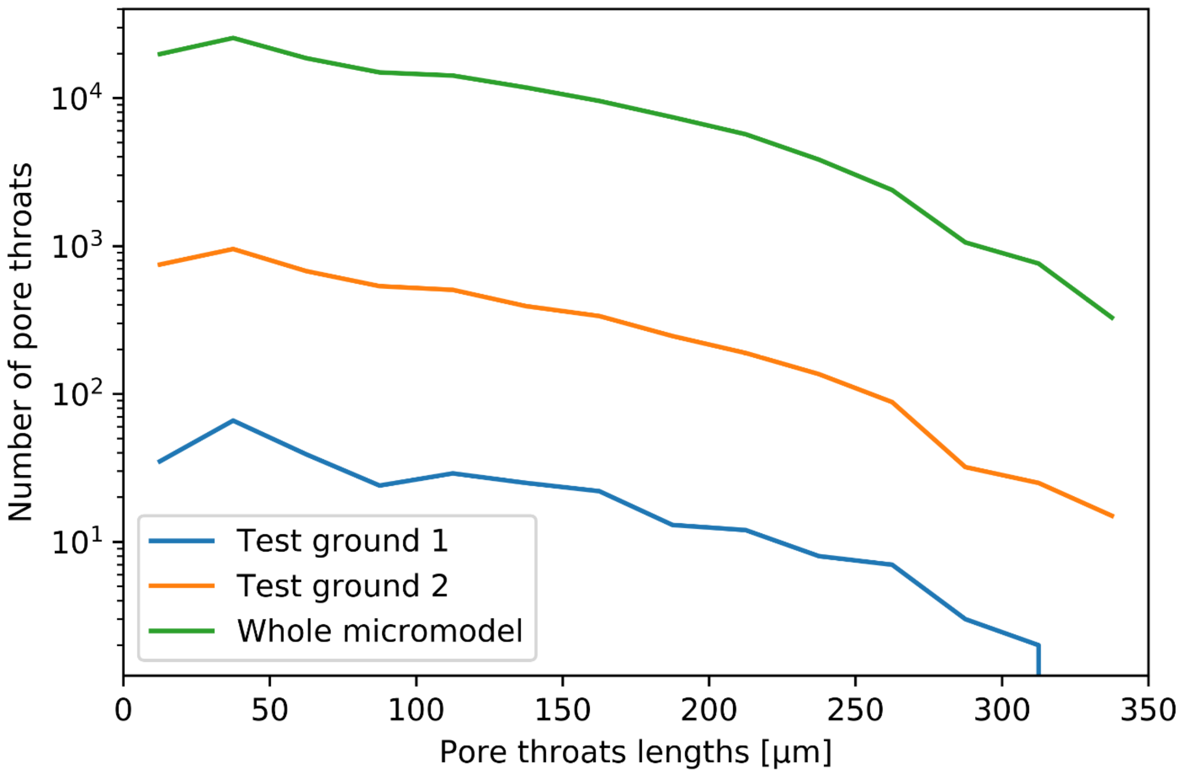

Figure 34: Number of pore throats versus pore throats lengths for the three grounds used for scripts development. As the previous figure test ground 2 is representative of the whole micromodel, while test ground 1 missing pore throats longer than 312.5 μm.

7.2 Thresholding

Thresholding is the most critical part of the image analysis performed in this thesis: with correctly implemented thresholding, advanced image analysis may be performed efficiently. Initially, an epi-illuminator z (Figure 30) was used that targets the center of the field of view and then spreads light circularly, so the light intensity in the edges differs from the center. To achieve the same intensity in the entire image to enable efficient and good thresholding, a shading correction can be applied in the microscope software. The images were transferred to grayscale, filtered with the function *frangi*, then thresholded with the function *threshold_mean (*Figure 35*)*. These functions can be found in the *skimage* library in *python*.

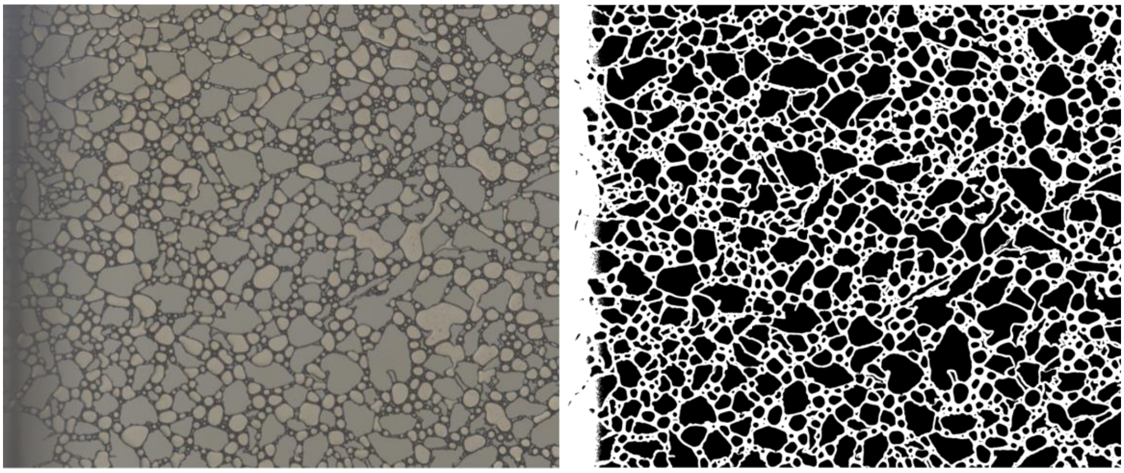

Figure 35: (left) Original image and (right) thresholded image. The image is thresholded by the functions described above.

The function described above provides a good threshold for images acquired with the epi-illuminator z, but it does not differentiate between grains and bubbles. To solve this crucial weakness and to be able to apply scripts for foam bubble quantification, a micromodel image saturated with filtered, distilled water was thresholded using the same function, but some of the narrow pores were also recognized as grains (will not occur when the pore space is fully saturated with bubbles). Using *paint.net* software, the image has been enhanced by making the pore space continuous. Using *findContours* function in *opencv* library in *python*, the grains were obtained from the image, then drawn in the top of the images. The contours did not fit well on the entire image, as each picture can shift a little in four directions due to the stage position. A picture of the entire model consists of 121 small pictures stitched together, so many contours had to be moved in each image. The image was divided into 73 parts, and contours in each of these parts had to be moved. This technique requires a lot of manual work, and was time-consuming and prone to biased interpretation, therefore a new illuminator, named fiber optic diffuser S has been tested (Figure 36).

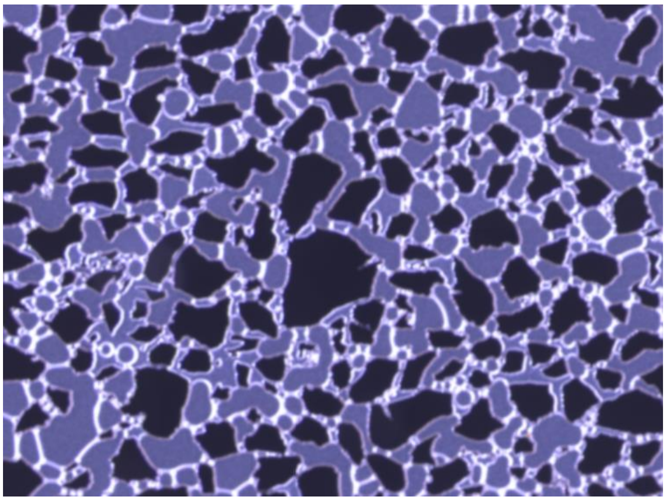

Figure 36: Image of a bubble saturated part of the micromodel using the fiber optic diffuser S.

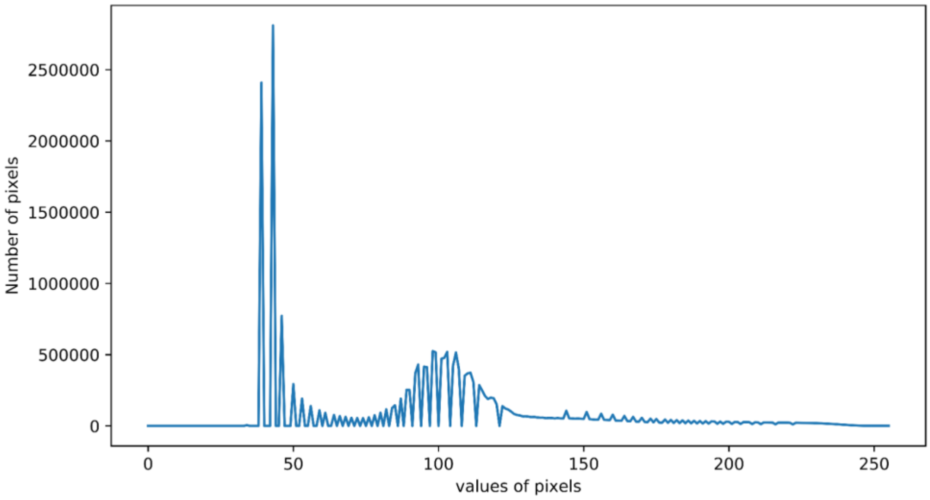

Figure 37: Number of pixels versus pixels values for a bubble saturated grayscale image. Grains have black color in pictures, thus values from 0 to 70 are grains, while lamellae and grains edges have a white color as shown in the figure above, thus values from 125 to 255 are lamellae and edges.

The thresholding of images taken with the fiber optic diffuser S was uncomplicated (due to the clear difference in colors between grains and lamellae and grain edges) than images taken with epi-illuminator z. Figure 37 indicates the values to be used to threshold images and the possibility of differentiating between grains and bubbles and draw each in an empty image (an image with the same pixels values, either 0 (black) or 255 (white)). Threshold function with parameters 70, 255, and *THRESH_BINARY* was used to threshold the grains, then a white frame was drawn around the threshed image to close all the grains in the edge of the image, so that the *findContours function could find and store all the grains as contours*. Threshold function with parameters 125, 255, and *THRESH_BINARY_INV* was used to threshold the lamellae and grain edges, then they were drawn on an empty white image with black. To ensure fully separation of the bubbles, the grains contours were drawn with black color on the same image (Figure 38). All the functions mentioned in this paragraph can be found in the *OpenCV* library in *python*. This function is defined in Appendix, Script, line 36.

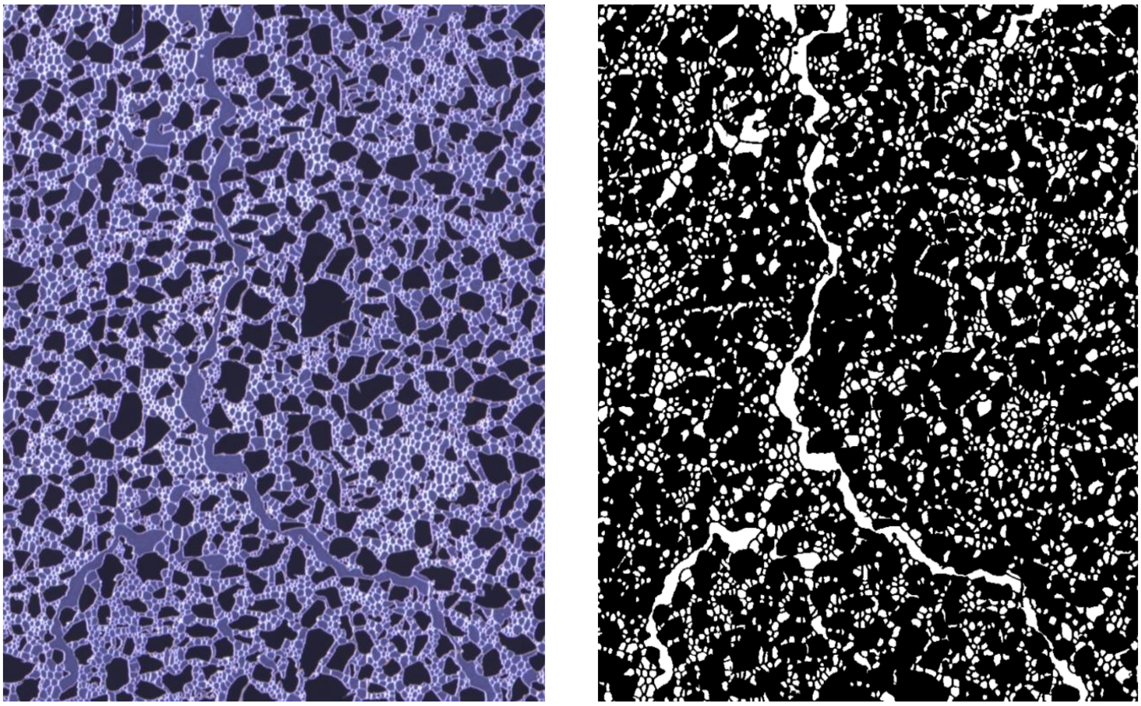

Figure 38: Original image on the left and thresholding of bubbles on the right. The function provides a good threshold for the image, and manages to separate the bubbles from the grains accurate.

7.3 Pore Throat Analysis

To study the interaction between bubble shape, orientation and distribution with local pore throat information, it is necessary to locate the pore throats. The pore throats can be obtained by finding the minimum distance between the grains. The *nearest_points* function in *shapely.ops* was used to obtain the pore throats (Figure 40). Before using *shapely* functions in *python* the contours were converted to polygons by using the *Polygons* function in *shapely.* The *shapely* function has a different coordinate system than the libraries used earlier (Figure 39), so all the y coordinates in the contours were modified to find the correct pore throats.

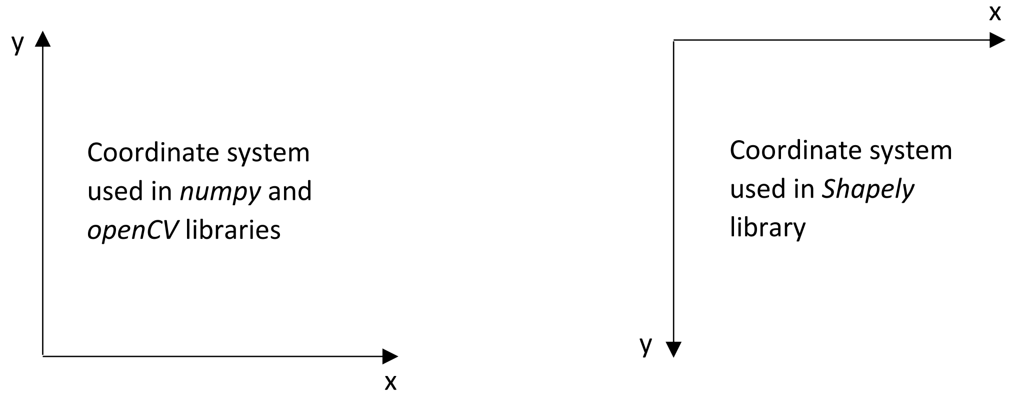

Figure 39: Illustration of various coordinate systems used in python.

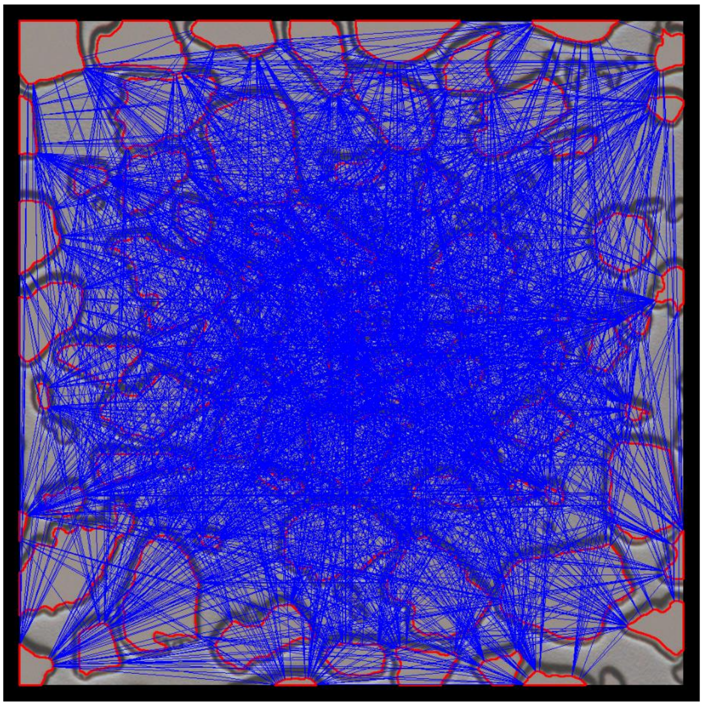

Figure 40: Result image using the method described above shown in Test ground 1. The minimum distances between all the grains were obtained, but the aim of this tool was to find the nearest points among the neighboring grains not among all the grains.

Two approaches were evaluated to identify the nearest points between the opposing grains. The first approach was to consider only connection lines that have a length less than a value (the values tested were 50, 150, 200, and 300 pixels). This approach did not perform well because some essential pore throats were missing (longer than the used value), and some connection lines were crossing other grains (when the grains were adjacent to each other), and these connection lines are not pore throats. The second approach was to use a condition to prevent connection lines from crossing the grains. This approach was achieved by using the *touches* and *intersects* functions in the *shapely* library (Figure 41). This function is defined in Appendix, Script , line 91.

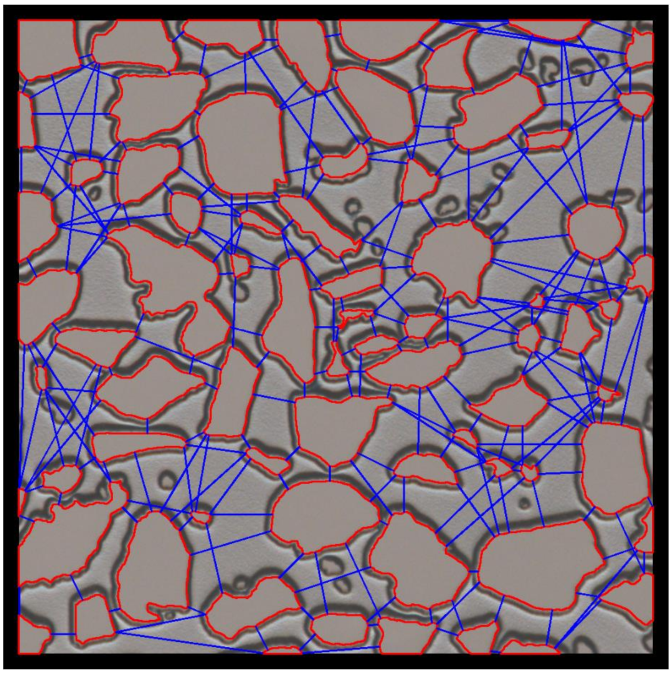

Figure 41: Result image using the method described above shown in Test ground 1. For simplicity, small grains were filtered out, but were used in experiments analyzing. The script performed well, but there were also some pore lengths, which will complicate bubble analysis described in Chapter 7.5.

7.4 Pore Throat Classification

To facilitate the bubble analysis (described in detail in the next sub-chapter), the connection lines described in the previous sub-chapter were classified into different groups. The first step was to find the pore throats: the connection lines that do not intersect other connection lines. The residual connection lines were then sorted by length to differentiate between pore lengths, and pore radii. Starting from the longest connection line, the intersection lines for each connection line were found by the *intersection* function in *shapely*, and the shortest one was classified as pore radius, whereas the connection line was classified as pore length. This procedure was conducted for all the connection lines, and the ones that had no intersection lines were added to the pore throat classification. The connection lines were successfully categorized in three different groups (Figure 42): the pore throat and the pore radius categorizes were used further in the bubble analysis part, whereas the pore length category was not used further. The pore length category may be of interest to use in another analysis tool in future research. This function is defined in Appendix, Script , line 227.

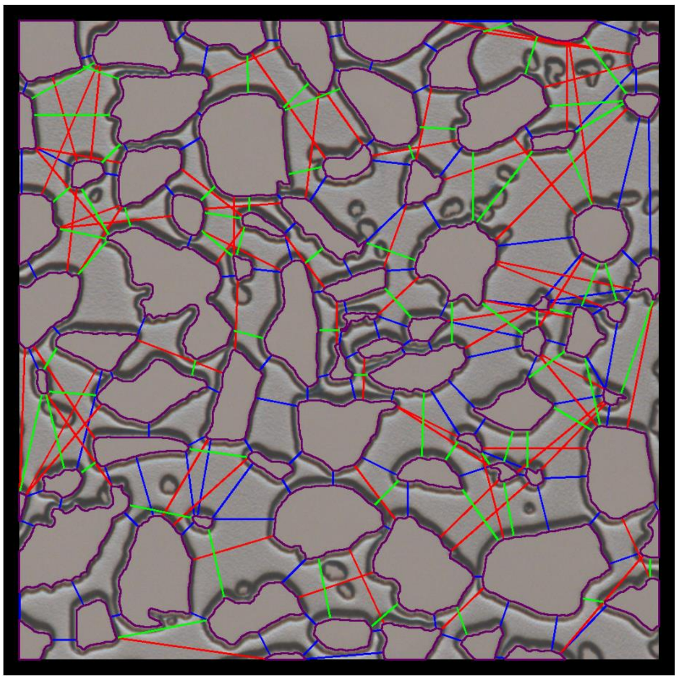

Figure 42: Result image using the method described above shown in test ground 1. The three classifications are shown in different colors. The blue lines are pore throat, green lines are pore radius, and red lines are pore length.

7.5 Bubble Analysis

The aim of this analyzing tool was to describe each bubble by the surrounding pore throats and grains. The first approach evaluated was to locate the grains surrounding the bubble, then locate the pore throats connecting the grains together. Initially, the bubbles to analyze were drawn manually by using *paint.net* software to test simple, and different scenarios. To find the bubbles using the epi-illuminator z described in the thresholding sub-chapter, two images was used: the first one contained only the grains, whereas the second one contained the grains and the manually drawn bubbles. The *centroid* function in *shapely* library was used to find the centroids of the grains and bubbles, then it was possible to subtract the centroids of the grains and bubbles in second image from the grain centroids in the first image, and the differences were the bubbles centroids. The bubbles were already separated from the grains using the fiber optic diffuser S. To locate the surrounding grains, connection lines between the bubble and the grains were not allow to intersect or touch the grains and/or the pore throats and pore radii more than once in total. In addition two more conditions had to be used to get the correct results. The first one was that the pore throats and/or pore radii intersecting the bubbles were removed to avoid intersection of the connection lines because connection lines will be removed if they intersect or touch more than one object. The second one was that the intersections of pore radii that were 10 pixels from the bubble will not be considered as intersections, and this was done to obtain data on essential pore throats and radii. The final result of this tool is shown in Figure 43.

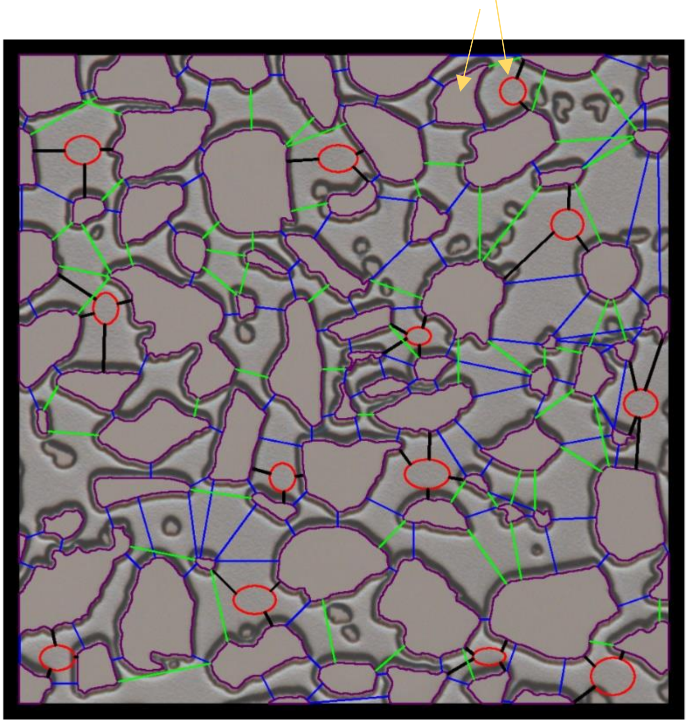

Figure 43: Image showing the outcome of the method described above. Red circles are the manually drawn bubbles, and the black lines show the grains that were considered by the script. The script worked well, but there were occasions where the script did not work well, one of these instances is shown with the yellow arrows, the third grain was not considered because the black line intersects both the grain and the green line. The main problem with this method occurs when a bubble has more than 3 grains, then the wrong pore throats and radiuses will also be considered. The method was also slow since many conditions were used.

It was time-consuming to verify the lines between one bubble and all the grains, and actually, only the neighboring grains that should be verified. A bounding box was therefore used to test only grains with centers inside the box boundary (Figure 44). This technique significantly reduced the script running time on the full-model images.

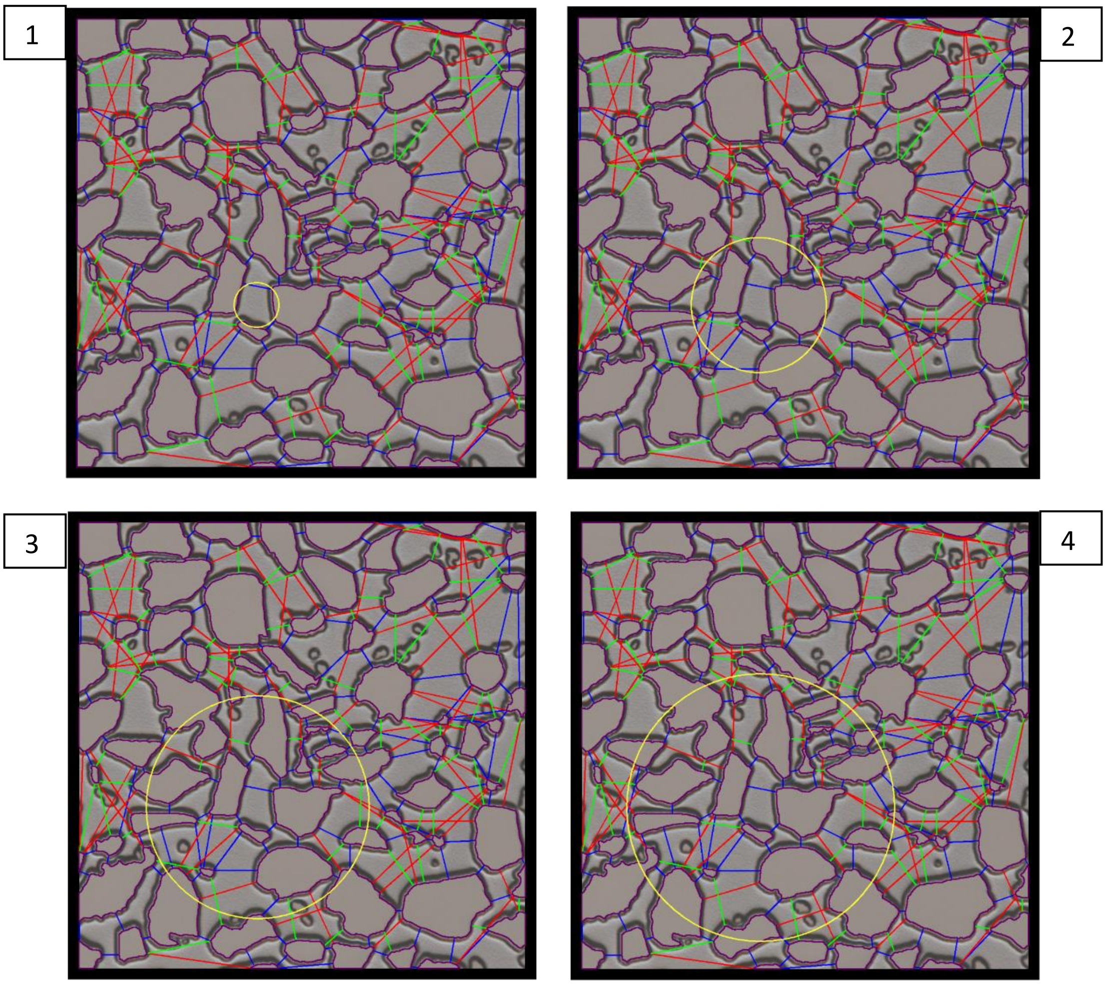

Figure 44: Images illustrating the size of the box to be used to include all the adjacent grains. The center of the yellow circles is the same as for the bubble and radii varies. (1) radius = 55 µm, (2) radius = 164 µm, (3) radius = 274 µm, and (4) radius = 329 µm. Radius = 274 µm was selected because image (1) and image (2) do not include all the adjacent grains centers, and there are too many grains in image (4).

The previous method described did not perform well for all the scenarios (Figure 43), therefore a new method was verified. The next method was to draw the grains and the lines that do not intersect the bubbles on an empty white image with a gray frame and use the *floodFill* function in the *OpenCV* library. The frame was used to stop the *floodFill* if the bubbles were located in the edges of the image (Figure 45). Then the image was thresholded to obtain the filled area (Figure 46). After converting the black filled areas to polygons, the intersection lines and grains with this polygons can be located as described in the previous analysis tools (Figure 47):

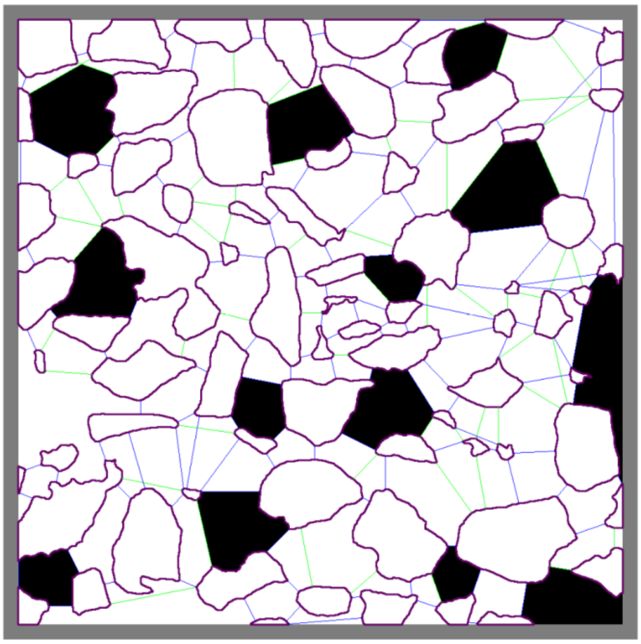

Figure 45: Image showing the result of the method described above . From the middle of the bubble, the filling function begins filling with black and stops if the color is different (grains, blue and green lines, and the gray frame).

Figure 46: Image showing the threshold of the previews image using the described threshold function. These shapes were then converted to contours and then polygons, so it is possible to find the intersection between them and the lines.

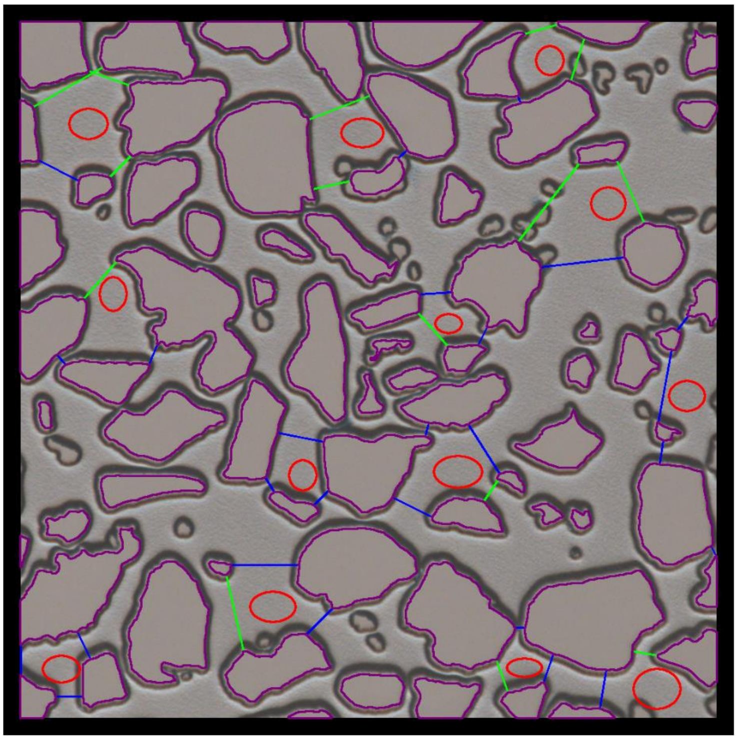

Figure 47: The final result shows the bubbles in red, the pore throats and radiuses that were considered, and the grains. This method also works well for large bubbles and channels.

In a realistic foam image, the bubbles are close to each other, and the method described above will not work unless each bubble is considered alone. The size of bubbles varies greatly, therefore the bounding box size was set as a function of the bubble area so that it fits all bubbles well. For each bubble, only the grains and lines that were located in the box that were drawn to improve runtime of the script, and the pore throats intersecting the bubble was drawn with white color to avoid stop of the *floodFill* function. This bubble analysis tool is defined in Appendix, Script, line 343.

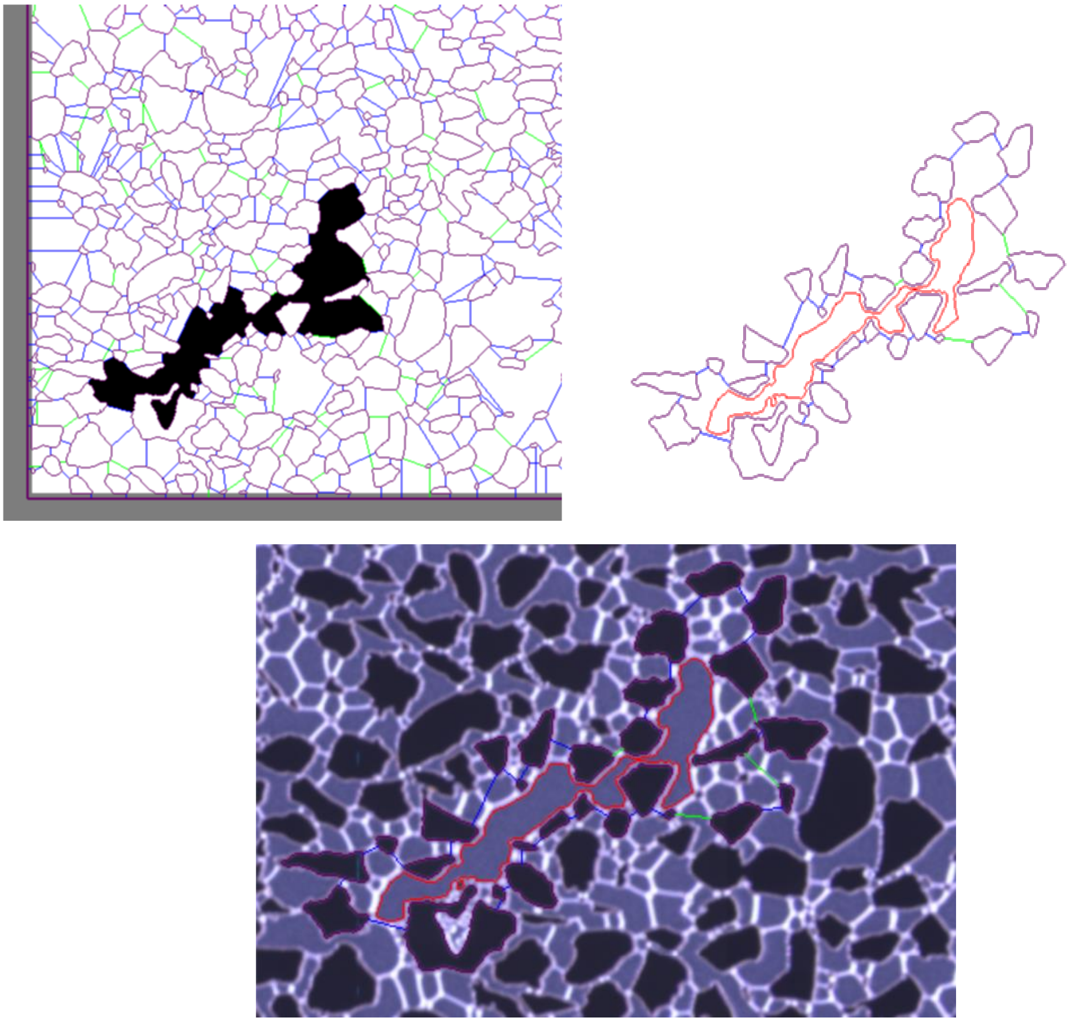

Figure 48: These images show the steps used to identify the lines and grains in a realistic image. The first step was to remove all the lines that intersect the bubble and then fill with black color (image at the top left). The second step was to find the black shape intersecting lines and grains (image at top right). In the bottom, the bubble and the lines are drawn on the original picture. The script succeeded in identifying all the pore throats surrounding the bubble. A contour around the image is shown in the top left image in the same color as the grains. This contour was added so that lines can be drawn from the grains to the edges of the image so that when the bubble is located in the edges, the fill function can be stopped.

Part III: Results and Discussion

8. Experimental Overview and Uncertainty

8.1 Experimental Overview

This section presents the foam pore-scale experiments conducted in this thesis to investigate the combined and separated use of nanoparticles and surfactants as foaming agents. Foam generation and stability using surfactants and nanoparticles dispersed in brine were studied by quantifying number of bubbles in the pore space during CO_2 injection. A total of 13 experiments were conducted in the same micromodel at 100 bar and room-temperature.

The Zeiss microscope software produce a czi image of the whole pore space amounting to 4.38 gigabytes (Gb) when 1x1 binning is applied. With one image captured every 72 second, each injection produced approximately 1.8 Terabytes (Tb) of image data. The large image size made export to png format and further image analysis inefficient, and a resize technique was tested, where 16 pixels were reduced to one pixel (25% resize). The resized png images (60 Mb) performed well in the scripts described above, and applied for experiment images acquired with 1x1 binning (Table 1). Further image size reduction, to be able to analyze more experiments, was also evaluated using 2x2 binning and 50% resize (16 pixels to one pixel) during png formatting. This resulted in reducing the total image data for each injection from 1.8 Tb to approximately 300 Gb; hence more experiments could be conducted. This techniques reduced runtime of scripts even further and were applied in most cases (Table 1). The conversion value used after binning and resizing is 4.380 μm/pixel.

Table 1: The injection fluids and rates used, and binning and resize techniques used.

Fluid	*Composition*	*Injection rate* $[\mu l/min]$	*Binning*	*Resize*
AQ1	0.5 wt% surf	1	1x1	25%
AQ2	0.5 wt% surf	4	2x2	50%
AQ3	0.05 wt% surf	4	1x1	25%
AQ4	0.5 wt% surf + 0.15 wt% NP	4	1x1	25%
AQ5	0.5 wt% surf + 0.015 wt% NP	4	2x2	50%
AQ6	0.15 wt% NP	4	2x2	50%
BL1	3.5 wt% NaCl	4	2x2	50%
AQ7	0.5 wt% surf	4	2x2	50%
AQ8	0.05 wt% surf	4	2x2	50%
AQ9	0.5 wt% surf + 0.15 wt% NP	4	2x2	50%
AQ10	0.5 wt% surf + 0.015 wt% NP	4	2x2	50%
AQ11	0.15 wt% NP	4	2x2	50%
BL2	3.5 wt% NaCl	4	2x2	50%

8.2 Uncertainty

This section will give an overview of the uncertainties in the experiments performed in this thesis and their possible influence on the result. The porosity and permeability uncertainties were calculated by the standard deviation formula.

$$S = \sqrt{\frac{\sum_{i=1}^{n}(x_i - \bar{x})^2}{n-1}} \tag{17}$$

where $\bar{\bar{x}}$ is the mean of all values in the data set, x_i is each value in the data set, and n is the number of values in the data set.

The image analysis calculation used in this thesis were based on the threshold images, and incorrectly thresholded images translate to incorrect results. Therefore the main uncertainty of the image analysis calculations described above was determined to be the thresholding part. As described in Part 2, the thresholding method uses lamellae and grain edges to separate bubbles; therefore when the image is not fully saturated with bubbles some pores will be interpreted as bubbles. Hence, the accuracy of this thresholding method increases with increasing bubble saturation of the pore space, and the uncertainty is high during the foam generation period when the pore space is only partially filled with bubbles. In order to get a better estimation of the foam generation period, a *Hierarchy* method in *OpenCV* was applied. This method is displayed in Appendix, Script, line 82. This method considers only the outermost contours at the same level (Figure 49), so if a bubble is enclosed by another bubble, it will be removed. This method gives a more accurate result in the foam generation period, but the accuracy of the periods after foam generation becomes somewhat reduced (Figure 50).

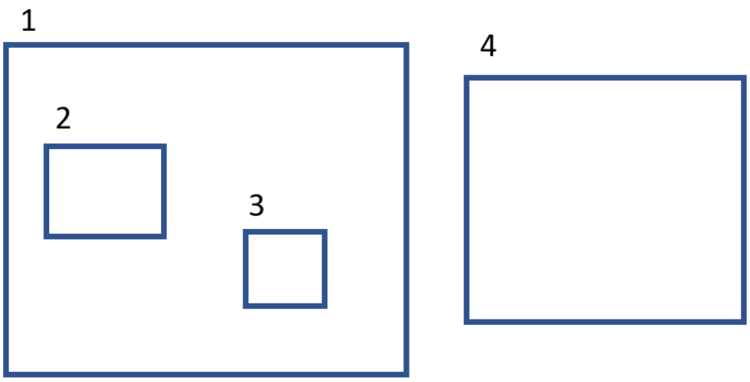

Figure 49: Illustration of the Hierachy method. Objects 1 and 4 are outermost and they are in the same level, whereas objects 2 and 3 are innermost and are in different level compared to 1 and 4.

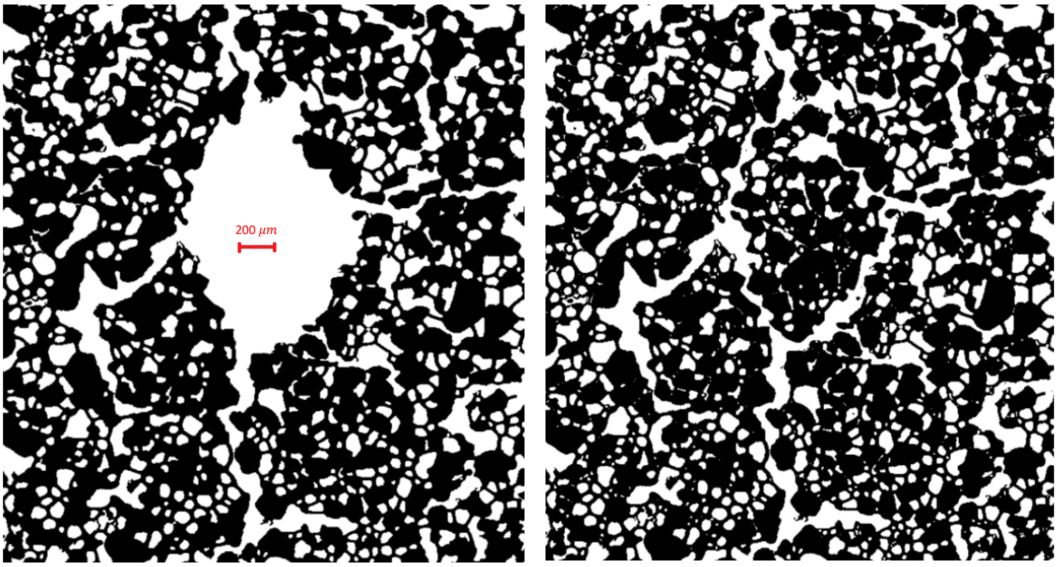

Figure 50: The segmentation images using the hierarchy method (left) and not using it (right). In case that a bubble encloses other bubbles, the enclosed bubbles will be removed.

A small area in the pore-space (Figure 51) was selected randomly to test the uncertainty of the segmentation method. The number of bubbles with and without the hierarchy method were compared, and the uncertainty for each image was quantified: using images filled with bubbles the bubble number with hierarchical approach was subtracted from the regular bubble number (without using the hierarchy method), then divided by the hierarchical bubble number. With this approach mean uncertainty was quantified to be 0.5%.

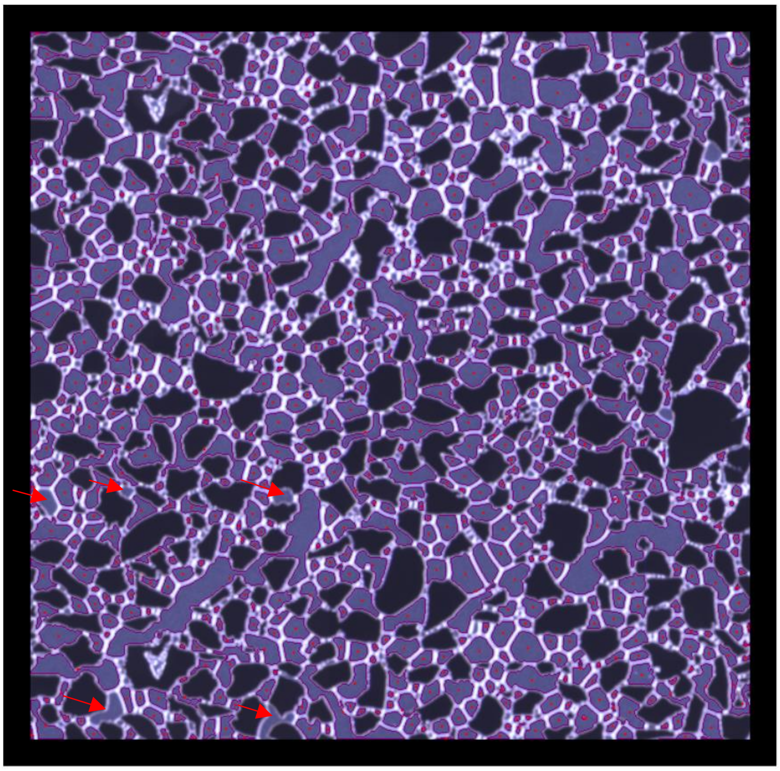

Figure 51: illustration of the bubbles that are considered (purple) using the hierarchy method. The bubble centroids are shown with red points. The red arrows show the bubbles missing.

9. Porosity and Permeability

Porosity was calculated as described in Part 1 and evaluated for an increasing portion of the pore space 100 times (between 0.11 % and 96% of the entire micromodel, Table 7). The contours used to quantify the porosity matched the grains well (Figure 52), indicating a good approach to the micromodel porosity. The porosity is calculated to be 0.607 $\pm$ 0.001.

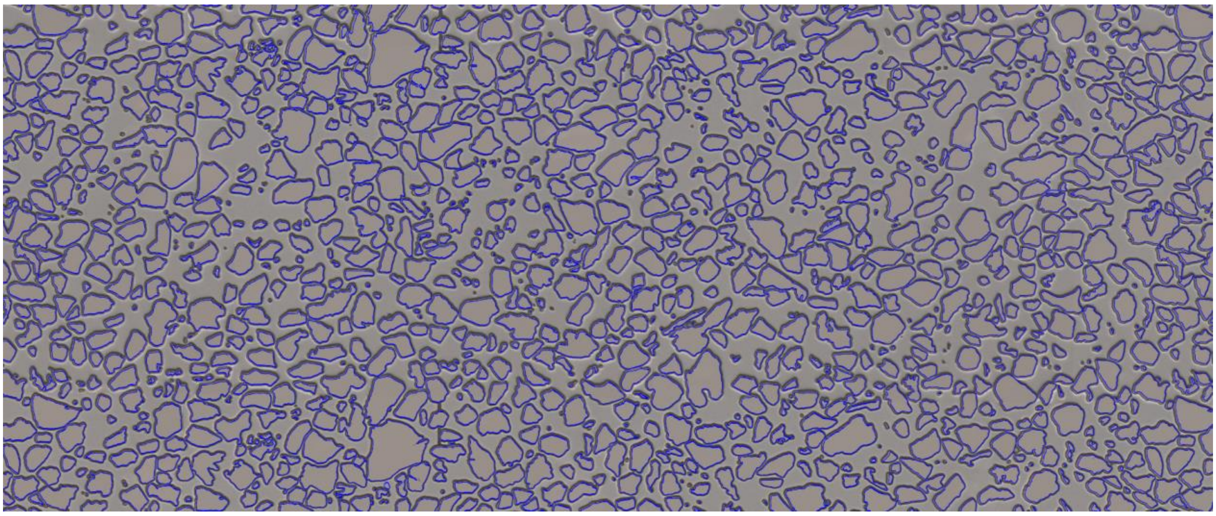

Figure 52: The contours used to calculate the porosity are drawn in blue color on the grains. The contours match well with grains, indicating that calculated porosity is a good approach.

Permeability measurements were performed on the micromodel by water injection at high pore pressure (BPR set to 100 bar) using Darcy's law. The dP values has been adjusted, so that the regression line intersect origin because when the rate is 0 the dP should be 0 (Table 2). The absolute permeability was calculated to be 2.97 $\pm$ 0.07 D.

Table 2: The measured values used to determine the absolute permeability.

Rate $[\mu l/min]$	*dP [bar]*	*Adjusted dP [bar]*	*Permeability [D]*
50	0.11	0.13	2.86
100	0.23	0.24	2.99
200	0.46	0.47	3.04
300	0.70	0.71	3.01
400	0.95	0.96	2.97

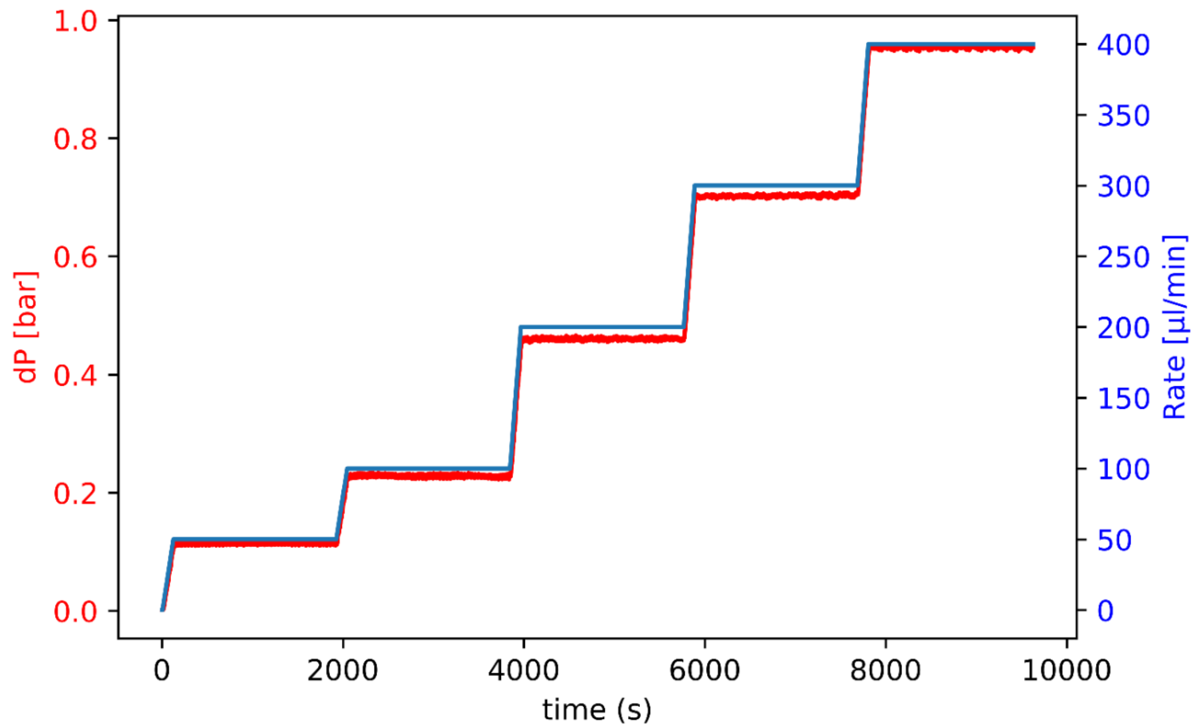

Figure 53: The measured differential pressure and injection rate plotted versus time. Five rates are used to calculate the permeability, each rate is held for 30 min. The differential pressure stabilized quickly after changes in injection rate.

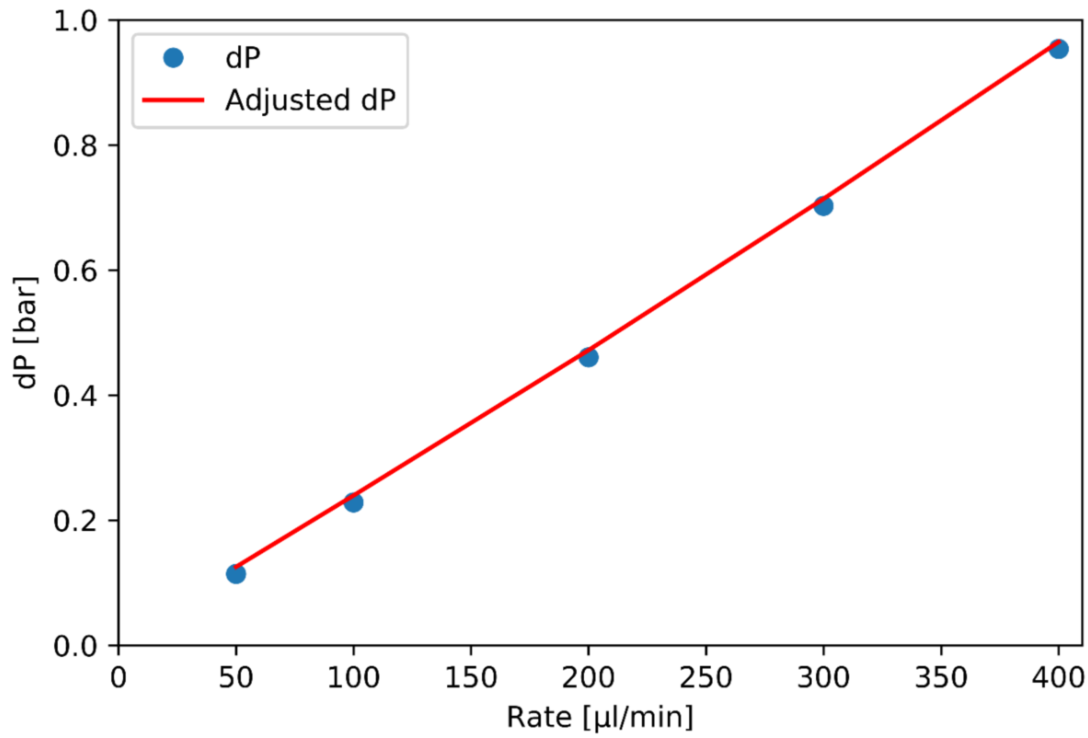

Figure 54: The measured dP and the adjusted dP plotted versus injection rate. The coefficient of determination (r^2) of dP versus injection rate regression is calculated to be 0.999, and the value used to adjust dP is 0.0112.

10. Baseline

Two experiments (*BL1* and *BL2*) were conducted without presence of foaming agents to provide baseline for subsequent injections with foaming agents to evaluate their ability to generate and stabilize CO_2 foams. The baseline experiments were conducted at the same conditions: 100 bar, room temperature, and injection rate of 4 $\mu l/min$. It was decided not to use *BL2* further in this thesis because after 20 pore volumes (PV) of CO_2 were injected, bubbles started to regenerate (this can be due to the present of some foaming agents residuals), and this would affect the subsequent injections if applied.

The threshold tool described earlier was applied to *BL1* images to obtain bubble contours. For each image, number of bubble contours and area for each bubble contour were attained by using *findContours* function in *openCV*. Bubble areas were divided into three categories ($< 10^3\ \mu m^2$, $10^3 - 10^4\ \mu m^2$, and $> 10^4\ \mu m^2$) to investigate if the bubble generation and decay depended on the bubble size in the subsequent injections. For each size category the number of bubbles were plotted as a function of PV injected CO_2 (Figure 55). The number of bubbles for each category start above zero because the CO_2 bubbles had already entered the micromodel when image acquisition started: the micromodel was already saturated with gas because in 72 seconds (time required to capture a picture of the full-model) with an injection rate of 4 $\mu l/min$ and a pore volume of 11.22 μl, 43% of the pore space will be saturated with CO_2. The acquisition of images was set to start two hours after the injection, and the first image containing CO_2 was selected manually.

The bubbles in *BL1* were mainly generated by leave-behind mechanism (Figure 59), mostly generating bubbles with sizes less than $10^4\ \mu m^2$; generation average for bubbles with size < $10^3 \mu m^2$ was 17.9 bubbles per injected PV CO_2 (BPIPV), and 12.3 BPIPV for bubble sizes $10^3 - 10^4\ \mu m^2$, whereas for larger bubbles the generation average was 3.8 BPIPV.

The total number of bubbles for *BL1* (Figure 56) was also used to compare the subsequent injections, and the total generation average was 34 BPIPV: hence, for each PV injected CO_2 the difference between bubble generation and decay is 34. *BL1* was used as baseline for all the subsequent injections in this thesis because the bubbles for all the sizes were stable and no regeneration of the bubbles occurred. For the subsequent injections, the number of bubbles generated with the presence of foaming agents is normalized the baseline bubble number for each PV value.

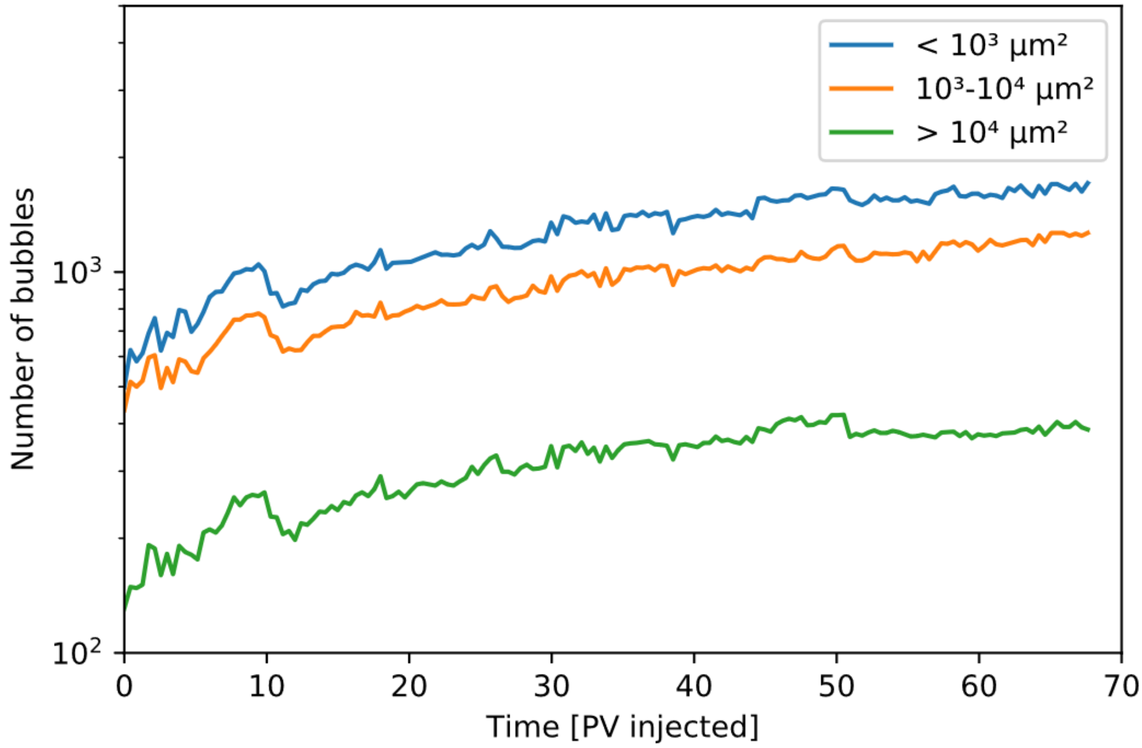

Figure 55: BL1 injection of CO_2 at 100 bar and room-temperature with a constant rate of 4 μl/min in a brine saturated micromodel. The bubble sizes are divided into 3 categories ($< 10^3\ \mu m^2$, $10^3 - 10^4\ \mu m^2$, and $> 10^4\ \mu m^2$), and the number of each category is plotted on a logarithmic scale as a function of the pore volumes injected. The number of the bubbles for all the three categories increases and are stable. This foam generation is mainly due to the leave-behind mechanism, and smaller bubbles ($< 10^4\ \mu m^2$) generates faster than the largest bubbles.

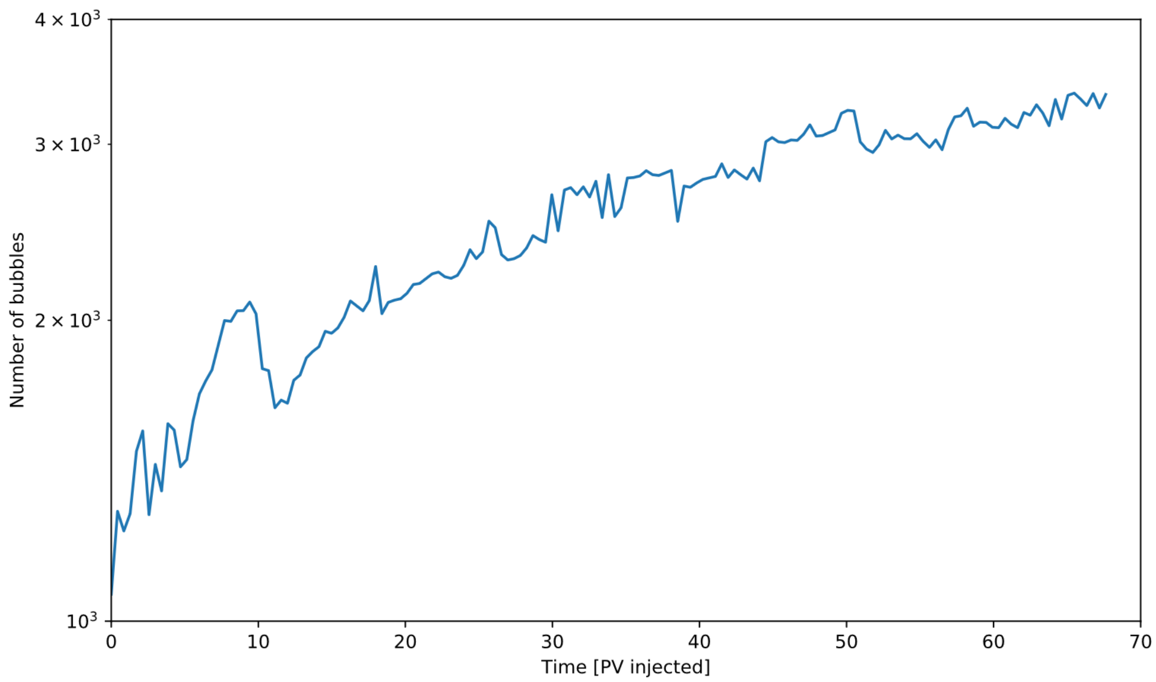

Figure 56: BL1 injection of CO_2 with a constant rate of 4 μl/min in a brine saturated micromodel. The number of bubbles plotted on a logarithmic scale as a function of pore volumes injected for Baseline. The number of the bubbles increases due to the leave-behind mechanism, and the total generation average was quantified to be 34 BPIPV.

Five different locations (Figure 57) were used to investigate the ability of foaming agents to generate and stabilize CO_2 foams in the full-model, and in specific locations (adjacent to injection and production ports). The main location ($22.66 \text{ mm} \times 18.23 \text{ mm}$) was used instead of full-model to avoid reflection noises in the edges of the micromodel, whereas locations 1 – 4 ($2.19 \text{ mm} \times 2.19 \text{ mm}$) were used to compare the foam behavior in the full-model.

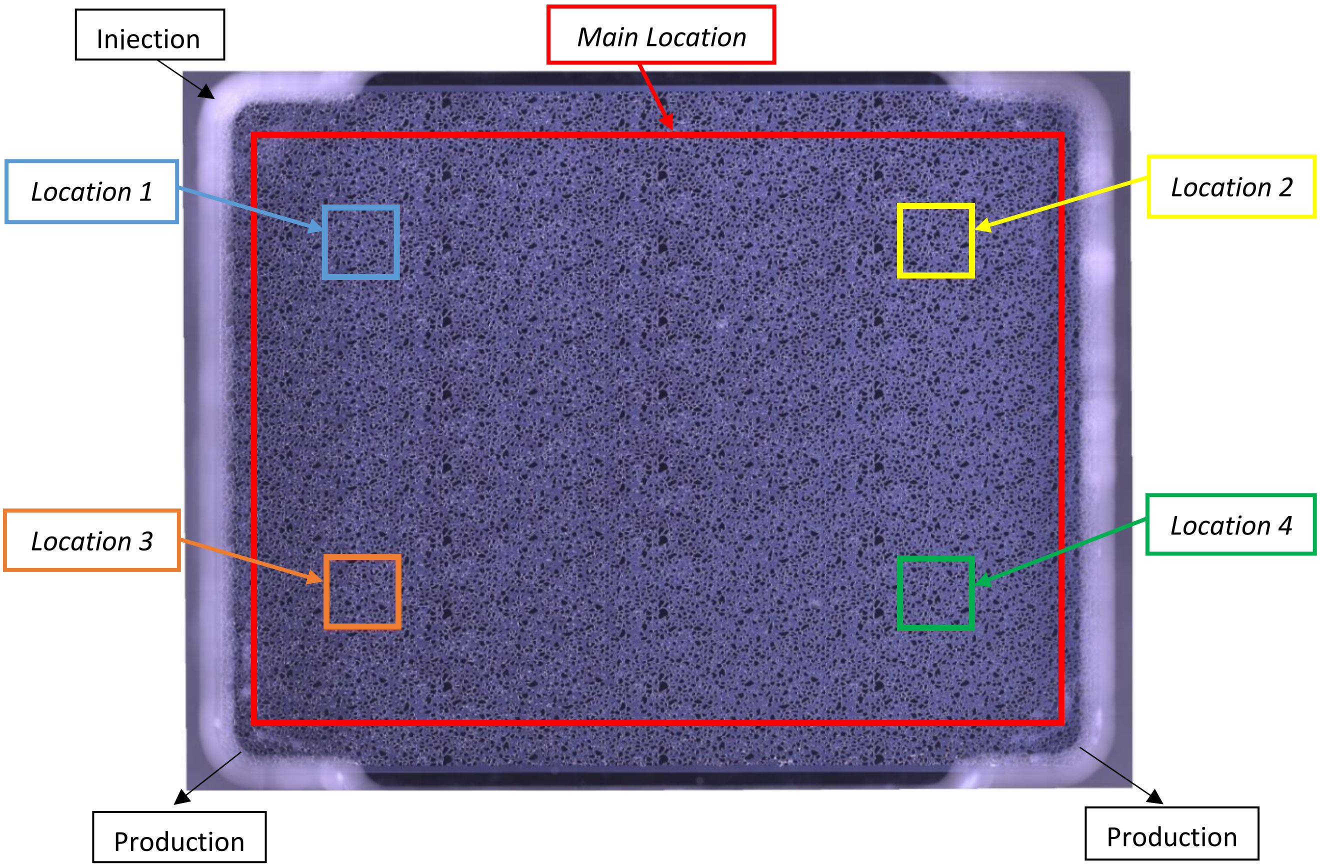

Figure 57: Different locations were studied to investigate the ability of foaming agents to generate and stabilize CO_2 foams . The main location was the area studied to compare different foaming agents performance and the synergy between them, whereas the four locations were mainly used to investigate and compare the foam behavior in different locations (adjacent to injection and production ports) for the injection.

The plot of the number of the bubbles (Figure 58) for the four locations defined above shows that bubbles in location 1 and 3 reached its peak ahead of the first image, whereas bubbles in location 2 and 4 were still in the generation period and reached a peak at PV = 15.8, and PV = 17.1, respectively. By comparing the number of bubbles for this four locations to the main location, we can observe that in the full-model the number of bubbles increased (generation average = 34 BPIPV), whereas in location 1 and 3 the number of bubbles were stable (0.2 BPIPV and 0.0 BPIPV, respectively), and the number of bubbles in location 2 and 4 in the decay period (period after reaching the peak) were also stable (-0.3 BPIPV and 0.4 BPIPV, respectively).

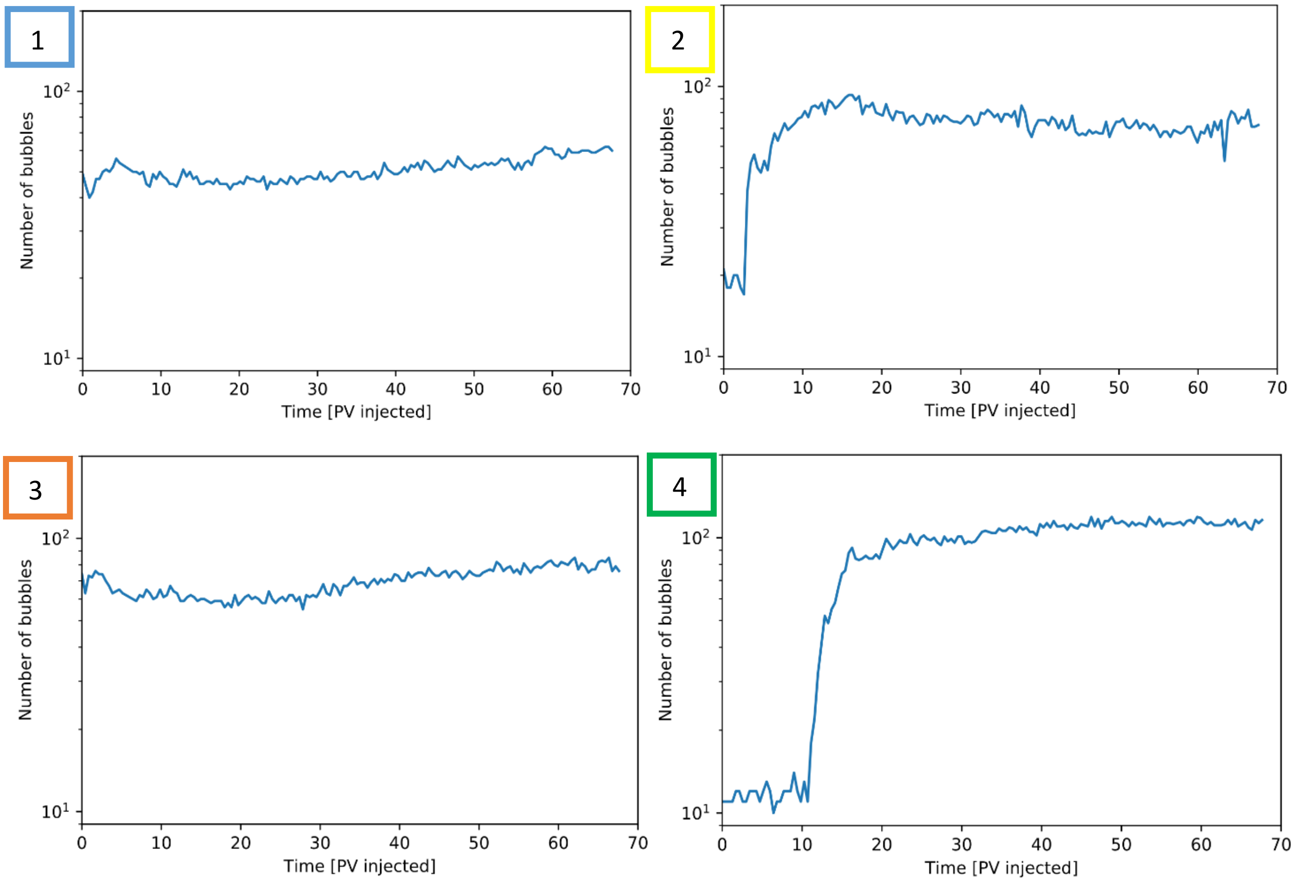

Figure 58: BL1 CO_2 injection. The number of bubbles plotted on a logarithmic scale as a function of pore volumes injected for the four locations described (Figure 57). The foam have already reached the generation peak in locations 1 and 3, whereas in locations 2 and the foam still in the generation period and reached a peak at PV = 15.8, and PV = 17.1, respectively. Unlike BL1 in main location, the number of bubbles in this locations is stable in the decay period.

11. Effect of Different Foaming Agents on Foam Generation

Four experiments were conducted at the pore-scale to evaluate the separate use of surfactants (*AQ2* and *AQ7*) and nanoparticles (*AQ6* and *AQ11*) as foaming agents for CO_2 foam in the absence of oil, see Table 1. Foaming agents were evaluated based on their ability to generate and stabilize CO_2 foams relative to baseline *BL1*. *AQ7* and *AQ11* were not used further in this thesis because in *AQ7* foam generation did not start until 12 PV CO_2 were injected, whereas in *AQ11* nanoparticles generated weak foam compared to *AQ6*.

Experiments *AQ2* and *AQ6* were conducted by performing CO_2 injection with the same conditions as for *BL1*. The use of surfactant and nanoparticles as foaming agents to generate CO_2 foam was evaluated in *Location 1* qualitatively (Figure 59). Compared to *BL1* both surfactant and nanoparticles were able to generate stronger foam, and different bubbles sizes and shapes were generated. Surfactant generated more bubbles, where the medium sized bubbles (299 of 506) were the dominant, but a few large bubbles were also generated, and the bubbles were distributed homogeneously. Nanoparticles generated mainly the small and large size bubbles, and they were not distributed homogeneously as for the surfactant, instead the small bubbles were accumulated in several different pores.

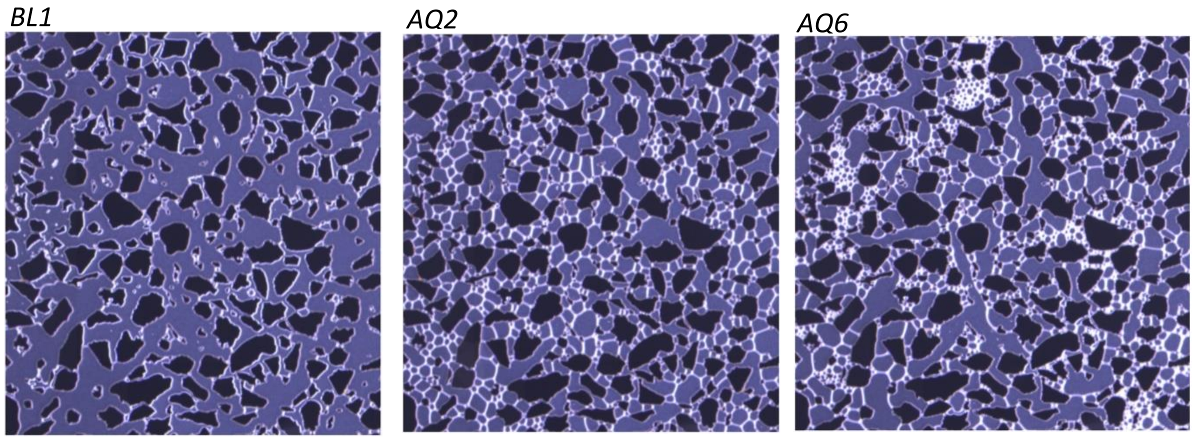

Figure 59: Comparison between BL1 (left), AQ2 (middle), and AQ6 (right) after 26.54 PV CO_2 was injected shown in location 1. Compared to BL1 both surfactant and nanoparticles were able to generate stronger foam: in Location 1 after 26.54 PV CO_2 were injected BL1 generated 45 bubbles, AQ2 generated 506 bubbles, and AQ6 generated 366 bubbles.

The normalized total number of bubbles for *AQ2* and *AQ6* (Figure 60) were also used to quantitatively compare the use of surfactants and nanoparticles as foaming agents, and to evaluate their performance to generate and stabilize CO_2 foams compared to *BL1* in full-model *(Main location)*. *AQ2* was able to generate stronger foam, and reached a significantly higher peak ($51.17 \times \mathrm{N_{baseline}}$ at PV = 5.14) compared with *AQ6* and *BL1*, but number of bubbles decreased rapidly with a generation average of -0.6 normalized bubbles per injected PV CO_2 (NBPIPV) in the decay period, whereas *AQ6* was able to stabilize the foam better than *AQ2* (0.0 NBPIPV) after the second peak (at PV=17.55).

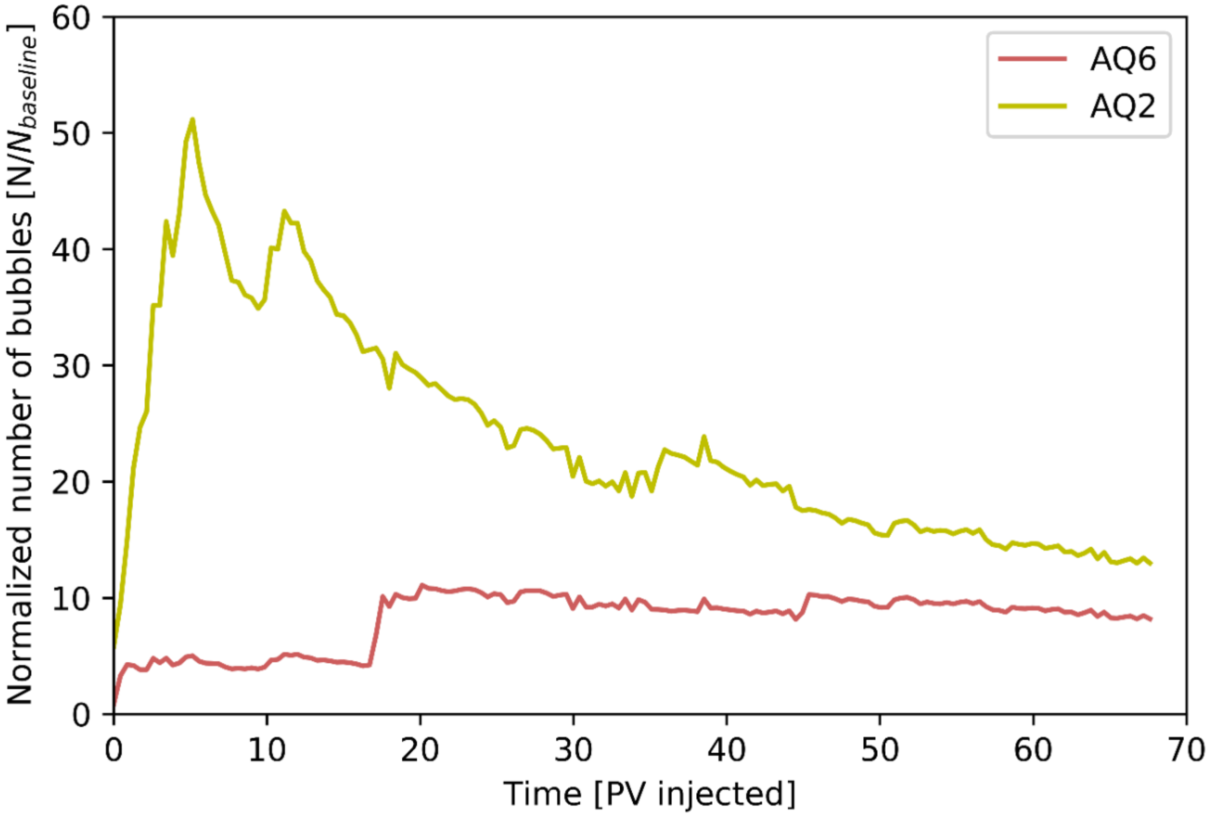

Figure 60: Normalized number of bubbles as a function of pore volume injected CO_2 for AQ2 (0.5 wt% surfactant), and AQ6 (0.15 wt% nanoparticles). Surfactant-stabilized CO_2-foam generates stronger foam compared to nanoparticle-stabilized CO_2-foam, but CO_2-foam stabilized by nanoparticles is more stable (0.0 NBPIPV) compared to surfactant-stabilized CO_2-foam (-0.6 NBPIPV) in the decay period.

The stability of the CO_2 foam for *AQ2* and *AQ6* in the decay period was also investigated for the three size categories ($< 10^3\ \mu m^2$, $10^3 - 10^4\ \mu m^2$, and $> 10^4\ \mu m^2$) (Table 3). The total generation average for *AQ2* was -583.4 BPIPV (The negative sign means that the bubbles were collapsing faster than generating): where bubble sizes less than $10^3 \mu m^2$ had a generation average of -673.4 BPIPV, bubble sizes $10^3 - 10^4\ \mu m^2$ 91.4 BPIPV, and bubble sizes $> 10^4\ \mu m^2$-1.4 BPIPV. These results show that large bubbles were stable during decay period, whereas medium size bubbles grow in the expense of the smallest bubbles, known as coalescence. The coalescence occurred due to the gas diffusion, which led to lamella rupture when the film thickness approached a critical value (5-15 nm using surfactant) (*cf.* Chapter 3.6). Figure 61 supports that film thickness was reduced during CO_2 injection for *AQ2* as the lamellae thickness decreases continually from PV = 3 to PV = 67.62. The total generation average for *AQ6* was 127.7 BPIPV: where bubble sizes less than $10^3 \mu m^2$ had a generation average of -2.1 BPIPV, bubble sizes $10^3 - 10^4\ \mu m^2$ 114.3 BPIPV, and bubble sizes $> 10^4\ \mu m^2$15.5 BPIPV. These results show that the mainly generated bubble sizes was $10^3 - 10^4\ \mu m^2$, whereas the other bubbles ($< 10^3\ \mu m^2$, and $> 10^4\ \mu m^2$) were stable, and no coalescence was observed using nanoparticles. The results for the generation average for *AQ2* and *AQ6* show that nanoparticles was able to stabilize the CO_2 foam, whereas surfactants did not stabilize the CO_2 foam in the decay period.

Table 3: The generation average for the three size categories ($< 10^3\ \mu m^2$, $10^3 - 10^4\ \mu m^2$, and $> 10^4\ \mu m^2$) for BL1, AQ2, and AQ6.

	BL1 [BPIPV]	AQ2 [BPIPV]	AQ6 [BPIPV]
$< 10^3\ \mu m^2$	17.9	-673.4	-2.1
$10^3 - 10^4\ \mu m^2$	12.3	91.4	114.3
$> 10^4\ \mu m^2$	3.8	-1.4	15.5
Total	34.0	-583.4	127.7

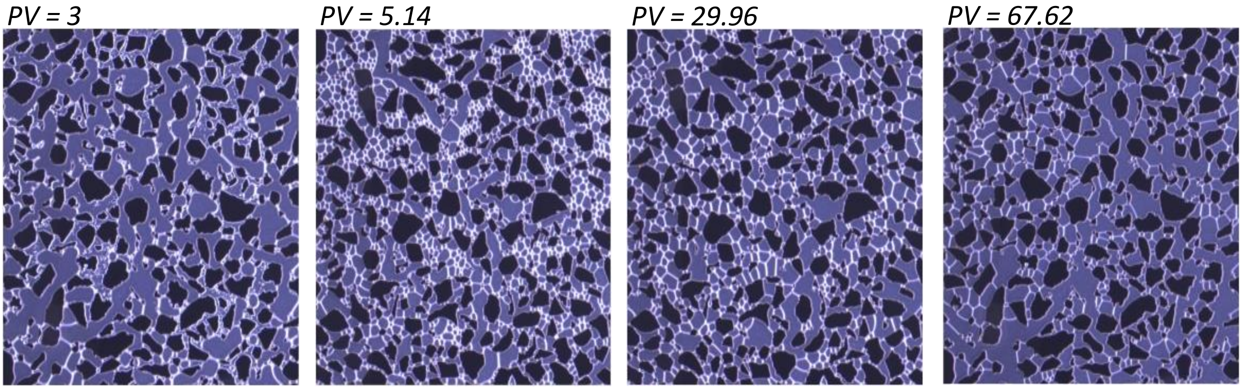

Figure 61: Series of images for AQ2 at different PV (3, 5.14, 29.96, and 67.62) shown in Location 1. The lamellae thickness decreases continually from PV = 3 to PV = 67.62, where the medium size bubbles grow in the expense of the smallest bubbles.

In addition the ability of foaming agents to stabilize CO_2 foams adjacent to the injection and the production ports were investigated for *AQ2* and *AQ6* in the four locations (Figure 57) for the decay period (Table 4). The foam destabilizes fastest in *Location 3* both for *AQ2* (-6.4 BPIPV), and *AQ6* (-1.2 BPIPV), and were most stable in *Location 2* (-3.3 BPIPV) for *AQ2*, and in *Location 1* for *AQ6*.

Table 4: The generation average for BL1, AQ2, and AQ6 in the four Locations (Figure 57).

	BL1 [BPIPV]	AQ2 [BPIPV]	AQ6 [BPIPV]
Location 1	0.2	-4.9	3.6
Location 2	-0.3	-3.3	0.9
Location 3	0.0	-6.4	-1.2
Location 4	0.4	-5.7	1.9

12. Effect of Surfactant Concentration on Foam Generation

Two experiments (*AQ3* and *AQ8*, Table 1) investigated the effect of surfactant concentration on foam generation and stability in the absence of oil. *AQ8* was not used in this thesis because the CO_2 entered the micromodel later compared to the other experiments, and only 35 PV was monitored with the microscope. *AQ3* (0.05 wt% surfactant) is compared qualitatively and quantitatively to *AQ2* (0.5 wt% surfactant) throughout this chapter to investigate the effect of increasing surfactant concentration on the foam texture and number of bubbles (NB) using identical experimental conditions. The pore-scale observations (*AQ2* and *AQ3*) were compared with previous work of CO_2 foam performed on core-scale.

The effect of surfactant concentration increase was evaluated qualitatively in the four locations at PV = 26.54 (Figure 62) to describe the bubble texture adjacent to the injection and production ports: texture for *AQ3* and *AQ2* generally appear similar, except the high concentration of the aqueous phase in *Location* 2 for *AQ3* observed as thick lamellae, and the channels in *Location 1* for *AQ3* and in *Location 2* for *AQ2*. For *AQ3* the channel observed in *Location 1* and the difference in lamellae thickness between *Location 1* (thin) and *Location 2* (thick) indicate that the CO_2 was mainly flowing through the left side of the micromodel, whereas the opposite was true for *AQ2* (CO_2 was mainly flowing through the right side of the micromodel).

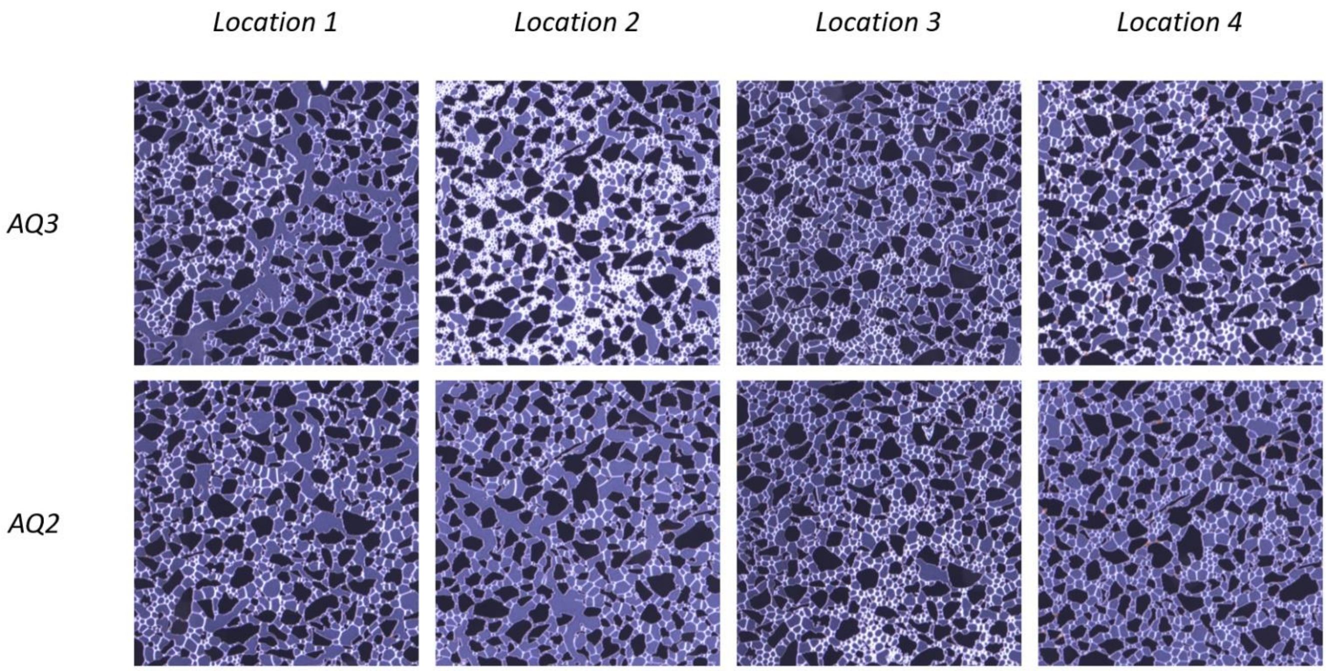

Figure 62: Series of images for AQ3 and AQ2 in the four locations (Figure 57) at PV = 26.54. The texture of the bubbles looks overall similar for AQ3 and AQ2, except the high concentration of the aqueous phase in Location 2 for AQ3, and the channels in Location 1 for AQ3 and in Location 2 for AQ2 that indicate different flow paths for AQ2 and AQ3.

To investigate the CO_2 flow path, and visualize the channels in the full-model for *AQ3* and *AQ2*, density plots (hexagonal binning plots) were used. The number of hexagons in the x-direction and the y-direction were set to 150 and 173, respectively, and for each hexagonal the NB centers were counted and represented by an color from the *inferno* color map (black when NB centers = 0, and yellow when NB centers $\geq$ 10). The channels are represented by few bubble centers, therefore they will be able to be detected using a hexagonal plot. The *Main Location* (Figure 57) was used to obtain the hexagonal binning plots over the full-model. Figure 63 shows the density plots for *AQ2* and *AQ3* at PV = 26.54. Two large channels were observed across the entire model in *AQ2*: one in the middle, and the second on the right. The CO_2 was flowing mainly through the middle and right side of the micromodel in *AQ2*, and this support the indication made based on the raw images from the four locations. A large black area was observed in the top right side of the micromodel in *AQ3*. After reviewing both the raw and threshold images it was concluded that this area was filled with small bubbles. The script was programed to remove all the objects that have area less than $0.2 \times 10^3 \mu m^2$: this was applied to remove noises, but in this case removed the exceptionally small bubbles also. Similar to *AQ2*, two large channels were observed across the entire pore-space during *AQ3*: one in the middle and the second on the left, where the left channel seems to be connected with the one in the middle. The CO_2 was flowing mainly through the middle and left side of the micromodel in *AQ3*, and results was also supporting the indication made based on the raw images from the four locations. Based on the qualitative (*Figure 62*) and quantitative (Figure 63) comparison for *AQ2* and *AQ3* at PV = 26.54, using a low concentration of surfactant (0.05 wt%) the flow do not block the pores near the injection port, and CO_2 flows mainly through the left and the middle side of the micromodel, whereas using a high concentration of surfactant (0.5 wt%) the flow blocks the pores adjacent to the injection port and the CO_2 flows mainly through the right and the middle side of the micromodel.

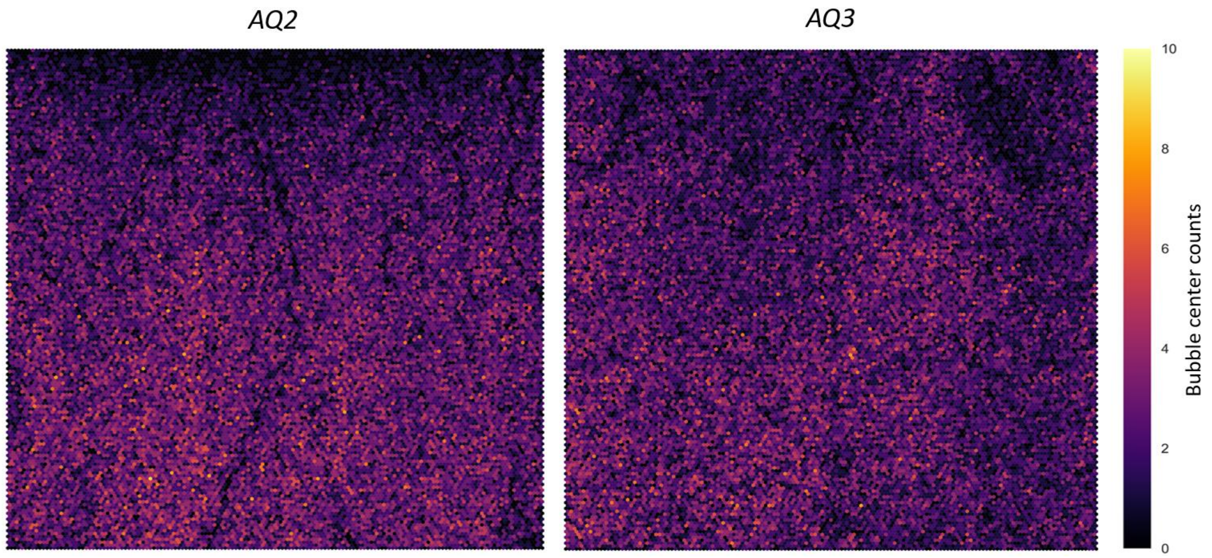

Figure 63: Density plots for AQ3 and AQ2 at PV = 26.54. Two large channels observed in the middle and the right side of the micromodel in AQ2 indicating the block-off of the flow adjacent to the injection port and the diversion of flow to the middle and the right side when using a high concentration of surfactant (0.5 wt%). Two large channels was also observed in AQ3 in the middle and the left side of the micromodel, the channel in the left seems to be connected to the one in the middle, and the flow is not blocked adjacent to the injection port using low concentration of surfactant (0.05 wt%).

The normalized NB for the three size categories ($< 10^3\ \mu m^2$, $10^3 - 10^4\ \mu m^2$, and $> 10^4\ \mu m^2$) for *AQ2* and *AQ3* (*Figure 64*) were also used to quantitatively investigate the effect of surfactant concentration on CO_2 foam generation and stability in full-model. In the foam generation period the size categories reaches the peaks at different PV for *AQ2* ($< 10^3\ \mu m^2$: 79.74 at PV = 4.71, and $10^3 - 10^4\ \mu m^2$: 43.58 at PV = 12.41) and for *AQ3* ($< 10^3\ \mu m^2$: 24.93 at PV = 24.82, and $10^3 - 10^4\ \mu m^2$: 25.20 at PV = 12.41). *AQ2* generated a stronger foam compared to *AQ3*, but in the decay period *AQ3* (-33.1 BPIPV in total) was more stable than *AQ2* (-583.4 BPIPV in total). As described in the previous chapter, the coalescence was observed for *AQ2*, and it was observed in AQ3 also, as the generation average for small bubbles was quantified to be -63.8, and 51.3 for the medium size bubbles (Table 5).

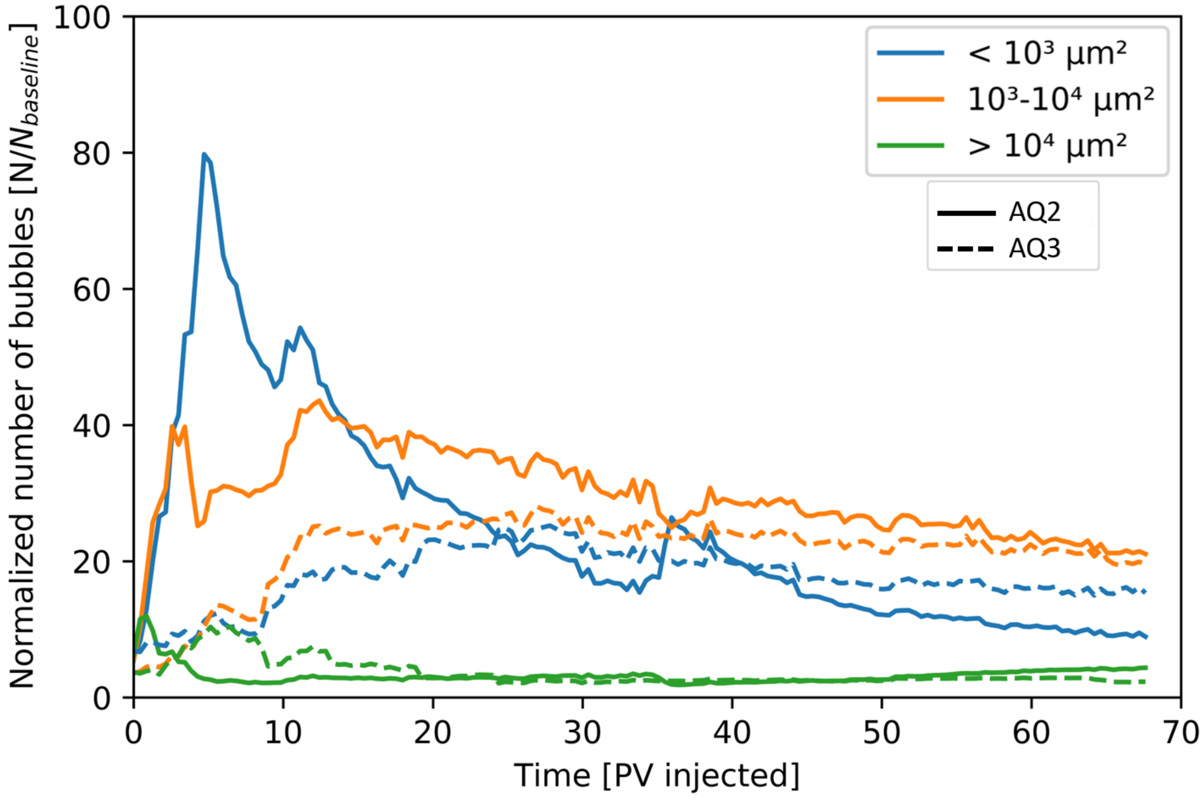

Figure 64: Normalized number of bubbles as a function of pore volume injected CO_2 for AQ2 (0.5 wt% surfactant), and AQ3 (0.05 wt% surfactant). AQ2 generated a stronger foam compared to AQ3, but in the decay period AQ3 (-33.1 BPIPV in total) was more stable than AQ2 (-583.4 BPIPV in total).

Table 5: The generation average for the three size categories ($< 10^3\ \mu m^2$, $10^3 - 10^4\ \mu m^2$, and $> 10^4\ \mu m^2$) for AQ2, and AQ3.

	AQ2 [BPIPV]	*AQ3 [BPIPV]*
$< 10^3\ \mu m^2$	-673.4	-63.8
$10^3 - 10^4\ \mu m^2$	91.4	51.3
$> 10^4\ \mu m^2$	-1.4	-20.6
Total	-583.4	-33.1

The effect of surfactant concentration on foam mobility has been studied in core plugs extensively (Alkan et al., 1991; Dixit et al., 1994; Lee & Heller, 1990). The results of these experiments show that the mobility declines with increasing surfactant concentration. The same was observed in the pore scale in this thesis, as the NB increases when increasing surfactant concentration. The increase in the NB blocks the flow pathways and result in an increase in the differential pressure and a decrease in foam mobility.

13. Effect of the Injection Rate on Foam Generation

One experiment (*AQ1*, Table 1) was conducted with an injection rate of 1 $\mu l/min$ to investigate the effect of the injection rate on foam generation and stability on the pore space in the absence of oil. This experiment was not successfully repeated because of a small undetected leakage in the system. *AQ1* (0.5 wt% surfactant, 1 $\mu l/min$) was compared with *AQ2* (0.5 wt% surfactant, 4 $\mu l/min$) throughout this chapter qualitatively and quantitatively to investigate the effect of increasing injection rate on the foam texture and NB on pore-scale, and these results were compared with previous work performed on core-scale.

AQ1 was conducted by performing CO_2 injection in the same pressure and temperature conditions as for *AQ2*, and the decrease of the injection rate was evaluated qualitatively in the four locations at PV = 26.54 (Figure 65) to describe the texture of the bubbles adjacent to the injection and production ports. For both *AQ1* and *AQ2* stronger foam was observed adjacent to the production ports compared to the top part of the micromodel, where the bubbles were more concentrated and smaller, and blocks the flow path. The texture of the foam looks generally similar for *AQ1* and *AQ2*, and the same flow path was observed: concentrated bubbles in *Location 1*, and some channels in *Location 2* indicate that the flow was blocked off in the left side and diverted to the right side of the micromodel where the top right port was plugged.

The normalized NB plots were not used in this chapter because of the lack of a baseline for *AQ1* (*BL1* could not be used because of the different injection rates used, and the lack of baseline data for three of four images), instead the NB was calculated for the four locations at PV = 26.54 to obtain quantitative data to compare performance of *AQ1* and *AQ2* (Figure 65). For each location the NB for *AQ2* is higher than the NB for *AQ1*, indicating stronger foam with higher injection rate. The effect of the injection rate on foam mobility has been studied extensively on core plugs (Heller et al., 1985; Yang & Reed, 1989). The result of these experiments shows that foam mobility was found "shear thinning" at high rates and "shear thickening" at low rates. (Rognmo, 2019) has conducted experiments with a surfactant solution for two rates (7.2 $\mu l/min$ and 14.4 $\mu l/min$) and observed that foam was "shear thinning". The experiments (*AQ1* and *AQ2*) conducted in this thesis show that the number of bubbles increase when increasing the injection rate. The NB increase blocks the flow pathways, resulting in increased differential pressure and reduced foam mobility. The decrease in foam mobility with increasing injection rate means that foam was "shear thickening". This observation on the pore-scale was comparable with the observations in the literature on the core-scale for low rates, but not comparable with Rognmo's observation: this may be due to the different rate ranges used, where in this thesis pore-scale experiments (*AQ1* and *AQ2*) was performed using low rates (1 $\mu l/min$ and 4 $\mu l/min$), whereas Rognmo conducted the experiments on the core-scale using higher rates (7.2 $\mu l/min$ and 14.4 $\mu l/min$). Because the acquisition of a full-model image requires 72 seconds, the rate could not be increased any more to not lose important data between each full-model acquisition. In order to study the effect of the injection rate on foam mobility on pore space in more detail, a small field of view can be chosen so that acquisition of a full-model image requires only a few seconds, and the injection rate can be increased much more than 4 $\mu l/min$.

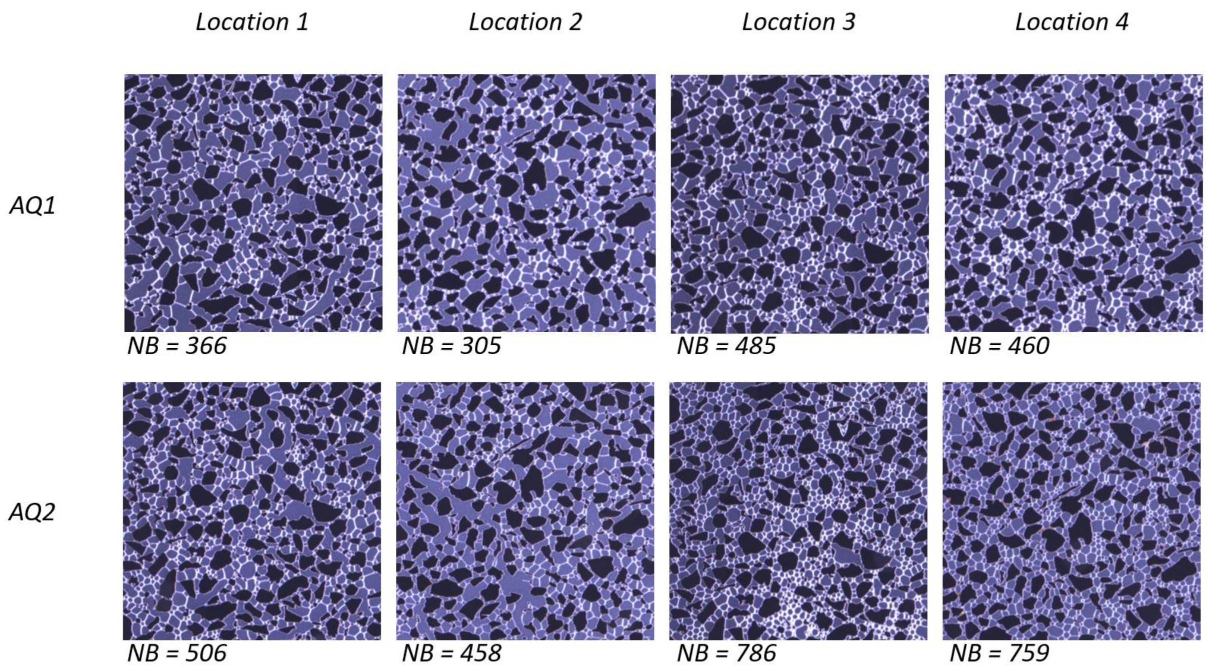

Figure 65: *Series of images for AQ1 and AQ2 in the four locations (Figure 57) at PV = 26.54. The NB for each image is shown underneath it. The texture of the bubbles looks overall similar for AQ1 and AQ2,and stronger foam (increased NB) was observed adjacent to the production ports (Location 3 and Location 4) compared to the top part of the micromodel (Location 1 and Location 2) both for AQ1 and AQ2, indicating the block-off of the flow adjacent to the injection port and the diversion of flow to the right side of the micromodel.*

14. The Synergy Between Nanoparticles and Surfactants to Stabilize Foams

The comparison of surfactant- and nanoparticle-stabilized foams conducted in this thesis by analyzing the NB on pore-scale, and the apparent viscosity comparison made by Rognmo on core-scale indicate that surfactants have a higher ability to generate foams, whereas nanoparticles display a significant potential to stabilize foams. A synergy between surfactants and nanoparticles, therefore, might prove beneficial in a CCUS context. Two experiments (*AQ4* and *AQ9*, Table 1) with injection fluid (0.5 wt% surfactant + 0.15 wt% nanoparticles), and two other experiments (*AQ5* and *AQ10*, Table 1) with injection fluid (0.5 wt% surfactant + 0.015 wt% nanoparticles) were conducted to investigate the effect of synergy between nanoparticles and surfactants on foam generation and stability on the pore space in the absence of oil. *AQ9* and *AQ10* were not used further in this thesis because in *AQ9* foam was already generated at PV = 0 and almost reached the peak, whereas in *AQ10* foam generation did not start until 11 PV CO_2 were injected, but they followed the same trend as *AQ4* and *AQ5*. *AQ4* and *AQ5* were compared to *AQ2* (0.5 wt% surfactant) throughout this chapter qualitatively and quantitatively to investigate the effect of combining nanoparticles and surfactants on the foam texture and NB on pore-scale in the absence of oil.

AQ4 and *AQ5* were conducted by performing CO_2 injection in the same conditions as for *AQ2*, and the effect of combining nanoparticles and surfactants was evaluated qualitatively in the four locations at PV = 26.54 (Figure 66) to describe the bubble texture adjacent to the injection and production ports. The texture of the foam looks generally similar and the NB looks equivalent for all the three experiments, except some channels were observed in *Location 1* and *Location 4* for both *AQ4* and *AQ5* and were not observed in *AQ2*. To describe these channels and the flow paths of the CO_2 in more details, density plots (hexagonal plots) were utilized (Figure 67). For *AQ4*, density plots show a continuous channel at the right side and some discontinuous channels at the top and top left side of the micromodel, and for *AQ5* two continuous channels were observed at the middle and at the right side of the micromodel. These results were comparable with the result for *AQ2*: the flow was blocked off in the left side and diverted to the right side of the micromodel where the top right port was plugged. To investigate the stability of the channels, a series of density plots for *AQ2* (*AQ4* and *AQ5* were similar to *AQ2*, therefore only *AQ2* density plots were shown) were used (Figure 68). The plots show channels formation start at PV = 3.42, the two channels in the middle and right side of the micromodel were stable during the entire injection, with small changes in the path in the bottom part of the micromodel, whereas the one in the left side was unstable and discontinuous during CO_2 injection. The front of the foam was observed to move backward against the direction of the flow as more bubbles were generated in the pores, and the dP data supports that the flow direction was from inlet to outlets. Backward front movement was observed in *AQ4* and *AQ5* also. (Apaydin & Kovscek, 2001; Nguyen et al., 2003; Mohammad Simjoo et al., 2013) have reported this backward front movement in the core plugs. (M. Simjoo & Zitha, 2019) explained the appearance of the secondary backward foam front by the change in the foam properties in the direction against the flow. They attribute this secondary backward front movement to a rheological transition during foam flow, as soon as the gas saturation reaches a characteristic value the foam transits from a weak state to a strong state.

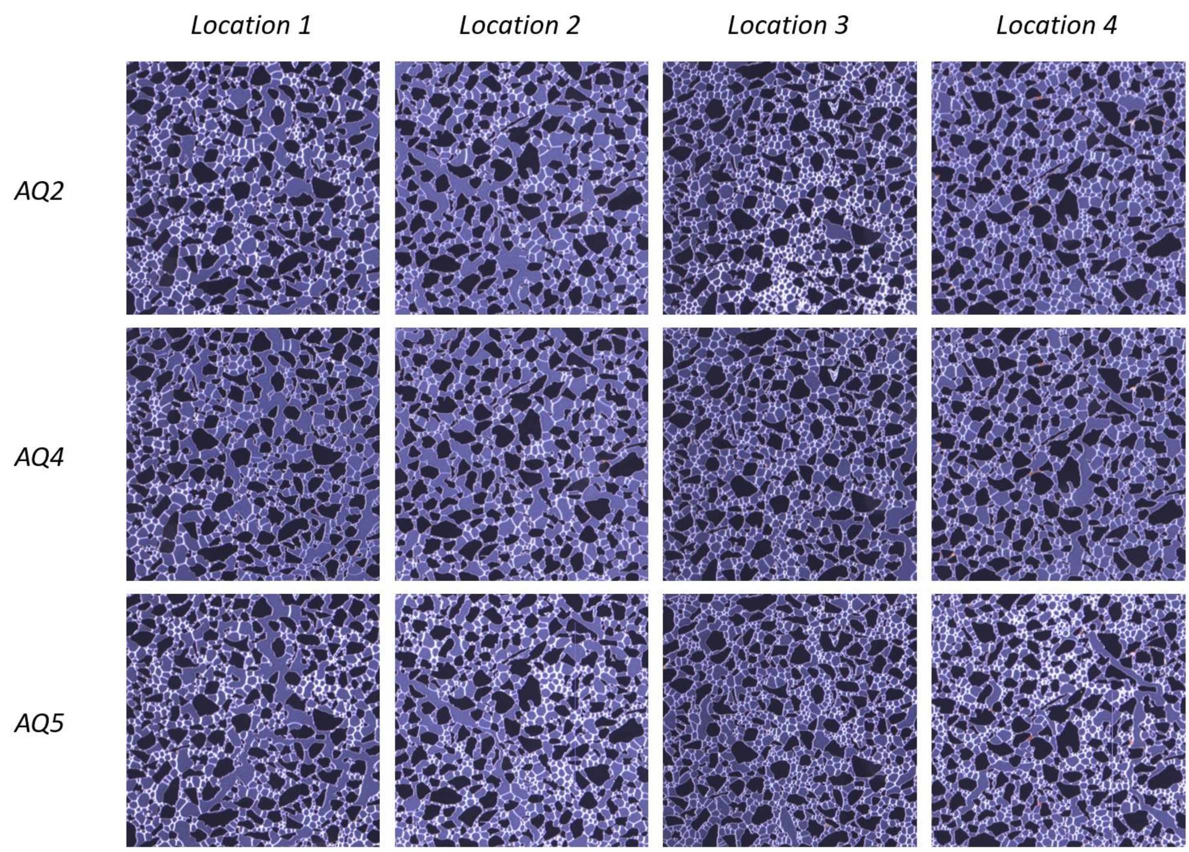

Figure 66: *Series of images for AQ2, AQ4, and AQ5 in the four locations (Figure 57) at PV = 26.54. The texture of the bubbles looks overall similar for all the injection shown. The texture of the foam looks generally similar and the NB looks equivalent for all the three experiments, except the channels in Location 1 and Location 4 for both AQ4 and AQ5 are not to find in AQ2.*

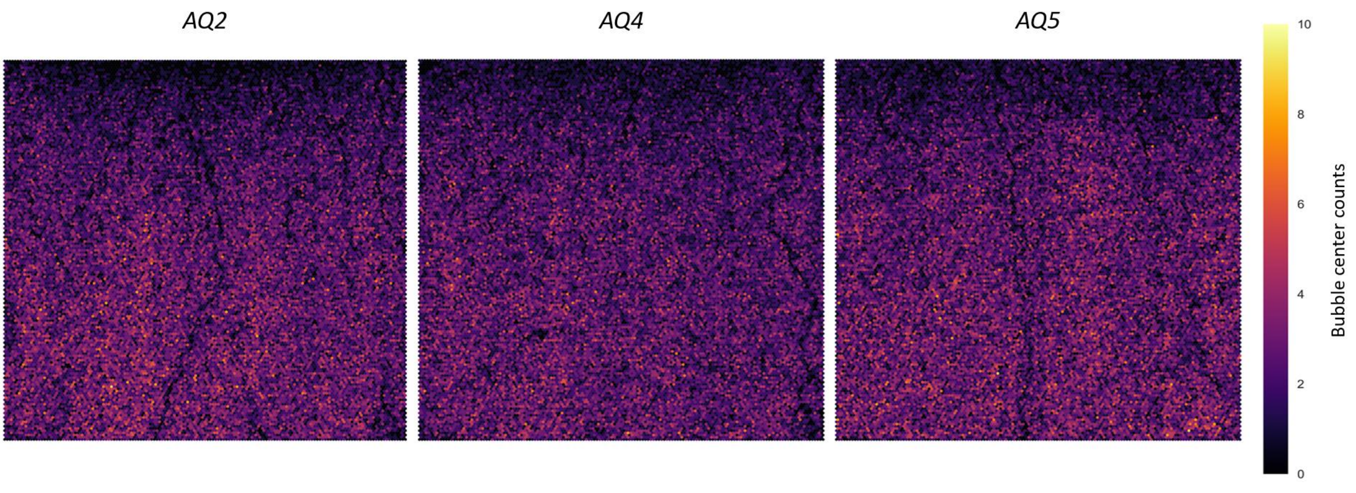

Figure 67: Density plots for AQ2, AQ4 and AQ5 at PV = 26.54. Two continuous channels in the middle and the right side of the micromodel in AQ2 and AQ5, and one in the right side of the micromodel in AQ4 indicating the block-off of the flow adjacent to the injection port and the diversion of the flow to the right side of the micromodel where the top right port was plugged.

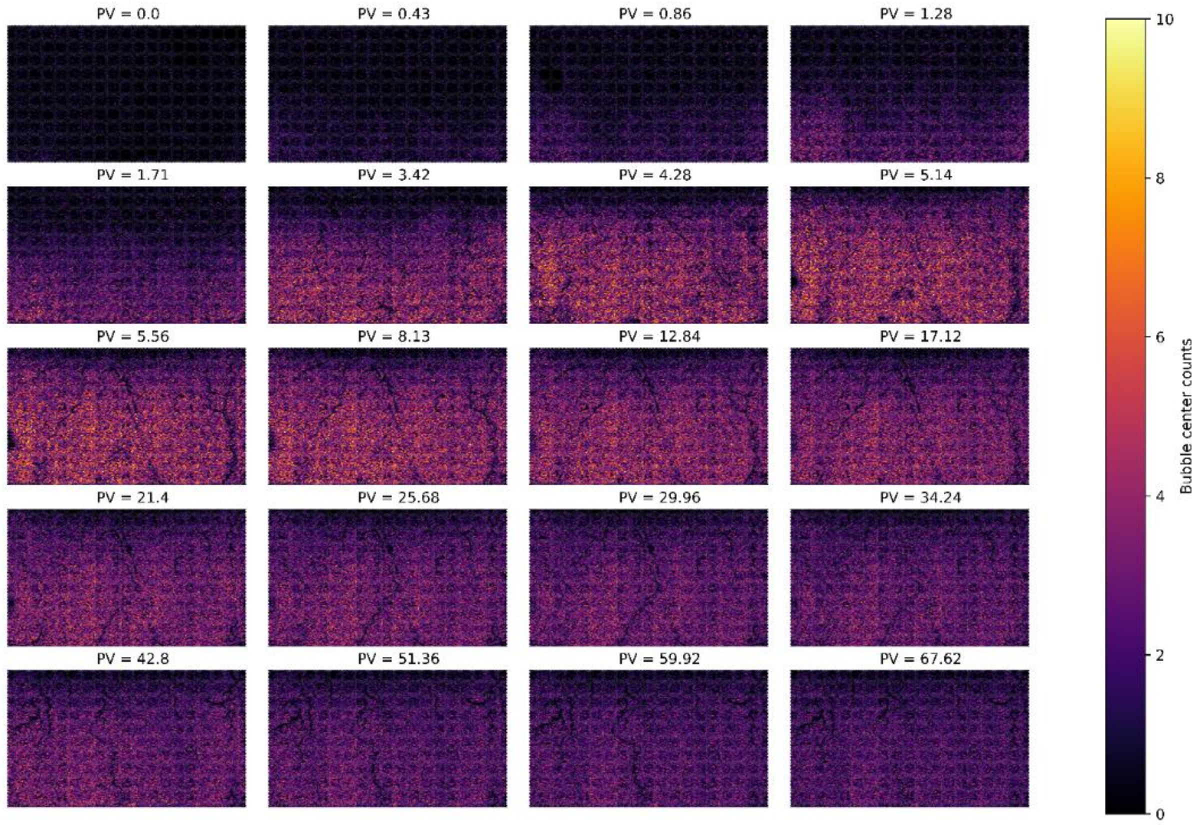

Figure 68: *Series of density plots for AQ2. The plots show channels formation start at PV = 3.42, the two channels in the middle and right side of the micromodel are stable during the entire injection, with some small changes in the path in the bottom part of the micromodel, whereas the one in the left side is unstable and discontinuous during CO_2 injection. The front of the foam was observed to move backward against the direction of the flow as more bubbles were generated in the pores.*

The normalized total NB (Figure 69), and the normalized NB for the three size categories ($< 10^3\ \mu m^2$, $10^3 - 10^4\ \mu m^2$, and $> 10^4\ \mu m^2$) (Figure 70) for *AQ2*, *AQ4*, and *AQ5* were used to quantitatively investigate the effect of combining nanoparticles and surfactants at pore-scale on CO_2 foam generation and stability in full-model in the absence of oil. The same foam generation and decay trend were observed in the normalized total NB plot for all the three injections (*AQ2*, *AQ4*, and *AQ5*), but they reached different peaks (*AQ2*: 51.17 × $N_{baseline}$ at PV = 5.14, *AQ4*: 39.5 × $N_{baseline}$ at PV = 5.56, and *AQ5*: 46.41 × $N_{baseline}$ at PV = 5.14) at approximately the same PV. In *AQ4* foam regeneration was observed at PV = 62.06, with a generation average of -0.6 NBPIPV (from PV = 62.06 to PV = 67.62), whereas the generation average at the same NB value was -0.3 NBPIPV (from PV = 30.82 to PV = 36.38): the regenerated bubbles were more unstable. The same foam generation and decay trend was also observed for all the three categories in the normalized NB plot for all the three injections (*AQ2*, *AQ4*, and *AQ5*). In the foam generation period the NB for the smallest and medium size bubbles differed somewhat, but in the decay period (as more CO_2 was injected) the NB number approached the same value for all the three categories, except the smallest bubbles in *AQ4* because of the regeneration described earlier. In addition, the generation average for all the three size categories were quantified for all the injections (Table 6). The generation average also shows the same trend for all the injections, and the coalescence was observed for all the injection with approximately the same rate for both the decay of the smallest bubbles (*AQ2*: -673.4, *AQ4*: -443.4 (small compared to *AQ2* and *AQ4* because of the regeneration of the smell bubbles), and *AQ5*: -613.5) and the generation of the medium size bubbles (*AQ2*: 91.4, *AQ4*: 114.0, and *AQ5*: 115.5). The results presented in this chapter conducted in the pore space indicate that the foam generation and stability in the pore-scale are independent of the nanoparticles in the absence of oil, with the surfactant concentrations studied.

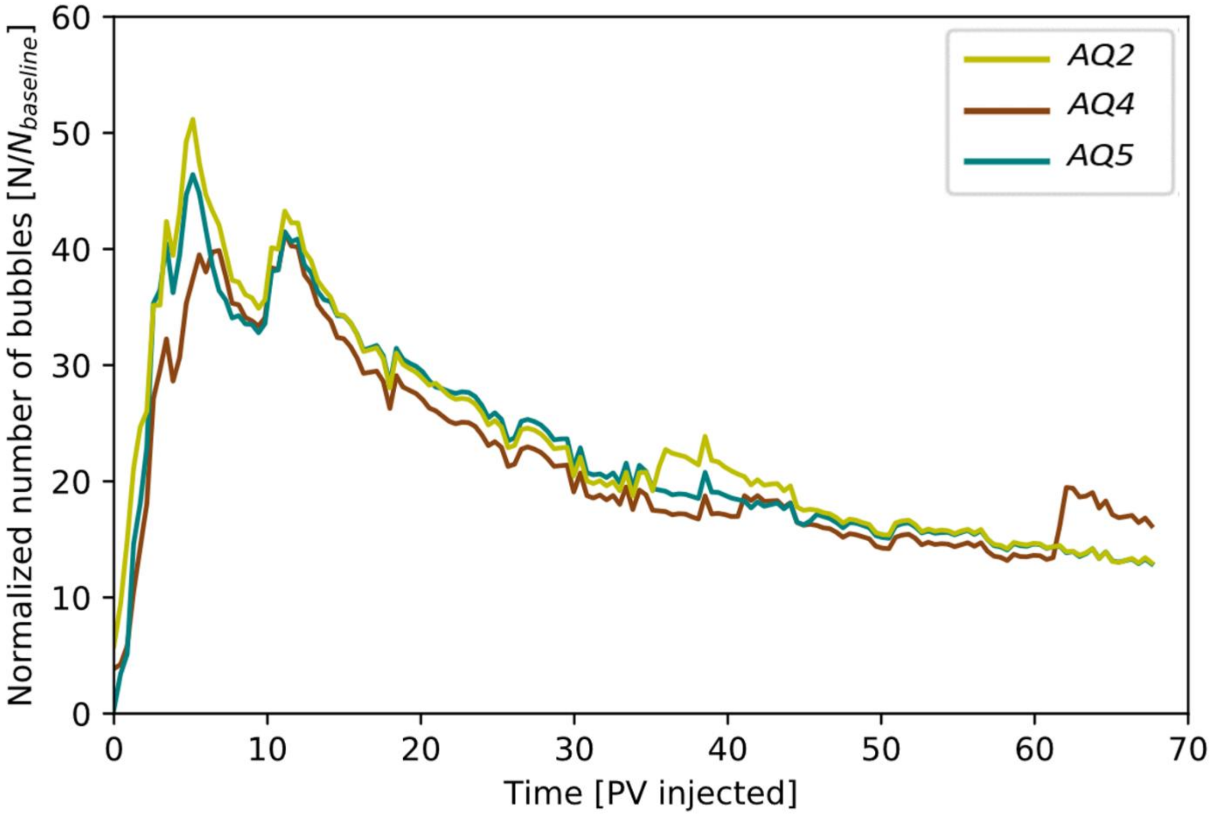

Figure 69: Normalized number of bubbles as a function of pore volume injected CO_2 for AQ2 (0.5 wt% surfactant), AQ4 (0.5 wt% surfactant + 0.15 wt% nanoparticles), and AQ5 (0.5 wt% surfactant + 0.015 wt% nanoparticles). The same trend was observed for all the three injections, but they reached different peaks (AQ2: 51.17 × $N_{baseline}$ at PV = 5.14, AQ4: 39.5 × $N_{baseline}$ at PV = 5.56, and AQ5: 46.41 × $N_{baseline}$ at PV = 5.14) around the similar PV, and in AQ4 foam regeneration was observed at PV = 62.06.

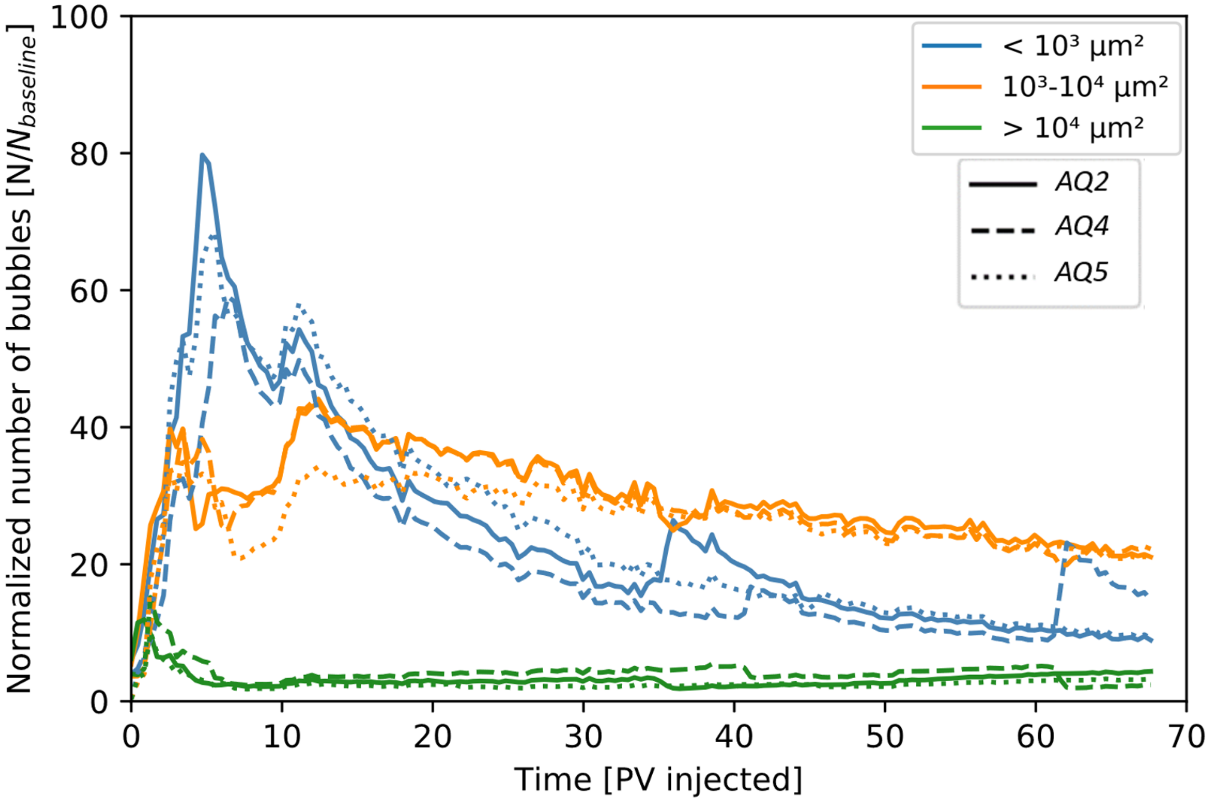

Figure 70: *Normalized number of bubbles for the three categories ($< 10^3\ \mu m^2$, $10^3 - 10^4\ \mu m^2$, and $> 10^4\ \mu m^2$) as a function of pore volume injected CO_2 for AQ2 (0.5 wt% surfactant), AQ4 (0.5 wt% surfactant + 0.15 wt% nanoparticles), and AQ5 (0.5 wt% surfactant + 0.015 wt% nanoparticles). In the foam generation period the NB for the smallest and medium size bubbles were a little far apart for all the injections, but as more CO_2 was injected in the decay period the NB for all the three injection approached the same value for all the three categories, except the smallest bubbles in AQ4 because of the regeneration described earlier.*

Table 6: The generation average for the three size categories ($< 10^3\ \mu m^2$, $10^3 - 10^4\ \mu m^2$, and $> 10^4\ \mu m^2$) for AQ2, AQ4, and AQ5.

	AQ2 [BPIPV]	*AQ4 [BPIPV]*	*AQ5 [BPIPV]*
$< 10^3\ \mu m^2$	-673.4	-443.4	-613.5
$10^3 - 10^4\ \mu m^2$	91.4	114.0	115.5
$> 10^4\ \mu m^2$	-1.4	-20.4	-4.1
Total	-583.4	-349.8	-502.1

15. Calcite Precipitation

The CO_2 storage in carbonate reservoirs is a complicated process due to the reactivity between the calcite minerals and the low pH fluids, and in order to investigate this reactivities at pore-scale, calcite minerals had to be precipitated inside the micromodel. The activation of the *Sporosarcina pasteurii* bacteria inside the micromodel was not fully developed during this thesis. The main problems of activating the bacteria inside the micromodel were the plugging of the micromodel and the uneven distribution of the bacteria. The micromodel can be plugged in the ports, channels, and even in the pores. Figure 71 shows the plugging of the top right port and channel. The reactant was injected through the top, right port, and at the moment the reactant reached the micromodel, a significant amount of calcite was precipitate, and the port was plugged after the reactant reached only few pores. To avoid this problem, growth medium has been injected with a high rate (10 µl/min) through the top left port and produced through the top right port. With this approach, bacteria was removed from the top ports and the top channel, and calcite precipitated in the pore space rather than the channel.

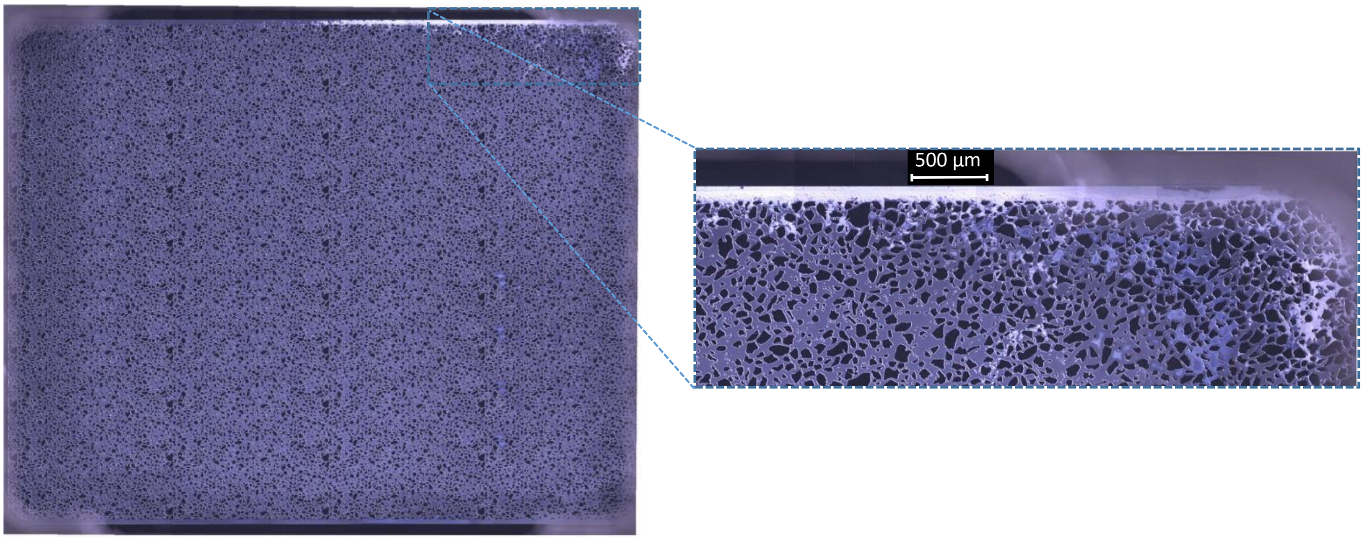

Figure 71: Reactant injection from the top right port in a micromodel saturated with bacteria and growth medium at room temperature and atmospheric pressure with a constant rate of 5.7 µl/min. The injection port and the top channel were plugged due to the high amount of calcite precipitation in this location.

When all the ports were plugged by calcite, the hydrochloric acid could not be injected in the pore space because the lines were already filled with other fluid. One possible approach was to inject with a constant pressure (2 bar overpressure) in the stagnant fluid volume in the injection tube to facilitate diffusion of the acid to the micromodel. Rather than using this approach, the micromodel was dissembled and immerged in acid for one week (Figure 72). The calcite in the ports was dissolved, and the fluids could be injected into the pore space using constant rates rather than constant pressures.

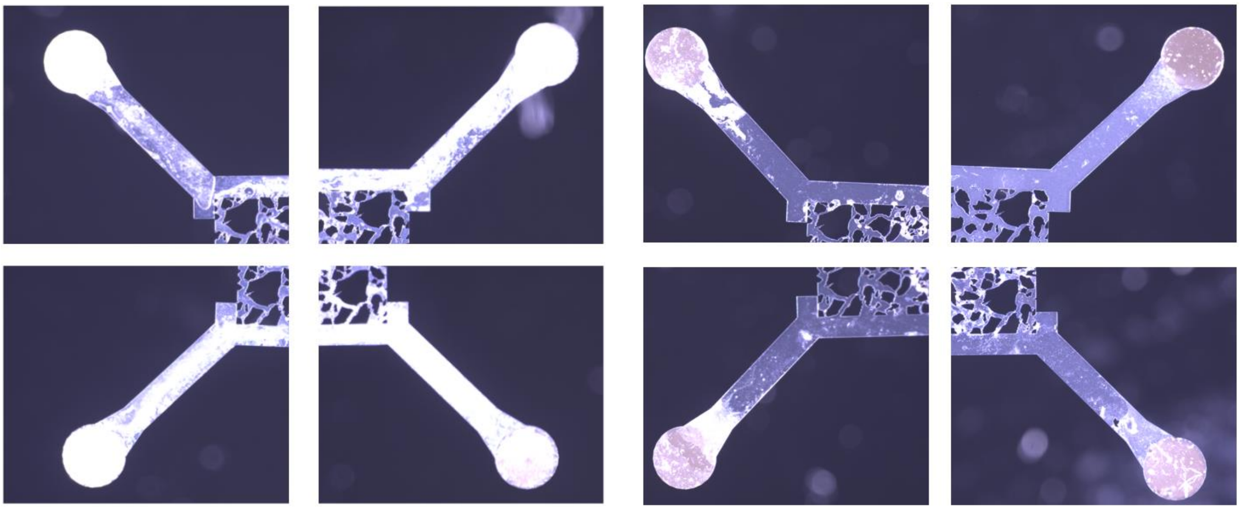

Figure 72: Image of the four ports after reactant injection (left), and after emerging it for one week in the acid (right). These two images are not from the same micromodel, but they illustrate how the calcite can be dissolved in the ports. The ports was fully plugged, and acid could not be injected inside the pore space to dissolve calcite. In order to dissolve the calcite in the ports, the micromodel was emerged in acid for one week.

After removal of bacteria from the top part and the top channel by circulating growth medium, calcite could be precipitated inside the pore space (Figure 73). The calcite did not precipitate evenly in the micromodel. Bacteria and reactant were injected from the top right port, therefore a high amount of calcite precipitated in the top and the right part of the micromodel, with less amount precipitating in the other parts of the micromodel. For better distribution, bacteria should be injected with a higher rate than 5.7 $\mu l/min$.

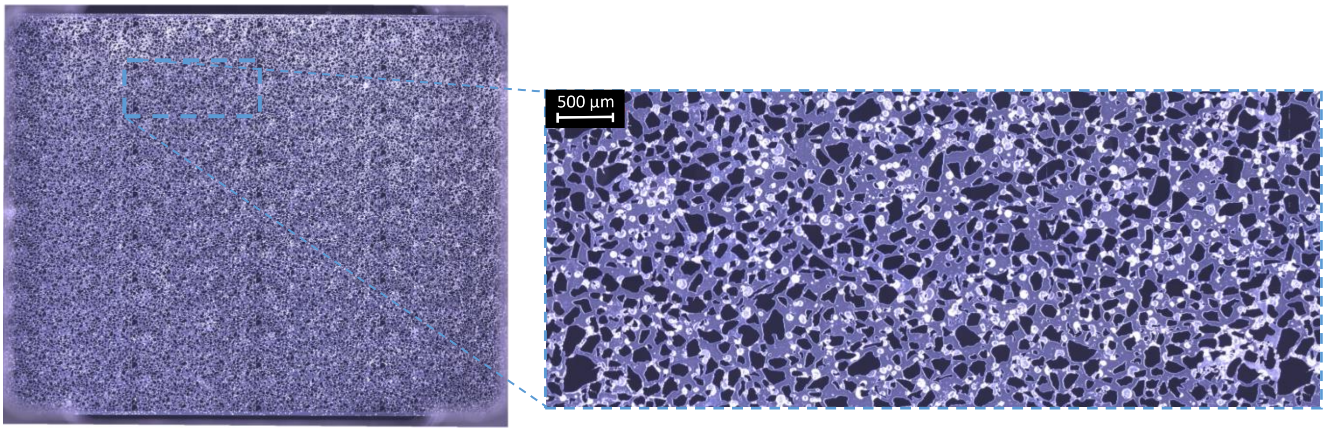

Figure 73: Calcite precipitation in a micromodel saturated with bacteria and growth medium at room temperature and atmospheric pressure. The reactant was injected with a constant rate of 5.7 μl/min from the top right port while producing through the two ports in the bottom.

16. Calcite Dissolution

Due to time restrictions, and lack of essential laboratory equipment such as a PEEK accumulator to saturate the hydrochloric acid with CO_2, the CO_2 saturated hydrochloric acid injection to the micromodel at high pressure was not conducted in this thesis. Instead 2 wt% hydrochloric acid was injected at atmospheric pressure (Figure 74). Significant amount of CO_2 was released during calcite dissolution, resulting in retarded calcite dissolution rates in the left bottom side: the CO_2 was trapped in this area and restricted the hydrochloric acid from direct contact with the calcite. After 11.4 ml of the 2 wt% hydrochloric acid injected, the CO_2 in the bottom left side started to circulate and the calcite in this location started to dissolve with a higher rate.

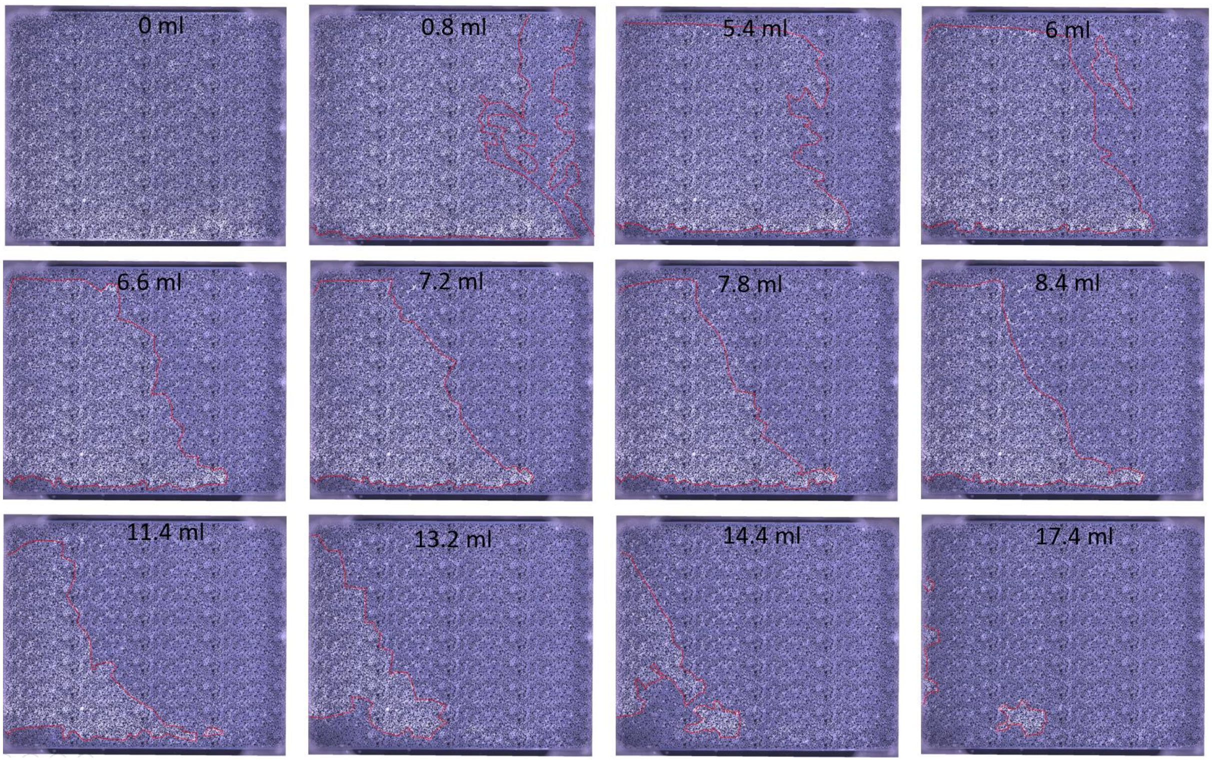

Figure 74: Calcite was dissolved by injecting 2 wt% hydrochloric acid at 5 $\mu l/min$ from the two ports in the bottom and producing through the two ports in the top. The calcite is indicated by the red polygons, while the black values indicating the amount of the 2 wt% hydrochloric acid injected.

Part IV: Conclusion and Future Work

17. Conclusions

This thesis reports experimental results on the foam behavior and CO_2 storage at pore scale, and a software development for pore scale image analysis. Important parameters like foam generation and foam decay were investigated at the pore scale using the software developed. The following key observations and conclusions can be drawn from this experimental study:

- The software developed has made it possible to analyze the foam behavior at pore-scale quantitatively by analyzing the NB instead of only describing the bubble texture. The combined and separated use of nanoparticles and surfactants as foaming agents were investigated by quantifying NB in the pore space during CO_2 injection using the software. The pore space was analyzed using the *Pore Throat Analysis* and *Pore Throat Classification* tools and the pore throats was located to study the interaction between bubble shape, orientation and distribution. In addition the *Bubble Analysis* tool was developed to describe each bubble by the surrounding pore throats and grains. Developed tools like *Bubble Analysis*, *Pore Throat Analysis*, and *Pore Throat Classification* tools were not applied on experimental results presented in the thesis, but will be valuable in future work.

- The porosity of the micromodel was calculated by image analysis and quantified to be 0.607 $\pm$ 0.001. The absolute permeability of the micromodel was quantified to be 2.97 $\pm$ 0.07 D.

- Surfactants demonstrated stronger foam (higher NB) compared to baseline, both quantitatively and qualitatively. Quantitatively, the number of bubbles increased significantly with the presence of surfactants, indicating a high CO_2 mobility reduction. An increase in surfactant concentration (from 0.05 wt% to 0.5 wt%) resulted in an increase in the number of bubbles and further mobility reduction. The foam was *shear thickening* when increasing the injection rate (from 1 $\mu l/min$ to 4 $\mu l/min$).

- A comparison between surfactant- and nanoparticle-stabilized foams was performed in this thesis by analyzing the number of the bubbles at pore-scale. Results indicate that surfactants have a higher ability to generate foams, whereas nanoparticles display a significant potential to stabilize foams. A synergy between nanoparticles and surfactant demonstrated that foam generation and stability do not depend on nanoparticles concentration in the absence of oil.

- A procedure for using of *Sporosarcina pasteurii* bacteria was developed as part of this thesis, and the calcite successfully precipitated in the pore space and calcite dissolution was studied at room temperature using 2 wt% hydrochloric acid. The procedure must be further developed to achieve a uniform distribution of calcite in the pore space to allow for controlled experiments related to the dissolution of calcite during CO_2 storage in carbonate.

18. Future Work

The experimental work presented in this thesis was a part of two ongoing projects run by the Reservoir Physics group at the Department of Physics and Technology, University of Bergen. In this thesis, a study of CO_2 foam and CO_2 storage at pore-scale were performed. However, there are further experiments and improvement that should be investigated going forward. Below is a list of suggestions for future work:

- Acquisition of a picture of the entire model (consists of 121 small pictures stitched together) required 72 seconds, thus a lot of dynamic information is lost between images. This should be improved by focusing on a smaller field of view, or decreasing the zoom and resolution to get the full view of the micromodel with less time. A key point is to balance acquisition time and resolution needed to perform a good image threshold.

- The system dead volume should be reduced because of the small pore volume in the micromodel (11.22 μl). This is an ongoing improvement in the Reservoir Physics group, where the autoclave valve will be replaced by a valve with a significant less dead volume.

- For a better evaluation of foaming agents at pore-scale, oil should be introduced to the system to study the foam-oil interaction for nanoparticles and surfactants at pore-scale in the future. Other effects that should be investigated at pore-scale for better evaluation of foaming agents are temperature, salinity, and pH.

- As mentioned, the activation of the bacteria inside the micromodel was not fully developed during this thesis. The calcite should be evenly distributed in the pore space, and this can be done by injecting the bacteria by a higher injecting rate. Parameters like bacteria concentration and growth medium concentration should also be investigated to develop a fully procedure for calcite precipitation.

- The dissolution of calcite using CO_2 saturated hydrochloric acid injection into the micromodel at high pressure should be conducted in the future to study the engulfment phenomenon described by (Song et al., 2018).

- The thresholding of the foam generation period should be enhanced and hierarchy method should be avoided to get a better accuracy.

- A method to threshold the calcite dissolution images, and distinguish between calcite and CO_2 bubbles should be developed to obtain an accurate calcite dissolution rate.

Part V: Appendix

Nomenclature

%	Percent
°C	Celsius degree
ρ	Density
ϕ	Effective porosity
ϕ_A	Absolute porosity
ϕ_{res}	Residual porosity
ϕ_{tot}	Total porosity
ΔP	Differential pressure
A	Cross sectional area
A_i	Area of grain i
D	Darcy
K	Absolute permeability
K_i	The effective permeability of fluid i
K_{ri}	Relative permeability of fluid i
M	Molar
Mt	Million tons
PV	Pore volume
Q	Volumetric flow
S	Standard deviation
S_i	Saturation of fluid i
TW	Terawatts
V_p	The pore volume
V_t	The matrix volume
Y	Height of the picture
$\frac{\mathrm{dp}}{\mathrm{dl}}$	Pressure Drop across Sample
g	The gravity constant
l	Length
p	Pressure
ppm	parts per million

v	Velocity
wt%	weight percent
x	Width of the picture
z	Height
μ	Viscosity
ß	Forchheimer factor

Abbreviations

2D	Two Dimensional
4D	Four Dimensional
BPIPV	Bubbles per Injected Pore Volume
BPR	Back Pressure Regulator
CCS	Carbon Capture and Storage
CCU	Carbon Capture and Utilization
CCUS	Carbon Capture, Utilization and Storage
$CO(NH_2)_2$	Urea
CO_2	Carbon dioxide
$\mathrm{CO_3^{2-}}$	Carbonate Ion
$\mathrm{C_6H_{12}O_6}$	Glucose
$\mathrm{CaCO_3}$	Calcium Carbonate
$\mathrm{Ca^{2+}}$	Calcium Ion
EOR	Enhanced Oil Recovery
Gb	Gigabyte
$\mathrm{HCO_3^-}$	Bicarbonate Ion
HMDS	Hexamethyldisilane
HSE	Health, Safety, and Environment
$\mathrm{H_2CO_3}$	Carbonic Acid
$\mathrm{H_2O}$	Water
IFT	Interfacial tension
Mb	Megabyte
MMP	Minimum Miscibility Pressure
NB	Number of Bubbles
NBPIPV	Normalized Bubbles per Injected Pore Volume
NH_3	Ammonia
$\mathrm{NH_4^+}$	Ammonium Ion
NPD	The Norwegian Petroleum Directorate
O_2	Oxygen

OH^-	Hydroxide Ion
PEEK	Polyether Ether Ketone
PET	Positron Emission Tomography
POM	Polyoxymethylene
SAG	Surfactant Alternating Gas
Tb	Terabyte

Tables

Table 7: Calculated values of the porosity.

Percentage of the micromodel	*Porosity*
0.1111	0.6050
0.2500	0.6036
0.3600	0.5997
0.4444	0.6014
0.5102	0.6030
0.5625	0.6039
0.6049	0.6044
0.6400	0.6055
0.6694	0.6057
0.6944	0.6051
0.7160	0.6059
0.7347	0.6067
0.7511	0.6067
0.7656	0.6061
0.7785	0.6064
0.7901	0.6065
0.8006	0.6065
0.8100	0.6070
0.8186	0.6072
0.8264	0.6075
0.8336	0.6076
0.8403	0.6075
0.8464	0.6075
0.8521	0.6076
0.8573	0.6075
0.8622	0.6076
0.8668	0.6077
0.8711	0.6078
0.8751	0.6078
0.8789	0.6077
0.8825	0.6076
0.8858	0.6074
0.8890	0.6073
0.8920	0.6072
0.8948	0.6072
0.8975	0.6073
0.9001	0.6073
0.9025	0.6074
0.9048	0.6074
0.9070	0.6074
0.9091	0.6074
0.9112	0.6074
0.9131	0.6074
0.9149	0.6073
0.9167	0.6073
0.9184	0.6072
0.9200	0.6072
0.9216	0.6072
0.9231	0.6072
0.9246	0.6072
0.9260	0.6072
0.9273	0.6073
0.9286	0.6073
0.9298	0.6072
0.9311	0.6072
0.9322	0.6072
0.9334	0.6072
0.9344	0.6072
0.9355	0.6072
0.9365	0.6072
0.9375	0.6072
0.9385	0.6072
0.9394	0.6072
0.9403	0.6071
0.9412	0.6071
0.9420	0.6071
0.9429	0.6071
0.9437	0.6071
0.9445	0.6071
0.9452	0.6071
0.9460	0.6071
0.9467	0.6071
0.9474	0.6070
0.9481	0.6070
0.9487	0.6070
0.9494	0.6070
0.9500	0.6070
0.9506	0.6070
0.9512	0.6070
0.9518	0.6069
0.9524	0.6069
0.9529	0.6069
0.9535	0.6069
0.9540	0.6069
0.9546	0.6068
0.9551	0.6068
0.9556	0.6068
0.9560	0.6068
0.9565	0.6068
0.9570	0.6067
0.9575	0.6067
0.9579	0.6067
0.9583	0.6067
0.9588	0.6067
0.9592	0.6067
0.9596	0.6067
0.9600	0.6067
0.9604	0.6066
0.9608	0.6066
0.9612	0.6066

Table 8: NB values for the three size categories for BL1.

PV	*< 10^3 µm²*	*10^3-10^4 µm²*	*> 10^4 µm²*
0	499	434	131
0.43	624	515	149
0.86	583	500	148
1.28	612	518	151
1.71	691	596	192
2.14	757	605	188
2.57	622	496	160
3	693	560	182
3.42	675	514	161
3.85	795	590	191
4.28	787	582	184
4.71	697	549	181
5.14	731	544	176
5.56	786	594	207
5.99	860	617	211
6.42	887	645	207
6.85	889	679	216
7.28	942	712	234
7.7	992	750	256
8.13	1000	750	244
8.56	1018	769	256
8.99	1014	770	260
9.42	1048	779	258
9.84	1005	761	264
10.27	878	683	228
10.7	881	673	227
11.13	812	618	205
11.56	825	630	209
11.98	831	623	198
12.41	899	624	219
12.84	892	654	217
13.27	929	680	225
13.7	946	680	235
14.12	949	699	234
14.55	990	716	243
14.98	985	719	237
15.41	996	720	249
15.84	1030	738	246
16.26	1046	786	259
16.69	1035	768	264
17.12	1015	771	258
17.55	1060	764	269
17.98	1142	831	291
18.4	1020	756	255
18.83	1057	769	258
19.26	1059	771	265
19.69	1059	787	256
20.12	1064	798	267
20.54	1080	815	277
20.97	1095	803	279
21.4	1111	813	277
21.83	1127	824	275
22.26	1110	843	282
22.68	1111	823	277
23.11	1106	822	275
23.54	1113	823	282
23.97	1154	828	288
24.4	1179	866	308
24.82	1155	855	295
25.25	1180	850	311
25.68	1280	909	324
26.11	1228	918	330
26.54	1165	863	299
26.96	1164	835	299
27.39	1157	854	294
27.82	1158	858	306
28.25	1183	868	312
28.68	1206	921	304
29.1	1213	891	305
29.53	1203	883	308
29.96	1348	974	349
30.39	1258	893	307
30.82	1401	952	347
31.24	1387	978	350
31.67	1347	985	339
32.1	1358	1005	357
32.53	1350	974	333
32.96	1415	994	346
33.38	1296	920	318
33.81	1426	1023	348
34.24	1289	926	325
34.67	1297	954	341
35.1	1404	1019	353
35.52	1413	1011	355
35.95	1405	1028	356
36.38	1439	1026	358
36.81	1403	1034	360
37.24	1428	1011	353
37.66	1417	1040	352

38.09	1439	1036	350
38.52	1265	925	322
38.95	1368	1006	351
39.38	1377	987	353
39.8	1393	1001	350
40.23	1404	1016	347
40.66	1396	1024	356
41.09	1410	1020	356
41.52	1457	1041	370
41.94	1413	1006	360
42.37	1430	1035	363
42.8	1421	1018	358
43.23	1410	1004	355
43.66	1444	1027	369
44.08	1385	1015	358
44.51	1561	1068	389
44.94	1568	1093	386
45.37	1541	1095	381
45.8	1531	1082	399
46.22	1542	1081	407
46.65	1544	1071	412
47.08	1587	1075	408
47.51	1592	1130	416
47.94	1563	1098	396
48.36	1578	1086	397
48.79	1595	1082	404
49.22	1601	1098	402
49.65	1657	1144	421
50.08	1654	1169	421
50.5	1645	1172	422
50.93	1544	1104	369
51.36	1519	1072	376
51.79	1500	1072	372
52.22	1530	1088	379
52.64	1589	1125	384

53.07	1543	1116	378
53.5	1569	1117	378
53.93	1543	1113	383
54.36	1543	1115	380
54.78	1572	1127	375
55.21	1531	1119	370
55.64	1542	1066	371
56.07	1526	1131	374
56.5	1512	1080	371
56.92	1602	1134	368
57.35	1626	1190	379
57.78	1638	1186	380
58.21	1676	1203	381
58.64	1584	1172	371
59.06	1578	1199	380
59.49	1606	1183	366
59.92	1607	1138	375
60.35	1574	1171	372
60.78	1596	1215	374
61.2	1588	1183	371
61.63	1565	1175	377
62.06	1663	1187	378
62.49	1632	1197	379
62.92	1688	1213	385
63.34	1622	1215	387
63.77	1576	1176	379
64.2	1684	1249	393
64.63	1606	1200	374
65.06	1702	1267	389
65.48	1703	1268	404
65.91	1671	1267	392
66.34	1644	1244	392
66.77	1706	1262	404
67.2	1626	1245	391
67.62	1712	1267	386

Table 9: NB values for the three size categories for AQ1.

PV	*< 10^3 µm²*	*10^3-10^4 µm²*	*> 10^4 µm²*
0	0.51	0.46	0.31
0.43	1.08	0.67	0.64
0.86	1.56	0.76	0.52
1.28	1.61	0.83	0.54
1.71	1.36	0.75	0.39
2.14	1.14	0.74	0.41
2.57	1.40	0.89	0.58
3	4.14	2.54	2.94
3.42	5.53	2.57	2.53
3.85	5.56	2.52	1.81
4.28	6.03	2.67	1.79
4.71	7.09	2.99	1.70
5.14	7.03	3.07	1.68
5.56	6.75	2.90	1.53
5.99	6.37	3.19	1.86
6.42	6.46	3.20	1.91
6.85	6.65	3.36	1.94
7.28	6.54	3.41	2.01
7.7	6.47	3.43	2.07
8.13	6.48	3.60	2.12
8.56	6.46	3.87	2.94
8.99	6.39	4.31	4.15
9.42	6.17	4.54	4.54
9.84	6.35	4.72	4.45
10.27	7.16	5.36	5.59
10.7	6.60	5.38	6.23
11.13	7.05	5.90	7.01
11.56	6.80	5.82	6.79
11.98	6.82	5.99	7.35
12.41	6.38	6.20	6.90
12.84	6.39	5.99	7.41
13.27	5.90	5.81	7.30
13.7	5.81	5.81	7.14
14.12	5.65	5.47	7.32
14.55	5.81	7.53	8.95
14.98	5.62	7.47	9.37
15.41	5.24	7.39	9.07
15.84	5.05	7.38	9.20
16.26	4.85	6.85	8.88
16.69	4.81	7.01	8.84
17.12	4.90	6.97	9.19
17.55	4.56	7.05	8.84
17.98	4.43	6.68	8.16
18.4	4.91	7.43	9.48
18.83	4.74	7.31	9.51
19.26	4.64	7.39	9.33
19.69	4.51	7.23	9.98
20.12	4.38	7.13	9.47
20.54	5.32	9.49	9.11
20.97	5.77	11.62	9.36
21.4	5.44	11.56	9.36
21.83	5.41	11.50	9.53
22.26	5.36	11.31	9.36
22.68	5.34	11.58	9.66
23.11	5.30	11.68	9.71
23.54	5.20	11.66	9.42
23.97	5.05	11.54	9.41
24.4	4.95	11.03	8.95
24.82	5.12	11.11	9.40
25.25	5.10	11.21	8.97
25.68	4.72	10.57	8.62
26.11	4.98	10.46	8.50
26.54	5.86	12.51	8.83
26.96	6.12	14.30	9.17
27.39	6.82	15.48	9.44
27.82	6.95	15.85	8.79
28.25	6.81	15.68	8.77
28.68	6.70	14.82	9.04
29.1	6.59	15.32	8.97
29.53	6.67	15.36	8.93
29.96	5.96	13.84	7.92
30.39	6.41	15.18	9.01
30.82	5.75	14.16	7.99
31.24	5.84	13.77	7.96
31.67	6.01	13.66	8.16
32.1	6.09	13.54	7.68
32.53	6.25	14.19	7.93
32.96	5.97	13.86	7.62
33.38	6.47	15.12	8.32
33.81	6.08	14.10	7.78
34.24	6.96	15.72	7.93
34.67	7.01	15.27	7.61
35.1	6.51	14.36	7.38
35.52	6.41	14.51	7.35
35.95	6.46	14.27	7.37
36.38	6.29	14.29	7.41
36.81	6.44	14.12	7.38
37.24	6.34	14.44	7.58
37.66	6.49	14.07	7.50

38.09	6.41	14.30	7.60
38.52	7.26	16.05	8.26
38.95	6.80	14.92	7.63
39.38	6.84	15.46	7.47
39.8	6.95	15.73	7.50
40.23	7.15	15.81	7.24
40.66	7.11	15.74	7.13
41.09	7.05	15.86	7.13
41.52	6.80	15.48	6.93
41.94	7.02	16.02	7.13
42.37	6.91	15.53	7.09
42.8	6.93	15.85	7.19
43.23	7.04	16.13	7.22
43.66	7.22	16.05	6.70
44.08	8.17	17.38	6.33
44.51	7.53	16.53	5.57
44.94	7.48	16.16	5.64
45.37	7.62	16.14	5.81
45.8	7.67	16.31	5.53
46.22	7.58	16.27	5.45
46.65	7.51	16.44	5.38
47.08	7.33	16.36	5.46
47.51	7.29	15.50	5.37
47.94	7.40	15.93	5.68
48.36	7.28	16.13	5.65
48.79	7.20	16.14	5.61
49.22	7.15	15.91	5.59
49.65	6.87	15.34	5.35
50.08	6.91	14.96	5.37
50.5	6.92	14.92	5.30
50.93	7.35	15.78	6.11
51.36	7.47	16.22	6.00
51.79	7.52	16.22	6.10
52.22	7.35	15.97	5.99
52.64	7.04	15.42	5.96
53.07	7.29	15.54	6.05
53.5	7.13	15.50	6.06
53.93	7.26	15.55	6.01
54.36	7.25	15.52	6.06
54.78	7.15	15.36	6.14
55.21	7.44	15.59	6.22
55.64	7.37	16.34	6.19
56.07	7.52	15.49	6.18
56.5	7.62	16.32	6.24
56.92	7.16	15.53	6.29
57.35	7.01	14.80	6.11
57.78	6.96	14.89	6.12
58.21	6.79	14.70	6.11
58.64	7.17	15.04	6.30
59.06	7.15	14.74	6.16
59.49	7.03	14.91	6.42
59.92	7.00	15.51	6.25
60.35	7.10	15.06	6.31
60.78	7.33	14.49	6.03
61.2	7.36	14.90	6.10
61.63	7.39	15.01	6.05
62.06	6.92	14.84	6.03
62.49	7.03	14.77	5.99
62.92	6.79	14.54	5.95
63.34	7.02	14.54	5.95
63.77	7.20	15.06	6.08
64.2	6.73	14.19	5.87
64.63	7.08	14.78	6.18
65.06	6.65	13.96	6.02
65.48	6.59	13.96	5.76
65.91	6.75	14.00	5.93
66.34	6.81	14.28	5.89
66.77	6.67	14.07	5.67
67.2	6.94	14.29	5.88
67.62	6.55	14.01	5.99

Table 10: NB values for the three size categories for AQ2.

PV	< 10^3 μm^2	10^3-10^4 μm^2	> 10^4 μm^2
0	6.06	5.44	6.23
0.43	8.21	10.32	11.48
0.86	12.95	17.97	11.93
1.28	20.06	25.73	9.81
1.71	26.55	28.31	6.49
2.14	27.21	30.64	6.36
2.57	38.77	39.81	6.73
3	41.44	37.13	5.24
3.42	53.27	39.74	5.16
3.85	53.68	31.79	3.91
4.28	65.87	25.18	3.07
4.71	79.74	25.89	2.74
5.14	78.48	30.19	2.61
5.56	72.19	30.38	2.35
5.99	64.84	31.02	2.38
6.42	61.75	30.90	2.50
6.85	60.53	30.50	2.44
7.28	56.03	30.20	2.28
7.7	52.27	29.59	2.13
8.13	50.79	30.35	2.25
8.56	48.90	30.42	2.13
8.99	48.08	31.04	2.14
9.42	45.58	31.40	2.18
9.84	46.67	32.72	2.19
10.27	52.25	37.08	2.54
10.7	51.01	38.16	2.63
11.13	54.27	42.17	3.00
11.56	52.45	41.96	2.94
11.98	51.02	42.97	3.18
12.41	46.18	43.58	2.93
12.84	45.67	41.92	2.97
13.27	43.07	40.73	2.90
13.7	41.58	41.06	2.88
14.12	40.72	40.30	2.85
14.55	38.45	39.52	2.79
14.98	37.91	39.64	2.90
15.41	36.98	39.80	2.81
15.84	35.23	38.92	2.88
16.26	34.01	36.75	2.75
16.69	33.81	37.84	2.70
17.12	33.99	37.80	2.81
17.55	32.05	38.26	2.75
17.98	29.29	35.24	2.55
18.4	32.19	38.94	2.96
18.83	30.71	38.27	2.99
19.26	30.16	38.27	2.91
19.69	29.68	37.56	3.07
20.12	29.15	37.12	2.97
20.54	28.96	36.00	2.89
20.97	28.90	36.72	2.75
21.4	27.96	36.39	2.82
21.83	27.05	35.99	2.87
22.26	26.97	35.29	2.80
22.68	26.49	36.17	2.93
23.11	26.15	36.32	2.97
23.54	25.62	36.19	2.94
23.97	24.40	36.03	2.92
24.4	23.54	34.47	2.76
24.82	23.75	34.93	3.00
25.25	22.91	35.12	2.87
25.68	20.92	32.82	2.78
26.11	21.56	32.45	2.76
26.54	22.45	34.60	3.06
26.96	22.10	35.73	3.11
27.39	22.04	34.92	3.18
27.82	21.73	34.73	3.11
28.25	21.04	34.25	3.07
28.68	20.49	32.31	3.19
29.1	20.15	33.33	3.22
29.53	20.12	33.63	3.22
29.96	17.77	30.46	2.89
30.39	18.79	33.15	3.35
30.82	16.76	31.05	2.97
31.24	16.75	30.18	2.95
31.67	17.13	29.88	3.13
32.1	16.79	29.32	3.00
32.53	16.69	30.23	3.21
32.96	15.81	29.63	3.13
33.38	17.09	31.94	3.48
33.81	15.41	28.68	3.21
34.24	17.16	31.76	3.45
34.67	17.80	31.07	3.33
35.1	17.60	27.00	2.91
35.52	22.56	26.07	2.27
35.95	26.42	24.93	1.91
36.38	25.15	25.78	1.84
36.81	24.69	26.12	1.86
37.24	23.47	27.25	1.94
37.66	22.94	26.83	1.99

38.09	21.92	27.26	2.04
38.52	24.32	30.77	2.28
38.95	21.96	28.47	2.10
39.38	21.33	29.14	2.09
39.8	20.51	28.89	2.16
40.23	20.00	28.53	2.23
40.66	19.63	28.35	2.22
41.09	19.07	28.57	2.25
41.52	18.13	28.08	2.22
41.94	18.31	29.08	2.30
42.37	17.84	28.26	2.32
42.8	17.67	28.80	2.35
43.23	17.51	29.15	2.45
43.66	16.83	28.52	2.38
44.08	17.26	28.84	2.50
44.51	15.10	27.35	2.35
44.94	14.80	26.67	2.45
45.37	14.87	26.66	2.50
45.8	14.77	26.96	2.40
46.22	14.47	26.97	2.40
46.65	14.21	27.18	2.43
47.08	13.67	27.11	2.43
47.51	13.46	25.71	2.44
47.94	13.53	26.44	2.62
48.36	13.26	26.69	2.64
48.79	12.99	26.67	2.63
49.22	12.81	26.33	2.71
49.65	12.22	25.21	2.60
50.08	12.14	24.64	2.63
50.5	12.08	24.56	2.65
50.93	12.71	26.04	3.05
51.36	12.78	26.74	3.03
51.79	12.81	26.70	3.13
52.22	12.42	26.28	3.09
52.64	11.86	25.32	3.10
53.07	12.10	25.43	3.20
53.5	11.79	25.43	3.26
53.93	11.91	25.50	3.27
54.36	11.81	25.41	3.33
54.78	11.50	25.10	3.41
55.21	11.70	25.25	3.52
55.64	11.52	26.44	3.55
56.07	11.59	24.86	3.52
56.5	11.62	26.02	3.54
56.92	10.82	24.63	3.69
57.35	10.63	23.44	3.62
57.78	10.49	23.50	3.66
58.21	10.20	23.10	3.66
58.64	10.69	23.70	3.77
59.06	10.71	23.16	3.74
59.49	10.40	23.38	3.92
59.92	10.37	24.26	3.86
60.35	10.53	23.50	3.95
60.78	10.30	22.64	3.93
61.2	10.25	23.09	4.04
61.63	10.37	23.28	4.03
62.06	9.75	22.97	4.05
62.49	9.84	22.79	4.06
62.92	9.47	22.45	4.05
63.34	9.78	22.37	4.10
63.77	10.00	23.03	4.20
64.2	9.34	21.67	4.07
64.63	9.73	22.51	4.30
65.06	9.09	21.20	4.22
65.48	9.05	21.20	4.06
65.91	9.22	21.22	4.19
66.34	9.33	21.58	4.21
66.77	8.97	21.20	4.15
67.2	9.48	21.45	4.32
67.62	8.93	21.07	4.37

Table 11: NB values for the three size categories for AQ3.

PV	*< 10^3 μm^2*	*10^3-10^4 μm^2*	*> 10^4 μm^2*
0	6.77	3.57	3.71
0.43	6.70	3.82	3.54
0.86	8.02	4.47	3.87
1.28	8.14	4.73	4.05
1.71	7.71	4.45	3.37
2.14	7.57	4.95	4.69
2.57	9.33	6.16	5.85
3	9.08	6.04	6.14
3.42	9.72	7.55	7.78
3.85	8.21	6.94	7.23
4.28	9.04	8.62	8.54
4.71	11.20	10.34	9.25
5.14	12.02	12.26	10.35
5.56	12.35	13.56	9.42
5.99	10.93	13.40	10.04
6.42	10.30	12.94	10.40
6.85	10.49	12.48	9.50
7.28	9.68	11.87	8.99
7.7	9.30	11.42	8.32
8.13	9.36	11.48	8.69
8.56	10.14	12.18	7.33
8.99	13.18	16.65	4.57
9.42	13.40	17.30	4.88
9.84	14.23	18.17	4.88
10.27	16.48	20.58	5.75
10.7	16.41	21.22	5.89
11.13	18.11	23.57	6.81
11.56	17.91	23.29	6.82
11.98	18.45	25.07	7.49
12.41	17.22	25.20	6.78
12.84	17.42	24.09	6.82
13.27	18.76	24.52	5.00
13.7	19.11	24.78	4.81
14.12	19.10	24.30	4.87
14.55	18.33	23.91	4.67
14.98	18.36	24.06	4.81
15.41	18.21	24.28	4.69
15.84	17.68	23.85	4.93
16.26	17.48	22.67	4.76
16.69	19.08	24.57	4.30
17.12	20.07	24.93	4.47
17.55	19.25	25.17	4.23
17.98	17.91	23.08	3.96
18.4	20.10	25.39	4.60
18.83	19.94	25.30	4.43
19.26	22.46	25.07	2.85
19.69	23.13	24.85	2.86
20.12	23.18	25.05	2.84
20.54	22.86	24.90	2.88
20.97	22.63	25.66	2.89
21.4	22.26	25.59	3.04
21.83	21.94	25.43	3.15
22.26	22.25	24.96	3.16
22.68	22.31	25.75	3.26
23.11	22.36	25.85	3.35
23.54	22.29	25.90	3.32
23.97	21.85	26.23	3.27
24.4	24.59	26.17	2.09
24.82	24.93	26.82	2.29
25.25	24.37	27.13	2.23
25.68	22.44	25.42	2.18
26.11	23.31	25.28	2.14
26.54	24.53	26.90	2.45
26.96	24.67	28.03	2.54
27.39	25.00	27.56	2.53
27.82	25.23	27.38	2.47
28.25	24.74	26.89	2.38
28.68	24.19	25.41	2.45
29.1	23.98	26.29	2.46
29.53	24.08	26.62	2.42
29.96	21.43	24.20	2.12
30.39	22.93	26.44	2.44
30.82	20.52	24.85	2.19
31.24	20.70	24.16	2.20
31.67	21.30	24.03	2.32
32.1	21.09	23.60	2.20
32.53	21.22	24.32	2.39
32.96	20.20	23.88	2.34
33.38	21.98	25.86	2.56
33.81	19.95	23.30	2.34
34.24	21.99	25.81	2.54
34.67	21.85	25.13	2.47
35.1	20.10	23.62	2.41
35.52	19.96	23.79	2.43
35.95	20.05	23.40	2.42
36.38	19.52	23.46	2.43
36.81	20.00	23.30	2.41
37.24	19.62	23.85	2.46
37.66	19.74	23.21	2.49

38.09	19.42	23.36	2.52
38.52	22.01	26.24	2.73
38.95	20.33	24.11	2.49
39.38	20.21	24.60	2.55
39.8	19.84	24.34	2.55
40.23	19.65	24.00	2.60
40.66	19.77	23.78	2.54
41.09	19.48	23.96	2.54
41.52	18.83	23.49	2.45
41.94	19.33	24.30	2.54
42.37	19.11	23.62	2.54
42.8	19.19	24.06	2.58
43.23	19.28	24.45	2.62
43.66	18.80	23.87	2.53
44.08	19.54	24.22	2.63
44.51	17.28	23.05	2.47
44.94	17.21	22.48	2.51
45.37	17.45	22.45	2.53
45.8	17.56	22.71	2.44
46.22	17.39	22.79	2.41
46.65	17.36	23.02	2.38
47.08	16.81	22.98	2.43
47.51	16.79	21.92	2.38
47.94	17.02	22.56	2.54
48.36	16.87	22.82	2.53
48.79	16.61	22.98	2.51
49.22	16.57	22.63	2.53
49.65	15.97	21.73	2.44
50.08	15.90	21.31	2.47
50.5	15.99	21.24	2.45
50.93	17.03	22.51	2.81
51.36	17.22	23.24	2.80
51.79	17.45	23.24	2.80
52.22	17.05	22.93	2.72
52.64	16.39	22.17	2.72

53.07	16.86	22.38	2.79
53.5	16.54	22.38	2.82
53.93	16.80	22.51	2.78
54.36	16.75	22.52	2.78
54.78	16.53	22.32	2.82
55.21	17.10	22.43	2.77
55.64	16.95	23.71	2.78
56.07	17.09	22.40	2.78
56.5	17.22	23.52	2.82
56.92	16.22	22.39	2.88
57.35	15.96	21.35	2.77
57.78	15.78	21.44	2.80
58.21	15.37	21.14	2.76
58.64	16.28	21.74	2.85
59.06	16.27	21.27	2.82
59.49	16.00	21.57	2.90
59.92	16.03	22.46	2.81
60.35	16.30	21.86	2.83
60.78	16.06	21.10	2.85
61.2	16.07	21.65	2.89
61.63	16.30	21.80	2.87
62.06	15.27	21.59	2.88
62.49	15.56	21.41	2.85
62.92	15.02	21.14	2.86
63.34	15.56	21.11	2.87
63.77	16.07	21.90	2.87
64.2	14.99	20.72	2.65
64.63	15.96	21.64	2.58
65.06	15.27	20.25	2.46
65.48	15.22	19.65	2.28
65.91	15.91	19.41	2.27
66.34	16.16	19.82	2.27
66.77	15.50	19.61	2.21
67.2	16.19	19.92	2.30
67.62	15.33	19.63	2.31

Table 12: NB values for the three size categories for AQ4.

PV	*< 10^3 µm²*	*10^3-10^4 µm²*	*> 10^4 µm²*
0	3.97	3.67	4.00
0.43	4.78	3.69	3.85
0.86	6.85	4.90	4.76
1.28	8.91	11.07	15.17
1.71	11.84	17.88	11.59
2.14	15.44	23.70	10.54
2.57	26.41	33.54	9.98
3	32.04	34.06	6.44
3.42	32.50	39.75	7.35
3.85	29.59	34.47	6.59
4.28	32.75	35.57	6.33
4.71	40.62	38.26	5.86
5.14	45.81	36.34	5.63
5.56	56.26	29.91	3.41
5.99	55.39	25.69	3.29
6.42	59.05	25.09	2.64
6.85	58.33	27.56	2.56
7.28	53.39	28.49	2.44
7.7	48.96	28.60	2.34
8.13	47.20	29.88	2.50
8.56	45.16	30.05	2.50
8.99	44.24	30.71	2.50
9.42	43.14	30.45	2.56
9.84	43.61	32.48	2.57
10.27	48.45	37.22	3.06
10.7	47.02	38.56	3.12
11.13	49.79	42.75	3.53
11.56	47.72	42.68	3.55
11.98	46.26	43.63	3.83
12.41	41.71	44.12	3.51
12.84	41.07	42.51	3.64
13.27	38.66	40.95	3.60
13.7	37.11	41.39	3.56
14.12	36.25	40.67	3.62
14.55	34.05	39.89	3.59
14.98	33.55	39.97	3.69
15.41	32.52	40.05	3.55
15.84	30.85	39.28	3.67
16.26	29.88	37.02	3.55
16.69	29.58	38.00	3.59
17.12	29.64	37.90	3.73
17.55	27.89	38.39	3.61
17.98	25.49	35.38	3.44
18.4	28.06	38.97	3.95
18.83	26.61	38.28	4.02
19.26	26.13	38.41	3.98
19.69	25.79	37.54	4.13
20.12	25.27	37.06	4.06
20.54	24.48	36.33	3.96
20.97	23.77	36.90	3.95
21.4	23.10	36.44	4.03
21.83	22.47	35.90	4.19
22.26	22.48	35.18	4.09
22.68	22.14	36.09	4.25
23.11	22.00	36.09	4.30
23.54	21.51	36.09	4.26
23.97	20.51	35.75	4.26
24.4	19.86	34.21	4.01
24.82	20.07	34.55	4.22
25.25	19.42	34.69	4.06
25.68	17.71	32.50	3.93
26.11	18.21	32.18	3.94
26.54	19.03	34.18	4.33
26.96	18.87	35.31	4.49
27.39	18.73	34.50	4.56
27.82	18.50	34.32	4.45
28.25	17.93	33.79	4.38
28.68	17.46	31.82	4.56
29.1	17.15	32.81	4.54
29.53	17.18	33.03	4.57
29.96	15.14	29.91	4.09
30.39	16.18	32.63	4.70
30.82	14.35	30.58	4.18
31.24	14.32	29.71	4.21
31.67	14.65	29.49	4.35
32.1	14.40	28.87	4.18
32.53	14.43	29.68	4.54
32.96	13.60	29.07	4.36
33.38	14.73	31.31	4.85
33.81	13.23	28.06	4.49
34.24	14.46	30.96	4.83
34.67	14.35	30.00	4.67
35.1	13.13	28.04	4.54
35.52	12.95	28.32	4.52
35.95	12.98	27.85	4.56
36.38	12.63	27.81	4.56
36.81	12.80	27.56	4.62
37.24	12.51	28.12	4.73
37.66	12.46	27.13	4.88

38.09	12.17	27.10	4.94
38.52	13.71	30.28	5.45
38.95	12.57	27.71	5.07
39.38	12.40	28.34	5.08
39.8	12.34	28.04	5.08
40.23	12.21	27.55	5.22
40.66	12.83	26.82	4.92
41.09	16.74	26.86	3.57
41.52	16.12	26.76	3.37
41.94	16.19	27.85	3.52
42.37	15.60	27.13	3.57
42.8	15.38	27.59	3.63
43.23	15.16	27.98	3.75
43.66	14.50	27.42	3.68
44.08	14.81	27.74	3.85
44.51	12.90	26.34	3.61
44.94	12.67	25.75	3.62
45.37	12.76	25.66	3.72
45.8	12.66	25.89	3.53
46.22	12.39	25.87	3.50
46.65	12.19	26.07	3.55
47.08	11.69	25.95	3.62
47.51	11.51	24.62	3.57
47.94	11.56	25.29	3.79
48.36	11.34	25.51	3.88
48.79	11.11	25.54	3.82
49.22	10.93	25.13	3.88
49.65	10.46	24.06	3.72
50.08	10.34	23.52	3.76
50.5	10.31	23.39	3.81
50.93	10.89	24.79	4.36
51.36	10.98	25.46	4.36
51.79	11.04	25.42	4.38
52.22	10.74	24.99	4.33
52.64	10.23	24.10	4.32
53.07	10.44	24.22	4.42
53.5	10.16	24.15	4.45
53.93	10.25	24.21	4.45
54.36	10.18	24.13	4.53
54.78	9.89	23.87	4.57
55.21	10.09	23.91	4.70
55.64	9.93	25.12	4.69
56.07	9.97	23.59	4.71
56.5	10.04	24.68	4.75
56.92	9.41	23.40	4.87
57.35	9.17	22.31	4.81
57.78	9.04	22.34	4.79
58.21	8.78	21.94	4.83
58.64	9.25	22.49	5.01
59.06	9.19	21.95	4.87
59.49	8.98	22.22	5.14
59.92	8.95	23.05	5.05
60.35	9.09	22.33	5.16
60.78	8.92	21.50	5.09
61.2	9.63	21.21	4.91
61.63	16.51	19.81	3.16
62.06	23.12	19.92	2.01
62.49	22.39	20.88	1.94
62.92	20.62	21.20	1.95
63.34	20.56	21.62	1.99
63.77	20.44	22.59	2.11
64.2	18.51	21.52	2.04
64.63	18.83	22.64	2.19
65.06	17.19	21.64	2.14
65.48	16.69	21.79	2.10
65.91	16.63	21.96	2.20
66.34	16.49	22.48	2.28
66.77	15.55	22.19	2.23
67.2	15.90	22.60	2.38
67.62	14.78	22.24	2.43

Table 13: NB values for the three size categories for AQ5.

PV	*< 10^3 μm²*	*10^3-10^4 μm²*	*> 10^4 μm²*
0	0.39	0.43	0.30
0.43	3.95	2.77	3.45
0.86	6.37	4.00	3.99
1.28	12.99	17.82	10.09
1.71	17.47	22.33	7.09
2.14	24.63	26.09	6.08
2.57	43.95	34.18	5.37
3	49.74	30.63	3.98
3.42	52.60	35.71	4.68
3.85	47.40	31.71	3.77
4.28	53.01	32.63	3.50
4.71	64.48	33.20	3.08
5.14	67.18	32.56	2.93
5.56	68.54	28.27	2.13
5.99	60.23	29.04	2.64
6.42	56.48	25.43	2.50
6.85	56.58	20.98	1.91
7.28	55.19	20.88	1.85
7.7	52.05	21.32	1.78
8.13	51.18	22.31	1.87
8.56	49.93	22.47	1.84
8.99	49.50	23.19	1.85
9.42	47.30	23.56	1.88
9.84	48.63	24.72	1.85
10.27	55.03	28.27	2.18
10.7	54.22	29.35	2.22
11.13	58.09	32.61	2.51
11.56	56.39	32.67	2.48
11.98	55.38	33.63	2.65
12.41	50.47	34.24	2.42
12.84	50.08	33.24	2.52
13.27	47.47	32.41	2.43
13.7	45.92	32.81	2.36
14.12	46.49	31.62	2.25
14.55	43.90	31.85	2.20
14.98	43.40	32.24	2.29
15.41	42.10	32.83	2.24
15.84	40.10	32.44	2.31
16.26	38.88	30.78	2.19
16.69	38.72	31.87	2.17
17.12	38.93	32.05	2.27
17.55	36.68	32.71	2.21
17.98	33.61	30.37	2.09
18.4	37.19	33.50	2.38
18.83	35.42	33.23	2.37
19.26	34.74	33.47	2.34
19.69	34.26	32.98	2.45
20.12	33.72	32.74	2.40
20.54	32.69	32.25	2.41
20.97	31.44	32.49	2.52
21.4	31.16	32.30	2.47
21.83	32.24	30.14	2.15
22.26	32.46	29.63	2.05
22.68	31.86	30.72	2.10
23.11	31.41	31.12	2.12
23.54	30.74	31.29	2.10
23.97	29.21	31.35	2.08
24.4	28.23	30.09	1.96
24.82	28.45	30.66	2.09
25.25	27.50	30.90	1.97
25.68	24.99	29.05	1.95
26.11	25.77	28.88	1.92
26.54	26.83	30.90	2.15
26.96	26.51	31.97	2.18
27.39	26.34	31.45	2.21
27.82	26.00	31.39	2.18
28.25	25.19	31.09	2.15
28.68	24.47	29.42	2.24
29.1	23.98	30.53	2.23
29.53	23.91	30.81	2.23
29.96	21.15	28.03	1.98
30.39	22.44	30.63	2.27
30.82	19.89	28.80	2.03
31.24	19.92	28.06	2.05
31.67	20.09	27.76	2.10
32.1	19.90	27.41	2.05
32.53	19.81	28.29	2.24
32.96	18.71	27.78	2.17
33.38	20.24	30.05	2.36
33.81	18.23	27.04	2.19
34.24	19.98	29.96	2.39
34.67	19.66	29.10	2.29
35.1	17.97	27.24	2.20
35.52	17.71	27.41	2.23
35.95	17.69	26.96	2.26
36.38	17.12	27.03	2.23
36.81	17.36	26.85	2.28
37.24	16.91	27.46	2.31
37.66	16.91	26.66	2.34

38.09	16.55	26.72	2.37
38.52	18.68	29.96	2.61
38.95	17.11	27.54	2.42
39.38	16.87	28.00	2.44
39.8	16.58	27.60	2.48
40.23	16.28	27.20	2.52
40.66	16.23	27.00	2.47
41.09	15.91	27.08	2.47
41.52	15.31	26.51	2.42
41.94	15.66	27.45	2.48
42.37	15.40	26.62	2.47
42.8	15.38	27.05	2.55
43.23	15.40	27.47	2.57
43.66	14.98	26.78	2.51
44.08	15.46	27.08	2.62
44.51	13.65	25.72	2.43
44.94	13.48	25.10	2.47
45.37	14.21	24.85	2.41
45.8	15.94	24.39	2.16
46.22	15.47	24.75	2.12
46.65	15.09	24.91	2.10
47.08	14.42	24.89	2.12
47.51	14.14	23.76	2.08
47.94	14.43	24.44	2.21
48.36	14.30	24.65	2.19
48.79	13.99	24.75	2.17
49.22	13.69	24.46	2.20
49.65	13.03	23.48	2.15
50.08	12.91	23.01	2.16
50.5	12.80	23.00	2.17
50.93	13.48	24.40	2.48
51.36	13.59	25.14	2.46
51.79	13.66	25.12	2.52
52.22	13.28	24.71	2.51
52.64	12.75	23.99	2.49
53.07	12.88	24.10	2.54
53.5	12.57	24.07	2.56
53.93	12.65	24.16	2.56
54.36	12.59	24.23	2.61
54.78	12.30	23.94	2.67
55.21	12.54	24.07	2.74
55.64	12.33	25.28	2.75
56.07	12.33	23.82	2.72
56.5	12.38	24.89	2.80
56.92	11.63	23.68	2.87
57.35	11.28	22.53	2.75
57.78	11.11	22.55	2.78
58.21	10.80	22.23	2.81
58.64	11.34	22.81	2.93
59.06	11.31	22.26	2.89
59.49	11.03	22.54	2.99
59.92	11.01	23.50	2.99
60.35	11.14	22.83	3.03
60.78	10.96	21.95	3.01
61.2	10.91	22.52	3.10
61.63	11.01	22.65	3.02
62.06	10.26	22.32	3.09
62.49	10.41	22.26	3.06
62.92	9.95	21.81	3.07
63.34	10.31	21.78	3.07
63.77	10.64	22.54	3.18
64.2	9.93	21.19	3.09
64.63	10.33	22.07	3.28
65.06	9.71	20.86	3.16
65.48	9.61	20.83	3.08
65.91	9.72	20.84	3.18
66.34	9.77	21.15	3.16
66.77	9.38	20.81	3.13
67.2	9.73	21.13	3.22
67.62	9.23	20.76	3.27

Table 14: NB values for the three size categories for AQ6.

PV	$< 10^3\ \mu m^2$	10^3-$10^4\ \mu m^2$	$> 10^4\ \mu m^2$
0	0.92	0.80	0.85
0.43	4.04	2.27	3.54
0.86	5.92	2.63	3.07
1.28	6.05	2.45	2.55
1.71	5.76	2.18	1.85
2.14	5.65	2.12	1.88
2.57	7.15	2.69	2.14
3	6.70	2.43	1.80
3.42	7.02	2.75	2.00
3.85	6.09	2.49	1.71
4.28	6.31	2.58	1.90
4.71	7.33	2.83	1.94
5.14	7.28	2.95	1.93
5.56	6.70	2.69	1.68
5.99	6.24	2.68	1.67
6.42	6.18	2.64	1.78
6.85	6.32	2.53	1.61
7.28	5.87	2.44	1.57
7.7	5.62	2.39	1.51
8.13	5.57	2.48	1.64
8.56	5.45	2.51	1.79
8.99	5.53	2.63	1.83
9.42	5.28	2.65	1.86
9.84	5.62	2.68	1.86
10.27	6.46	3.09	2.21
10.7	6.51	3.10	2.36
11.13	7.05	3.48	2.55
11.56	6.89	3.50	2.47
11.98	6.83	3.63	2.76
12.41	6.22	3.72	2.77
12.84	6.17	3.58	3.06
13.27	5.92	3.40	2.86
13.7	5.92	3.46	2.88
14.12	5.86	3.38	2.88
14.55	5.70	3.30	2.74
14.98	5.69	3.35	2.80
15.41	5.59	3.34	2.76
15.84	5.39	3.28	2.83
16.26	5.26	3.11	2.69
16.69	5.31	3.25	2.74
17.12	7.03	6.69	6.46
17.55	7.51	14.04	9.25
17.98	6.76	12.92	8.55
18.4	7.51	14.18	9.94
18.83	7.11	14.03	10.00
19.26	7.01	13.96	9.80
19.69	7.10	13.69	10.27
20.12	7.91	15.89	9.29
20.54	7.67	15.54	9.14
20.97	7.51	15.80	9.18
21.4	7.32	15.58	9.33
21.83	7.26	15.30	9.54
22.26	7.42	15.15	9.42
22.68	7.41	15.55	9.65
23.11	7.40	15.62	9.81
23.54	7.39	15.56	9.55
23.97	7.18	15.39	9.34
24.4	6.98	14.72	8.82
24.82	7.21	14.94	9.35
25.25	7.13	15.08	8.99
25.68	6.62	14.11	8.56
26.11	6.88	13.95	8.49
26.54	7.38	15.05	9.54
26.96	7.34	15.57	9.57
27.39	7.36	15.28	9.80
27.82	7.41	15.31	9.50
28.25	7.24	15.08	9.37
28.68	7.09	14.21	9.63
29.1	7.06	14.73	9.67
29.53	7.15	14.83	9.63
29.96	6.28	13.22	8.28
30.39	6.86	14.71	9.72
30.82	6.17	13.85	8.65
31.24	6.27	13.57	8.61
31.67	6.52	13.73	8.68
32.1	6.43	13.50	8.30
32.53	6.42	13.89	8.93
32.96	6.11	13.57	8.64
33.38	6.62	14.64	9.50
33.81	5.99	13.17	8.68
34.24	6.60	14.50	9.41
34.67	6.56	14.03	8.93
35.1	6.03	13.18	8.71
35.52	6.00	13.30	8.66
35.95	6.00	13.04	8.77
36.38	5.87	13.05	8.73
36.81	5.97	12.96	8.71
37.24	5.89	13.22	8.92
37.66	5.93	12.87	8.96

38.09	5.81	12.89	9.12
38.52	6.55	14.42	9.94
38.95	6.07	13.28	9.09
39.38	6.01	13.53	9.06
39.8	5.92	13.31	9.18
40.23	5.87	13.14	9.22
40.66	5.84	12.99	9.04
41.09	5.79	13.03	9.08
41.52	5.56	12.75	8.79
41.94	5.68	13.21	9.08
42.37	5.62	12.82	9.04
42.8	5.62	13.01	9.22
43.23	5.66	13.20	9.29
43.66	5.49	12.93	8.91
44.08	5.73	13.06	9.24
44.51	5.11	12.42	8.51
44.94	5.47	13.43	8.85
45.37	6.85	16.20	7.03
45.8	6.84	16.29	6.80
46.22	6.67	16.26	6.74
46.65	6.59	16.48	6.64
47.08	6.38	16.36	6.74
47.51	6.31	15.53	6.68
47.94	6.39	15.91	7.05
48.36	6.28	16.03	7.08
48.79	6.15	15.99	6.92
49.22	6.11	15.78	7.11
49.65	5.86	15.14	6.75
50.08	5.82	14.74	6.82
50.5	5.84	14.72	6.79
50.93	6.18	15.58	7.85
51.36	6.28	16.02	7.69
51.79	6.30	16.00	7.86
52.22	6.16	15.76	7.68
52.64	5.89	15.15	7.66
53.07	6.04	15.26	7.79
53.5	5.91	15.18	7.78
53.93	5.91	15.03	7.63
54.36	5.94	15.27	7.83
54.78	5.81	15.07	7.99
55.21	5.93	15.15	8.14
55.64	5.83	15.84	8.14
56.07	5.83	14.93	8.07
56.5	5.84	15.57	8.17
56.92	5.50	14.84	8.27
57.35	5.44	14.10	8.03
57.78	5.32	14.17	8.07
58.21	5.17	13.98	8.06
58.64	5.54	14.40	8.29
59.06	5.50	14.08	8.11
59.49	5.40	14.23	8.43
59.92	5.33	14.76	8.25
60.35	5.41	14.28	8.32
60.78	5.28	13.80	8.28
61.2	5.30	14.12	8.45
61.63	5.36	14.19	8.34
62.06	5.04	14.08	8.32
62.49	5.11	13.90	8.34
62.92	4.91	13.67	8.25
63.34	5.13	13.66	8.21
63.77	5.22	14.07	8.44
64.2	4.87	13.22	8.17
64.63	5.08	13.75	8.60
65.06	4.74	13.02	8.24
65.48	4.75	13.03	7.95
65.91	4.81	13.04	8.23
66.34	4.86	13.23	8.24
66.77	4.64	13.04	8.00
67.2	4.89	13.19	8.29
67.62	4.59	12.95	8.45

Scripts

```python
# -*- coding: utf-8 -*-
"""
Created on Tue Nov 12 11:34:49 2019

@author: bbe020
"""

import cv2 as cv
import numpy as np
import os
from PIL import Image
from shapely.geometry.polygon import Polygon
from shapely.ops import nearest_points
import datetime
import pandas as pd
from math import sqrt
from shapely.geometry import LineString

# This function loops through all the pictures in a folder and saves the result as a CSV file.
def main():
    names = img_names("F:/foam oktober/bilder/Experiment-74") # The path of the folder
    t = datetime.datetime.now()
    print("Start time: ",t)
    for i in names:
        result = findbobbel(i)
        name = "F:/foam oktober/result/Experiment-74/"+i[-7:-4]+".csv"
        result.to_csv(name,index = False)
        print(datetime.datetime.now()-t,"\t",i)
        t = datetime.datetime.now()

# This function returns the image names in the folder directed to.
def img_names(folder_name):
    liste = os.listdir(folder_name)
    names = []
    for i in liste:
        if i[:10] == "Experiment":
            names.append(i)
    return names

# This function threshold the pictures, saves the threshold image of the bubbles for each image, and returns contours of grains and bubbles, a threshold image of the grains, and its height and width to the findlines function.
def thresh(imgname):
    name = "F:/foam oktober/bilder/Experiment-74/"+imgname
    img = cv.imread(name,0) # Reads image in the grayscale

    img = Image.fromarray(img)
    width,hight = img.size
```

```
    box = 500,500,width-500,hight-500
    img = img.crop(box) # crops the image to remove noise in the edges.
    img = np.array(img, dtype = np.uint8)
    hight,width = img.shape
    thresh_grains = np.full((hight+50,width+50,3), 255,np.uint8)
    e_img = np.full((hight+50,width+50,3), 0,np.uint8)
#    plt.plot(cv.calcHist([img],[0],None,[256],[0,256])) # Can be used to
define the threshold parameters
"---------------------grains segmentation method--------------------"
    ret,img_1 = cv.threshold(img,70,255,cv.THRESH_BINARY) # Thresholds
    image to get grains.
    e_img1 = np.full((hight+50,width+50), 255,np.uint8)
    x_offset=y_offset=25
    e_img1[y_offset:y_offset+hight, x_offset:x_offset+width] = img_1 #
    Makes a frame in order to find grains in the edges.
    img_1 = e_img1
    _,con,Hierarchy=cv.findContours(img_1, cv.RETR_TREE,
    cv.CHAIN_APPROX_SIMPLE)
    con = con[1:]
    contours = []
    for i in range(len(con)): # Removes grains that have an area less than
                                10 pixels to get rid of noise
        a = cv.contourArea(con[i])
        if a > 10 :
            contours.append(con[i])
    cv.drawContours(thresh_grains, contours,-1,(125,0,125),thickness = 1)
"--------------------Bubbles segmentation method---------------------"
    ret,img_2 = cv.threshold(img,125,255,cv.THRESH_BINARY_INV) # Thresholds
    image to get lamellae and grains edges.
    e_img2 = np.full((hight+50,width+50), 0,np.uint8)
    x_offset=y_offset=25
    e_img2[y_offset:y_offset+hight, x_offset:x_offset+width] = img_2
    img_2 = e_img2
    cv.drawContours(img_2, contours,-1, (0,0,0), thickness=2)
    cv.fillPoly(img_2, contours, 0) # Removes grains from img_2
    _,con1,Hierarchy=cv.findContours(img_2, cv.RETR_TREE,
    cv.CHAIN_APPROX_SIMPLE)
    con1 = con1[1:]
    contours_b = []
    for i in range(len(con1)): # Removes bubbles with area less than 10 and
    pores without bubbles
        a = cv.contourArea(con1[i])
        if 10 < a <1000000 and Hierarchy[0][i][3] == -1 :
            contours_b.append(con1[i])
    cv.fillPoly(e_img, contours_b, (255,255,255))
    hight,width,_ = thresh_grains.shape
"--------------------------------------------------------------------"
    os.chdir("F:/foam oktober/segment/Experiment-74")
    cv.imwrite(imgname[-7:],e_img)
    return contours,contours_b,width,hight,thresh_grains

# This function finds the nearest point among the neighboring grains.
def findlines(imgname):
    con,conb,width,hight,thresh_grains= thresh(imgname)
    polygons = []
```

```
    # This for loop converts grains contours to polygons
    for i in range(len(con)):
        box =con[i].copy()
        box = box.reshape(con[i].shape[0],2)
        for v in box:
            v[1] = hight-v[1]

        po = Polygon(box)
        polygons.append(po)

    x = []
    y = []
    area = []

    # This for loop finds the center and the area of the grains
    for i in range(len(polygons)):
        x1 = polygons[i].centroid.coords[0][0]
        x.append(x1)
        y1 = hight-polygons[i].centroid.coords[0][1]
        y.append(y1)
        a = cv.contourArea(con[i])
        area.append(a)

    centers_df = pd.DataFrame()
    centers_df["x"] = x
    centers_df["y"] = y
    centers_df["area"] = area

    lengths = []
    pos = []
    m_pos_x = []
    m_pos_y = []
    sjekk_dupl = []
    lines = []

    # This for loop finds the pore throats and makes sure that they do not
    intersect the grains.
    for i in range(len(centers_df)):
        x = centers_df.x.loc[i]
        y = centers_df.y.loc[i]
        a1 = centers_df.area.loc[i]

        a = centers_df[(centers_df.x-x).abs() < sqrt(a1)*2].index
        b = centers_df[(centers_df.y-y).abs() < sqrt(a1)*2].index
        c = a.append(b)
        d = c[c.duplicated()].unique()
        po1 = polygons[i]
        for n in d:
            po2 = polygons[n]
            p1, p2 = nearest_points(po1, po2)
            l= p1.distance(p2)
            line = LineString([p1,p2])
            ans = 0
            c = 0
            for v in d:
```

```
                c += 1
                po3 = polygons[v]
                if po3.touches(p1) or po3.touches(p2):
                    ans += 1
                else:
                    if not line.intersects(po3):
                        ans += 1

            if ans == c and ans != 0 and l != 0:
                dup = [i,n]
                dup.sort()
                sjekk_dupl.append(dup)
                pos.append((int(p1.coords[0][0]),int(hight-
                p1.coords[0][1]),int(p2.coords[0][0]),int(hight-
                p2.coords[0][1])))
                m_pos_x.append(line.centroid.coords[0][0])
                m_pos_y.append(line.centroid.coords[0][1])
                lengths.append(l)
                lines.append(line)

"------------find the lines from grains to the edges of image------------"
    con.append(np.array([[[20,20]],[[width-20,20]],[[width-20,hight-
    20]],[[21,hight-20]],[[21,21]],[[width-21,21]],[[width-21,hight-
    21]],[[20,hight-21]]]))
    box =con[len(con)-1].copy()
    box = box.reshape(con[len(con)-1].shape[0],2)
    for v in box:
        v[1] = hight-v[1]
    po = Polygon(box)
    polygons.append(po)
    a = centers_df[(centers_df.x-width).abs() < 50].index
    b = centers_df[(centers_df.x).abs() < 50].index
    c = centers_df[(centers_df.y-hight).abs() < 50].index
    d = centers_df[(centers_df.y).abs() < 50].index
    e = a.append(b)
    e = e.append(c)
    e = e.append(d)
    po1 = polygons[len(polygons)-1]
    for n in e:
        po2 = polygons[n]
        p1, p2 = nearest_points(po1, po2)
        l= p1.distance(p2)
        line = LineString([p1,p2])
        ans = 0
        k = 0
        for v in e:
            k += 1
            po3 = polygons[v]
            if po3.touches(p1) or po3.touches(p2):
                ans += 1
            else:
                if not line.intersects(po3):
                    ans += 1

        if ans == k and ans != 0 and l != 0:
```

```
            dup = [i,n]
            dup.sort()
            sjekk_dupl.append(dup)
            pos.append((int(p1.coords[0][0]),int(hight-
            p1.coords[0][1]),int(p2.coords[0][0]),int(hight-
            p2.coords[0][1])))
            m_pos_x.append(line.centroid.coords[0][0])
            m_pos_y.append(line.centroid.coords[0][1])
            lengths.append(l)
            lines.append(line)
"-----------------------------------------------------------------------"
    pos_t = []
    m_pos_x_t = []
    m_pos_y_t = []
    lengths_t = []
    lines_t = []
    df = pd.DataFrame(sjekk_dupl)
    df1 = df.drop_duplicates()
    ind = df1.index
    for i in ind:
        pos_t.append(pos[i])
        lengths_t.append(lengths[i])
        m_pos_x_t.append(m_pos_x[i])
        m_pos_y_t.append(m_pos_y[i])
        lines_t.append(lines[i])


    lst = pd.DataFrame(pos_t)
    lst.columns = ["x1","y1","x2","y2"]
    lst["lengths"] = lengths_t
    lst["x_center"] = m_pos_x_t
    lst["y_center"] = m_pos_y_t
    lst["lines"] = lines_t
    return lst,con,conb,thresh_grains,width,hight,polygons


# This function classifies the lines obtained from findlines function into three catagories(pore_throat,length_pore_throat, and rad_pore_throat).
def line_class(imgname):
    lst,contours,conb,thresh_grains,width,hight,polygons =
    findlines(imgname)
    pt = []
    m_pt = []
    l_pt = []
    d_pt = []
    l = []
    x_center = []
    y_center = []
# This for loop finds the lines that do not intersects other lines and append them to pt list, and append the other lines to m_pt list
    for i in range(len(lst)):
        line0 = lst.lines[i]
        l0 = line0.length
        if l0 != 0:
            a = lst[(lst.x_center-lst.x_center[i]).abs() <
```

```
            l0/sqrt(2)].index
            b = lst[(lst.y_center-lst.y_center[i]).abs() <
            l0/sqrt(2)].index
            c = a.append(b)
            d = c[c.duplicated()].unique()
            a = 0
            for n in d:
                line1 = lst.lines[n]
                l1 = line1.length

                if not line0.intersects(line1):
                    a += 1
            if a == len(d)-1:
                pt.append(line0)
            else :
                m_pt.append(line0)
                l.append(l0)
                x_center.append(lst.x_center[i])
                y_center.append(lst.y_center[i])

    df = pd.DataFrame()
    df["lines"] = m_pt
    df["length"] = l
    df["x_center"] = x_center
    df["y_center"] = y_center
    df = df.sort_values(by = ["length"])
    df = df.iloc[::-1]
    df = df.reset_index()
    ind = []

# This for loop classifies the lines in m_pt list into three catagories
(pore_throat,length_pore_throat, and rad_pore_throat)
    for i in range(len(df)):
        if i not in ind:
            line0 = df["lines"][i]
            l0 = df["length"][i]

            a = df[(df.x_center-df.x_center[i]).abs() < 2*l0].index
            b = df[(df.y_center-df.y_center[i]).abs() < 2*l0].index
            c = a.append(b)
            d = c[c.duplicated()].unique()
            a = []
            l = []
            ind.append(i)
            for z in d:
                if z not in ind:
                    line1 = df["lines"][z]
                    l1 = df["length"][z]
                    if line0.intersects(line1):
                        a.append([z,line1])
                        l.append(l1)
            if len(a) == 0:
                pt.append(line0)
            else:
                l_pt.append(line0)
```

```
                d_pt.append(a[l.index(min(l))][1])
                ind.append(a[l.index(min(l))][0])


    pore_throat = []
    # This for loop draws pore throats obtained into thresh_grains image,
    and append all the data needed into a list
    for i in pt:
        p1 =(int(i.boundary[0].coords[0][0]),hight-
        int(i.boundary[0].coords[0][1]))
        p2 =(int(i.boundary[1].coords[0][0]),hight-
        int(i.boundary[1].coords[0][1]))
        cv.line(thresh_grains,p1,p2,(255,0,0),1)
        l = i.length
        x = i.centroid.coords[0][0]
        y = hight-i.centroid.coords[0][1]
        pore_throat.append((p1[0],p1[1],p2[0],p2[1],l,x,y,i))

    length_pore_throat = []
    # This for loop draws pore throats lengths obtained into thresh_grains
    image, and append all the data needed into a list
    for i in l_pt:
        p1 =(int(i.boundary[0].coords[0][0]),hight-
        int(i.boundary[0].coords[0][1]))
        p2 =(int(i.boundary[1].coords[0][0]),hight-
        int(i.boundary[1].coords[0][1]))
        l = i.length
        x = i.centroid.coords[0][0]
        y = hight-i.centroid.coords[0][1]
        length_pore_throat.append((p1[0],p1[1],p2[0],p2[1],l,x,y))

    rad_pore_throat = []
    # This for loop draws pore throats radiis obtained into thresh_grains
    image, and append all the data needed into a list
    for i in d_pt:
        p1 =(int(i.boundary[0].coords[0][0]),hight-
        int(i.boundary[0].coords[0][1]))
        p2 =(int(i.boundary[1].coords[0][0]),hight-
        int(i.boundary[1].coords[0][1]))
        cv.line(thresh_grains,p1,p2,(0,255,0),1)
        l = i.length
        x = i.centroid.coords[0][0]
        y = hight-i.centroid.coords[0][1]
        rad_pore_throat.append((p1[0],p1[1],p2[0],p2[1],l,x,y,i))


    lst1 = pd.DataFrame(pore_throat)
    lst1.columns["x1","y1","x2","y2","lengths","x_center","y_center",
    "lines"]

    lst2 = pd.DataFrame(length_pore_throat)
    lst2.columns = ["x1","y1","x2","y2","lengths","x_center","y_center"]

    lst3 = pd.DataFrame(rad_pore_throat)
    lst3.columns = ["x1","y1","x2","y2","lengths","x_center","y_center",
```

```
    "lines"]

    return lst1,lst3,contours,conb,width,hight,polygons,thresh_grains

# This function runs through all the bubbles to find the grains and pore throts enclosing them, and saves the data in a pandas dataframe.
def findbobbel(imgname):
    lst,lst1,contours,contours_b,width,hight,polygons,thresh_grains =
    line_class(imgname)

    polygons_b = []
    Area = []
    # This for loop converts bubbles contours to polygons
    for i in range(len(contours_b)):
        box =contours_b[i].copy()
        a = cv.contourArea(box)
        Area.append(a)
        box = box.reshape(contours_b[i].shape[0],2)
        for v in box:
            v[1] = hight-v[1]

        po = Polygon(box)
        polygons_b.append(po)


    x = []
    y = []
    # This for lopp finds centers of grains
    for i in range(len(polygons)):
        x1 = polygons[i].centroid.coords[0][0]
        x.append(x1)
        y1 = hight-polygons[i].centroid.coords[0][1]
        y.append(y1)
    con = pd.DataFrame()
    con["x"] = x
    con["y"] = y


    po_exterior = polygons[-1:][0]

    thresh_grains = Image.fromarray(thresh_grains)
    width,hight = thresh_grains.size
    box = 25,25,width-25,hight-25
    thresh_grains = thresh_grains.crop(box)
    thresh_grains = np.array(thresh_grains, dtype = np.uint8)

    e_img = np.full((hight,width,3), (125,125,125),np.uint8)
    x_offset=y_offset=25
    e_img[y_offset:hight-y_offset, x_offset:width-x_offset] = thresh_grains
    thresh_grains = e_img

    result = pd.DataFrame(columns
    =["x_center","y_center","Areal","Omkrets","Antall linjer","linjer
    lengde","avstand linjer","sirkularitet","orientering","ma","Ma"])
```

```
        # This for lopp runs through all the bubbles to find the grains and
        pore throts enclosing them
        for i in range(len(polygons_b)):
            linjer_s = []
            linjer = []
            linjer1_s = []
            linjer1 = []

            po = polygons_b[i]

            x = po.centroid.coords[0][0]
            y = hight-po.centroid.coords[0][1]
            box_x = po.bounds[2]-po.bounds[0]+50
            box_y = po.bounds[3]-po.bounds[1]+50

            x1 = int(po.bounds[0]-200)
            x2 = int(po.bounds[2]+200)
            y1 = int(hight-po.bounds[3]-200)
            y2 = int(hight-po.bounds[1]+200)
            if x1 < 0:
                x1 = 0
            if y1 < 0:
                y1 = 0

            try: # Uses try to avoid script crash since some polygons are
                 damaged and have to use buffer function on them. If buffer
                 function is used on an undamaged polygon, then it will be
                 damaged therefore the buffer function is used after except
                e_img = []
                e_img.append(thresh_grains[y1:y2,x1:x2].copy())
                e_img = e_img[0]

                a = lst[(lst.x_center-x).abs() < box_x ].index
                b = lst[(lst.y_center-y).abs() < box_y].index
                c = a.append(b)
                ind_lines = c[c.duplicated()].unique()
                # This for lopp finds pore throats that intersecting the bubble
                and draw it using white color on the e_img to remove them so
                that fill function can reach all the enclosing porethroats and
                grains
                for z in ind_lines:
                    line = lst.lines[z]
                    if line.intersects(po):
                        linjer_s.append(z)
                        cv.line(e_img,(lst.x1.loc[z]-x1,lst.y1.loc[z]y1),
                        (lst.x2.loc[z]-x1,lst.y2.loc[z]-y1),(255,255,255),1)
                    else:
                        linjer.append(z)

                a = lst1[(lst1.x_center-x).abs() < box_x].index
                b = lst1[(lst1.y_center-y).abs() < box_y].index
                c = a.append(b)
                ind_lines1 = c[c.duplicated()].unique()
                # This for lopp finds pore throats radii that intersecting the
                bubble and draw it using white color on the e_img to remove
```

```
                them so that fill function can reach all the enclosing
                porethroats and grains
                for z in ind_lines1:
                    line = lst1.lines[z]
                    if line.intersects(po):
                        linjer1_s.append(z)
                        cv.line(e_img,(lst1.x1.loc[z]-x1,lst1.y1.loc[z]-y1),
                        (lst1.x2.loc[z]-x1,lst1.y2.loc[z]-y1),(255,255,255),1)
                    else:
                        linjer1.append(z)
                # This for loop draw all the enclosing pore throats radii using
                green color on the e_img so that fill function does not leak
                between pore throats radii and grains
                for z in linjer1:
                    if z not in linjer1_s:
                        cv.line(e_img,(lst1.x1.loc[z]-x1,lst1.y1.loc[z]-y1),
                        (lst1.x2.loc[z]-x1,lst1.y2.loc[z]-y1),(0,255,0),1)

                # This for loop draw all the enclosing pore throats using blue
                color on the e_img so that fill function does not leak between
                pore throats and grains
                for z in linjer:
                    if z not in linjer_s:
                        cv.line(e_img,(lst.x1.loc[z]-x1,lst.y1.loc[z]-y1),
                        (lst.x2.loc[z]-x1,lst.y2.loc[z]-y1),(255,0,0),1)

                a = con[(con.x-x).abs() < box_x+50].index
                b = con[(con.y-y).abs() < box_y+50].index
                c = a.append(b)
                ind_polygons = c[c.duplicated()].unique()
                conf = []
                # This for loop draw all the enclosing grains using purple
                color on the e_img so that fill function does not leak between
                pore throats and grains
                for v in ind_polygons:
                    conf.append(contours[v])
                    for g in contours[v]:
                        g[0][0] = g[0][0]-x1
                        g[0][1] = g[0][1]-y1
                cv.drawContours(e_img, conf,-1, (102,0,102), thickness=1)

                cv.floodFill(e_img,None,(int(x-x1),int(y-y1)),(0,0,0))
            except:
                po1 = po.buffer(0)
                e_img = []
                e_img.append(thresh_grains[y1:y2,x1:x2].copy())
                e_img = e_img[0]

                a = lst[(lst.x_center-x).abs() < box_x ].index
                b = lst[(lst.y_center-y).abs() < box_y].index
                c = a.append(b)
                ind_lines = c[c.duplicated()].unique()
                for z in ind_lines:
                    line = lst.lines[z]
                    if line.intersects(po):
```

```
            linjer_s.append(z)
            cv.line(e_img,(lst.x1.loc[z]-x1,lst.y1.loc[z]y1),
            (lst.x2.loc[z]-x1,lst.y2.loc[z]-y1),(255,255,255),1)
        else:
            linjer.append(z)

    a = lst1[(lst1.x_center-x).abs() < box_x].index
    b = lst1[(lst1.y_center-y).abs() < box_y].index
    c = a.append(b)
    ind_lines1 = c[c.duplicated()].unique()
    for z in ind_lines1:
        line = lst1.lines[z]
        if line.intersects(po):
            linjer1_s.append(z)
            cv.line(e_img,(lst1.x1.loc[z]-x1,lst1.y1.loc[z]-y1),
            (lst1.x2.loc[z]-x1,lst1.y2.loc[z]-y1),(255,255,255),1)
        else:
            linjer1.append(z)
    for z in linjer1:
        if z not in linjer1_s:
            cv.line(e_img,(lst1.x1.loc[z]-x1,lst1.y1.loc[z]-y1),
            (lst1.x2.loc[z]-x1,lst1.y2.loc[z]-y1),(0,255,0),1)

    for z in linjer:
        if z not in linjer_s:
            cv.line(e_img,(lst.x1.loc[z]-x1,lst.y1.loc[z]-y1),
            (lst.x2.loc[z]-x1,lst.y2.loc[z]-y1),(255,0,0),1)

    a = con[(con.x-x).abs() < box_x+50].index
    b = con[(con.y-y).abs() < box_y+50].index
    c = a.append(b)
    ind_polygons = c[c.duplicated()].unique()
    conf = []
    for v in ind_polygons:
        conf.append(contours[v])
        for g in contours[v]:
            g[0][0] = g[0][0]-x1
            g[0][1] = g[0][1]-y1
    cv.drawContours(e_img, conf,-1, (102,0,102), thickness=1)

    cv.floodFill(e_img,None,(int(x-x1),int(y-y1)),(0,0,0))

e_img = cv.cvtColor(e_img, cv.COLOR_BGR2GRAY)
ret,img = cv.threshold(e_img,1,255,cv.THRESH_BINARY)



_,con_o,Hierarchy=cv.findContours(e_img, cv.RETR_TREE,
cv.CHAIN_APPROX_SIMPLE)
if len(con_o) == 1:
    box = con_o[0].copy()
else:
    con_o = con_o[1:]
    box = con_o[0].copy()
box = box.reshape(box.shape[0],2)
```

```
        for v in box:
            v[0] = v[0]+x1
            v[1] = hight-v[1]-y1
        po_o = Polygon(box) # Fill polygon
        try : # Uses try to avoid script crash since some fill polygons are
             damaged and have to use buffer function on them. If buffer
             function is used on an undamaged polygon, then it will be
             damaged therefore the buffer function is used after except

            # This for loop moves the polygons to the rigt location since
            different coordinate systems are used
            for v in ind_polygons:
                for g in contours[v]:
                    g[0][0] = g[0][0]+x1
                    g[0][1] = g[0][1]+y1
            antall_linjer = 0
            linjer_lengde = []
            avstand_linjer = []
            # This for loop obtain data for pore throrats enclosing the
            bubble
            for v in linjer:
                if v not in linjer_s:
                    line = lst.lines[v]
                    if line.intersects(po_o) and not
                    line.intersects(po_exterior):
                        antall_linjer += 1
                        linjer_lengde.append(line.length)
                        avstand_linjer.append(line.distance(po))

            # This for loop obtain data for pore throrats enclosing the
            bubble
            for v in linjer1:
                if v not in linjer1_s:
                    line = lst1.lines[v]
                    if line.intersects(po_o) and not
                    line.intersects(po_exterior):
                        antall_linjer += 1
                        linjer_lengde.append(line.length)
                        avstand_linjer.append(line.distance(po))

            area = cv.contourArea(contours_b[i])
            perimeter = cv.arcLength(contours_b[i],True)
            sirkularitet = (4*np.pi*area)/(perimeter**2)
            if len(contours_b[i]) >4:
                (ma,Ma),angle = cv.fitEllipse(contours_b[i])[1:]
            else:
                angle = -1
                ma = -1
                Ma = -1
            result = result.append({"x_center":x,"y_center":y,"Areal":
            area,"Omkrets":perimeter,"Antall linjer":antall_linjer,
            "linjer lengde":linjer_lengde,"avstand linjer":
            avstand_linjer,"sirkularitet":sirkularitet,"orientering":
            angle,"ma":ma,"Ma":Ma},ignore_index=True)
```

```
        except:
            po_o = po_o.buffer(0)
            for v in ind_polygons:
                for g in contours[v]:
                    g[0][0] = g[0][0]+x1
                    g[0][1] = g[0][1]+y1
            antall_linjer = 0
            linjer_lengde = []
            avstand_linjer = []
            for v in linjer:
                if v not in linjer_s:
                    line = lst.lines[v]
                    if line.intersects(po_o) and not
                    line.intersects(po_exterior):
                        antall_linjer += 1
                        linjer_lengde.append(line.length)
                        avstand_linjer.append(line.distance(po))


            for v in linjer1:
                if v not in linjer1_s:
                    line = lst1.lines[v]
                    if line.intersects(po_o) and not
                    line.intersects(po_exterior):
                        antall_linjer += 1
                        linjer_lengde.append(line.length)
                        avstand_linjer.append(line.distance(po))

            area = cv.contourArea(contours_b[i])
            perimeter = cv.arcLength(contours_b[i],True)
            sirkularitet = (4*np.pi*area)/(perimeter**2)
            if len(contours_b[i]) >4:
                (ma,Ma),angle = cv.fitEllipse(contours_b[i])[1:]
            else:
                angle = -1
                ma = -1
                Ma = -1
            result = result.append({"x_center":x,"y_center":y,"Areal":
            area,"Omkrets":perimeter,"Antall linjer":antall_linjer,
            "linjer lengde":linjer_lengde,"avstand linjer":
            avstand_linjer,"sirkularitet":sirkularitet,"orientering":
            angle,"ma":ma,"Ma":Ma},ignore_index=True)
    return result
```

References

Akbar, M., Vissapragada, B., Alghamdi, A. H., Allen, D., Herron, M., Carnegie, A., . . . Saxena, K. (2000). A Snapshot of Carbonate Reservoir Evaluation. *Oilfield Review, 12*, 20-41.

Alkan, H., Goktekin, A., & Satman, A. (1991). *A Laboratory Study of CO2-Foam Process for Bati Raman Field, Turkey*. Paper presented at the Middle East Oil Show, Bahrain. https://doi.org/10.2118/21409-MS

Anderson, W. G. (1987a). Wettability literature survey part 4: Effects of Wettability on Capillary Pressure. *Journal of petroleum technology*.

Anderson, W. G. (1987b). Wettability literature survey part 5: Effects of Wettability on Relative Permeability. *Journal of petroleum technology*.

Apaydin, O. G., & Kovscek, A. R. (2001). Surfactant Concentration and End Effects on Foam Flow in Porous Media. *Transport in Porous Media, 43*(3), 511-536. Retrieved from https://doi.org/10.1023/A:1010740811277. doi:10.1023/A:1010740811277

Auffan, M., Rose, J., Bottero, J.-Y., Lowry, G. V., Jolivet, J.-P., & Wiesner, M. R. (2009). Towards a definition of inorganic nanoparticles from an environmental, health and safety perspective. *Nature Nanotechnology, 4*(10), 634-641. Retrieved from https://doi.org/10.1038/nnano.2009.242. doi:10.1038/nnano.2009.242

Bahadori, A. (2018). *Fundamentals of Enhanced Oil and Gas Recovery from Conventional and Unconventional Reservoirs*.

Baklid, A., Korbol, R., & Owren, G. (1996). *Sleipner Vest CO2 Disposal, CO2 Injection Into A Shallow Underground Aquifer*. Paper presented at the SPE Annual Technical Conference and Exhibition, Denver, Colorado. https://doi.org/10.2118/36600-MS

Bekken, S. G., Schöffel, K., Aakenes, S., Hatlen, T., Slagtern, Å., & Øi, L. E. (2013). The CLIMIT Program and its Strategy for Norwegian Research, Development and Demonstration of CCS Technology. *Energy Procedia, 37*, 6508-6519. Retrieved from http://www.sciencedirect.com/science/article/pii/S1876610213008242. doi:https://doi.org/10.1016/j.egypro.2013.06.581

Bennetzen, M. V., & Mogensen, K. (2014). *Novel Applications of Nanoparticles for Future Enhanced Oil Recovery*. Paper presented at the International Petroleum Technology Conference, Kuala Lumpur, Malaysia. https://doi.org/10.2523/IPTC-17857-MS

Boggs, S. (2006). *Principles of sedimentology and stratigraphy* (4th ed. ed.). Upper Saddle River, N.J: Pearson Prentice Hall.

Buchgraber, M., Al-Dossary, M., Ross, C. M., & Kovscek, A. R. (2012). Creation of a dual-porosity micromodel for pore-level visualization of multiphase flow. *Journal of Petroleum Science and Engineering, 86-87*, 27-38. Retrieved from http://www.sciencedirect.com/science/article/pii/S0920410512000654. doi:https://doi.org/10.1016/j.petrol.2012.03.012

Chen, L., Wang, M., Kang, Q., & Tao, W. (2018). Pore scale study of multiphase multicomponent reactive transport during CO2 dissolution trapping. *Advances in Water Resources, 116*, 208-218. Retrieved from http://www.sciencedirect.com/science/article/pii/S0309170817308977. doi:https://doi.org/10.1016/j.advwatres.2018.02.018

Cobb, W. M., & Marek, F. J. (1997). *Determination of Volumetric Sweep Efficiency in Mature Waterfloods Using Production Data*. Paper presented at the SPE Annual Technical Conference and Exhibition, San Antonio, Texas. https://doi.org/10.2118/38902-MS

Cuccia, L., Dugay, J., Bontemps, D., Louis-Louisy, M., & Vial, J. (2018). Analytical methods for the monitoring of post-combustion CO2 capture process using amine solvents: A review. *International Journal of Greenhouse Gas Control, 72*, 138-151. Retrieved from http://www.sciencedirect.com/science/article/pii/S1750583617306588. doi:https://doi.org/10.1016/j.ijggc.2018.03.014

David, A., & Marsden, S. S., Jr. (1969). *The Rheology of Foam*. Paper presented at the Fall Meeting of the Society of Petroleum Engineers of AIME, Denver, Colorado. https://doi.org/10.2118/2544-MS

De Muynck, W., De Belie, N., & Verstraete, W. (2010). Microbial carbonate precipitation in construction materials: A review. *Ecological Engineering, 36*(2), 118-136. Retrieved from http://www.sciencedirect.com/science/article/pii/S092585740900113X. doi:https://doi.org/10.1016/j.ecoleng.2009.02.006

Dixit, A., Tsau, J. S., & Heller, J. P. (1994). *Laboratory Study on Surfactant-Based Selective Mobility Control*. Paper presented at the Permian Basin Oil and Gas Recovery Conference, Midland, Texas. https://doi.org/10.2118/27729-MS

Ediger, V. Ş. (2019). An integrated review and analysis of multi-energy transition from fossil fuels to renewables. *Energy Procedia, 156*, 2-6. Retrieved from http://www.sciencedirect.com/science/article/pii/S1876610218310324. doi:https://doi.org/10.1016/j.egypro.2018.11.073

Edwards, R. W. J., & Celia, M. A. (2018). Infrastructure to enable deployment of carbon capture, utilization, and storage in the United States. *Proceedings of the National Academy of Sciences, 115*(38), E8815. Retrieved from http://www.pnas.org/content/115/38/E8815.abstract. doi:10.1073/pnas.1806504115

Enick, R. M., Olsen, D. K., Ammer, J. R., & Schuller, W. (2012). *Mobility and Conformance Control for CO2 EOR via Thickeners, Foams, and Gels -- A Literature Review of 40 Years of Research and Pilot Tests*. Paper presented at the SPE Improved Oil Recovery Symposium, Tulsa, Oklahoma, USA. https://doi.org/10.2118/154122-MS

EPA. (2019). Greenhouse Gas Emissions. Retrieved 21.07.2019, from EPA https://www.epa.gov/ghgemissions/global-greenhouse-gas-emissions-data

Farajzadeh, R., Andrianov, A., Krastev, R., Hirasaki, G. J., & Rossen, W. R. (2012). Foam–oil interaction in porous media: Implications for foam assisted enhanced oil recovery. *Advances in Colloid and Interface Science, 183-184*, 1-13. Retrieved from http://www.sciencedirect.com/science/article/pii/S0001868612001121. doi:https://doi.org/10.1016/j.cis.2012.07.002

Firoozabadi, A., & Myint, P. C. (2010). Prospects for subsurface CO2 sequestration. *AIChE Journal, 56*(6), 1398-1405. Retrieved from https://doi.org/10.1002/aic.12287. doi:10.1002/aic.12287

Forchheimer, P. (1901). Wasserbewegung durch Boden. *Z. Ver. Deutsch, Ing., 45*, 1782-1788. Retrieved from https://ci.nii.ac.jp/naid/10010395788/en/.

Furre, A.-K., Eiken, O., Alnes, H., Vevatne, J. N., & Kiær, A. F. (2017). 20 Years of Monitoring CO2-injection at Sleipner. *Energy Procedia, 114*, 3916-3926. Retrieved from http://www.sciencedirect.com/science/article/pii/S1876610217317174. doi:https://doi.org/10.1016/j.egypro.2017.03.1523

Gerbelová, H., van der Spek, M., & Schakel, W. (2017). Feasibility Assessment of CO2 Capture Retrofitted to an Existing Cement Plant: Post-combustion vs. Oxy-fuel Combustion Technology. *Energy Procedia, 114*, 6141-6149. Retrieved from http://www.sciencedirect.com/science/article/pii/S1876610217319537. doi:https://doi.org/10.1016/j.egypro.2017.03.1751

Hansen, H., Eiken, O., & Aasum, T. O. (2005). *The path of a carbon dioxide molecule from a gas-condensate reservoir, through the amine plant and back down into the subsurface for storage. Case study: The Sleipner area, South Viking Graben, Norwegian North Sea*. Paper presented at the Offshore Europe, Aberdeen, United Kingdom. https://doi.org/10.2118/96742-MS

Hanssen, J. E., Holt, T., & Surguchev, L. M. (1994). *Foam Processes: An Assessment of Their Potential in North Sea Reservoirs Based on a Critical Evaluation of Current Field Experience*. Paper presented at the SPE/DOE Improved Oil Recovery Symposium, Tulsa, Oklahoma. https://doi.org/10.2118/27768-MS

Heller, J. P., Lien, C. L., & Kuntamukkula, M. S. (1985). Foamlike Dispersions for Mobility Control in CO2 Floods. *Society of Petroleum Engineers Journal, 25*(04), 603-613. Retrieved from https://doi.org/10.2118/11233-PA. doi:10.2118/11233-PA

Hornbrook, J. W., Castanier, L. M., & Pettit, P. A. (1991). *Observation of Foam/Oil Interactions in a New, High-Resolution Micromodel*. Paper presented at the SPE Annual Technical Conference and Exhibition, Dallas, Texas. https://doi.org/10.2118/22631-MS

Huntsman. (2019). Technical Bulletin Surfonic L24-22 Surfactant. Retrieved from https://monsonco.com/wp-content/uploads/2019/08/Surfonic-L-24-22.-TDS..pdf

IPCC. (2005). IPCC Special Report on Carbon Dioxide Capture and Storage. Prepared by Working Group III of the Intergovernmental Panel on Climate Change [Metz, B., O. Davidson, H. C. de Coninck, M. Loos, and L. A. Meyer (eds.)]. Cambridge University Press, Cambridge, United Kingdom and New York, NY, USA, 442 pp.

IPCC. (2014). *Climate Change 2014: Synthesis Report. Contribution of Working Groups I, II and III to the Fifth Assessment Report of the Intergovernmental Panel on Climate Change [Core Writing Team, R.K. Pachauri and L.A. Meyer (eds.)]. IPCC, Geneva, Switzerland, 151 pp.* Retrieved from

IPCC. (2018). Summary for Policymakers. In: Global Warming of 1.5°C. An IPCC Special Report on the impacts of global warming of 1.5°C above pre-industrial levels and related global greenhouse gas emission pathways, in the context of strengthening the global response to the threat of climate change, sustainable development, and efforts to eradicate poverty [Masson-Delmotte, V., P. Zhai, H.-O. Pörtner, D. Roberts, J. Skea, P.R. Shukla, A. Pirani, W. Moufouma-Okia, C. Péan, R. Pidcock, S. Connors, J.B.R. Matthews, Y. Chen, X. Zhou, M.I. Gomis, E. Lonnoy, Maycock, M. Tignor, and T. Waterfield (eds.)]. World Meteorological Organization, Geneva, Switzerland, 32 pp.

Jansen, D., Gazzani, M., Manzolini, G., Dijk, E. v., & Carbo, M. (2015). Pre-combustion CO2 capture. *International Journal of Greenhouse Gas Control, 40*, 167-187. Retrieved from http://www.sciencedirect.com/science/article/pii/S1750583615001917. doi:https://doi.org/10.1016/j.ijggc.2015.05.028

Kamali, F., Hussain, F., & Cinar, Y. (2015). A Laboratory and Numerical-Simulation Study of Co-Optimizing CO2 Storage and CO2 Enhanced Oil Recovery. *SPE Journal, 20*(06), 1227-1237. Retrieved from https://doi.org/10.2118/171520-PA. doi:10.2118/171520-PA

Kamat, P. V. (2007). Meeting the Clean Energy Demand: Nanostructure Architectures for Solar Energy Conversion. *The Journal of Physical Chemistry C, 111*(7), 2834-2860. Retrieved from https://doi.org/10.1021/jp066952u. doi:10.1021/jp066952u

Klinkenberg, L. J. (1941). *The Permeability Of Porous Media To Liquids And Gases*. Paper presented at the Drilling and Production Practice, New York, New York. https://doi.org/

Kontogeorgis, G. M., & Kiil, S. (2016). *Introduction to Applied Colloid and Surface Chemistry*. Chicester, UNITED KINGDOM: John Wiley & Sons, Incorporated.

Kuuskraa, V. A., Godec, M. L., & Dipietro, P. (2013). CO2 Utilization from “Next Generation” CO2 Enhanced Oil Recovery Technology. *Energy Procedia, 37*, 6854-6866. Retrieved from http://www.sciencedirect.com/science/article/pii/S1876610213008618. doi:https://doi.org/10.1016/j.egypro.2013.06.618

Lake, L. W., Johns, R., Rossen, W. R., & Pope, G. A. (2014). Fundamentals of enhanced oil recovery.

Laumb, J. D., Kay, J., Holmes, M. J., Cowan, R., Azenkeng, A., Heebink, L., . . . Raymond, L. J. (2013). Economic and Market Analysis of CO2 Utilization Technologies – Focus on CO2 derived from North Dakota lignite. *Energy Procedia, 37*, 6987-6998. doi:10.1016/j.egypro.2013.06.632

Lee, H. O., & Heller, J. P. (1990). Laboratory Measurements of CO2-Foam Mobility. *SPE Reservoir Engineering, 5*(02), 193-197. Retrieved from https://doi.org/10.2118/17363-PA. doi:10.2118/17363-PA

Liu, Q., & Maroto-Valer, M. M. (2014). Study of Mineral Trapping of CO2 and Seal Leakage Mitigation. *Energy Procedia, 63*, 5490-5494. Retrieved from http://www.sciencedirect.com/science/article/pii/S1876610214023960. doi:https://doi.org/10.1016/j.egypro.2014.11.581

Mabon, L., Shackley, S., & Bower-Bir, N. (2014). Perceptions of sub-seabed carbon dioxide storage in Scotland and implications for policy: A qualitative study. *Marine Policy, 45*, 9-15. Retrieved from http://www.sciencedirect.com/science/article/pii/S0308597X13002662. doi:https://doi.org/10.1016/j.marpol.2013.11.011

Mac Dowell, N., Fennell, P. S., Shah, N., & Maitland, G. C. (2017). The role of CO2 capture and utilization in mitigating climate change. *Nature Climate Change, 7*(4), 243-249. Retrieved from https://doi.org/10.1038/nclimate3231. doi:10.1038/nclimate3231

Miocic, J. M., Gilfillan, S. M. V., Roberts, J. J., Edlmann, K., McDermott, C. I., & Haszeldine, R. S. (2016). Controls on CO2 storage security in natural reservoirs and implications for CO2 storage site selection. *International Journal of Greenhouse Gas Control, 51*, 118-125. Retrieved from http://www.sciencedirect.com/science/article/pii/S1750583616302626. doi:https://doi.org/10.1016/j.ijggc.2016.05.019

Nguyen, Q. P., Currie, P. K., & Zitha, P. L. J. (2003). *Determination of Foam Induced Fluid Partitioning in Porous Media using X-ray Computed Tomography*. Paper presented at the International Symposium on Oilfield Chemistry, Houston, Texas. https://doi.org/10.2118/80245-MS

NPD. (2011). *CO2 Storage Atlas Norwegian North Sea*. Retrieved from https://www.npd.no/en/facts/publications/co2-atlases/:

Picha, M. S. (2007). *Enhanced Oil Recovery By Hot CO2 Flooding*. Paper presented at the SPE Middle East Oil and Gas Show and Conference, Manama, Bahrain. https://doi.org/10.2118/105425-MS

Ransohoff, T. C., & Radke, C. J. (1988). Mechanisms of Foam Generation in Glass-Bead Packs. *SPE Reservoir Engineering, 3*(02), 573-585. Retrieved from https://doi.org/10.2118/15441-PA. doi:10.2118/15441-PA

Rognmo, A. U. (2019). CO2-Foams for Enhanced Oil Recovery and CO2 Storage.

Rognmo, A. U., Horjen, H., & Fernø, M. A. (2017). Nanotechnology for improved CO2 utilization in CCS: Laboratory study of CO2-foam flow and silica nanoparticle retention in porous media. *International Journal of Greenhouse Gas Control, 64*, 113-118. Retrieved from http://www.sciencedirect.com/science/article/pii/S1750583617303146. doi:https://doi.org/10.1016/j.ijggc.2017.07.010

Ruckenstein, E. (1996). Microemulsions, Macroemulsions, and the Bancroft Rule. *Langmuir, 12*(26), 6351-6353. Retrieved from https://doi.org/10.1021/la960849m. doi:10.1021/la960849m

Schramm, L. L. (1994). *Foams: fundamentals and applications in the petroleum industry* (Vol. 242): American Chemical Society Washington, DC.

Shi, J.-Q., Imrie, C., Sinayuc, C., Durucan, S., Korre, A., & Eiken, O. (2013). Snøhvit CO2 Storage Project: Assessment of CO2 Injection Performance Through History Matching of the Injection Well Pressure Over a 32-months Period. *Energy Procedia, 37*, 3267-3274. Retrieved from http://www.sciencedirect.com/science/article/pii/S1876610213004578. doi:https://doi.org/10.1016/j.egypro.2013.06.214

Simjoo, M., Dong, Y., Andrianov, A., Talanana, M., & Zitha, P. L. J. (2013). Novel Insight Into Foam Mobility Control. *SPE Journal, 18*(03), 416-427. Retrieved from https://doi.org/10.2118/163092-PA. doi:10.2118/163092-PA

Simjoo, M., & Zitha, P. L. J. (2019). Modeling and Experimental Validation of Rheological Transition During Foam Flow in Porous Media. *Transport in Porous Media*. Retrieved from https://doi.org/10.1007/s11242-019-01251-9. doi:10.1007/s11242-019-01251-9

Skauge, T., Spildo, K., & Skauge, A. (2010). *Nano-sized Particles For EOR*. Paper presented at the SPE Improved Oil Recovery Symposium, Tulsa, Oklahoma, USA. https://doi.org/10.2118/129933-MS

Song, W., Ogunbanwo, F., Steinsbø, M., Fernø, M. A., & Kovscek, A. R. (2018). Mechanisms of multiphase reactive flow using biogenically calcite-functionalized micromodels. *Lab on a Chip, 18*(24), 3881-3891.

Srivastava, S. (2003). *Understanding bacteria*: Springer Science & Business Media.
Tans, P., & Keeling, R. (2019). Trends in Atmospheric Carbon Dioxide. Retrieved 21.07.2019, from U.S. Department of Commerce\ National Oceanic and Atmospheric Administration\ NOAA Research https://esrl.noaa.gov/gmd/ccgg/trends/data.html
Yang, S. H., & Reed, R. L. (1989). *Mobility Control Using CO2 Forms*. Paper presented at the SPE Annual Technical Conference and Exhibition, San Antonio, Texas. https://doi.org/10.2118/19689-MS
Yokota, T., Yoshida, Y., Eguchi, N., Ota, Y., Tanaka, T., Watanabe, H., & Maksyutov, S. (2009). Global Concentrations of CO2 and CH4 Retrieved from GOSAT: First Preliminary Results. *SOLA, 5*, 160-163. doi:10.2151/sola.2009-041
Zeiss. Axio zoom.V16. Retrieved from https://www.micro-shop.zeiss.com/en/de/system/zoom-microscopes-axio+zoom.v16-zoom+microscopes/10257/
Zeng, F., & Zhao, G. (2008). Semianalytical Model for Reservoirs With Forchheimer's Non-Darcy Flow. *SPE Reservoir Evaluation & Engineering, 11*(02), 280-291. Retrieved from https://doi.org/10.2118/100540-PA. doi:10.2118/100540-PA
Zhang, P., Diao, Y., Shan, Y., Pei, S., Ren, S., Zhang, L., & Yang, H. (2020). Experimental investigation of amine-surfactant CO2 foam for smart mobility control during CO2 flooding. *Journal of Petroleum Science and Engineering, 184*, 106511. Retrieved from http://www.sciencedirect.com/science/article/pii/S0920410519309325. doi:https://doi.org/10.1016/j.petrol.2019.106511
Zulqarnain, M., Zeidouni, M., & Hughes, R. G. (2018). Implications of fault structure heterogeneities, dissolution and capillary trapping mechanisms for CO2 storage integrity. *International Journal of Greenhouse Gas Control, 76*, 53-61. Retrieved from http://www.sciencedirect.com/science/article/pii/S1750583618301452. doi:https://doi.org/10.1016/j.ijggc.2018.06.013
Zuta, J., Fjelde, I., & Berenblyum, R. (2009). *Oil recovery during CO2-foam injection in fractured chalk rock at reservoir conditions. SCA2009-27*.